Local Structure Analysis of Solid State Ionic Conductors, Perovskite-derived Structures by NMR and Computational Studies

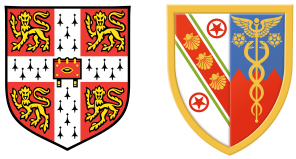

Rıza Dervişoğlu

Department of Chemistry / Darwin College

University of Cambridge

A thesis submitted for the degree of

Doctor of Philosophy

20/09/2013

I would like to dedicate this thesis to my loving wife,
Gülay Türkmen-Dervişoğlu.

Acknowledgements

First and foremost I would like to thank my supervisor Clare P. Grey. She has taught me how to approach a scientific problem analytically. Without her support I could not have completed my doctoral research. I appreciate all her contributions of time, ideas, and funding to make my PhD experience productive and stimulating. She has been a constant inspiration for rigorous scholarship, and an excellent example as a successful chemist and a professor.

I have had the opportunity to benefit from the teachings of several other scholars among whom are Peter Khalifah, John B. Parise, Brian Phillips, David Jefferson and Bill Jones. I thank them all for generously sharing their expertise with me. I would also like to thank my thesis examiners Saiful Islam and David Jefferson for taking the time to improve my scientific work.

The members of the Grey group have contributed immensely to my personal and professional development both in Stony Brook and in Cambridge. My heartfelt thanks go to Derek S. Middlemiss, Frédéric Blanc, Lesley Holmes, Barış Key, Fulya Doğan Key, Kenny Rosina, Ben Yunxu Zhu, Lucienne Buannic, Rosa Robert, Hua Huo, Matthew Dunstan, Xiao Hua, Hao Wang, Luke Sperrin, Lina Zhou, John Griffin, Michal Leskes, Yan-Yan Hu and Paul Bayley. I would like to convey my special thanks to Gunwoo Kim (The Korean), whose friendship made this journey more meaningful.

My stay during the summer of 2008 at University of Wisconsin, Madison has a special place in my PhD experience. It was in Madison that I was introduced to computational studies professionally. I thank Dane Morgan, Yueh-Lin Lee and the computational materials group

(CMG) in Madison for their help in my studies on cluster expansion and Monte Carlo simulations.

Both Argonne and Brookhaven national laboratories contributed to my studies with synchrotron x-ray source and computational resources. I greatly appreciate the support I have received from both institutions.

I would like to thank my friends from Stony Brook University in New York and Darwin College in Cambridge, who I lived together and had great conversations with, saving the world, each time: Marcos Crichigno, Masatoshi Sugeno, Ozan Erdoğan, Hung Cheng Chen, Irina Kostitsyna, Andrew Malingowsky, Nick Ostrum, Sarah Black, Helen Ngo, Patrick Donelan, Sean Dyde, Pascal Bugnion, Anshul Sirur, Matt Benton, Bianca Schmitt, Erika Davies and all the Dar Bar members.

Lastly, I would like to thank my family for all their love and encouragement. My parents, who raised me with a love of science, supported me in all my pursuits. I cannot thank them enough. Above all I thank my loving, supportive, encouraging, and patient wife Gulay. Despite the physical distance I have felt her comforting presence by my side throughout all these years. Thank you.

Abstract

In this work, local environments of ions in solid oxide fuel cell (SOFC) electrolyte materials with perovskite and perovskite-derived crystallographic structures, i.e. $Ba_2In_2O_5$, $Ba_2(In_{1-x}Ga_x)_2O_5$ and $Ba_2In_2O_4(OH)_2$, were investigated for their high ionic (O^{2-} and H^+) mobility at elevated temperatures. Two general methods were employed in this investigation; first, computational methods, such as density functional theory (DFT), gauge including projector augmented wave (GIPAW), cluster expansion (CE) and Monte Carlo simulations (MC); second, experimental methods, such as nuclear magnetic resonance (NMR), X-ray scattering (both powder diffraction and pair distribution function (PDF) analysis) and thermo-gravimetric analysis (TGA). The parent material, $Ba_2In_2O_5$, has inherent oxygen vacancies which allow for fast O^{2-} ion mobility at elevated temperatures and for hydration of the material needless of doping. We improve a previous NMR study of $Ba_2In_2O_5$ by Adler et al. [1], assigning all three oxygen crystallographic sites to their relevant NMR peaks and investigate the high temperature structure. We then study the iso-valent doping of Ga into the In site resulting in $Ba_2(In_{1-x}Ga_x)_2O_5$. While Yao et al. [2] find that Ga doping levels higher than 20% form a stable cubic structure, our findings indicate that Ga doping results in a phase segregation. However our findings for quenched samples are no different than those of Yao et al. [2]. Lastly we study the hydrated form of the parent material, $Ba_2In_2O_4(OH)_2$, which has high H^+ ion mobility above 180°C. We observe at least three possible hydrogen sites with local environments slightly different from the previous neutron diffraction study by Jayaraman et al. [3]. In contrast to the observation by Jayaraman et al. [3] of the hydrogen presence in all O2 layers we find an alternating occupancy of hydrogens in those layers.

Contents

List of Figures

Chapter 1

Introduction

Long range ionic conductivity is not a common property of solids , where atoms are essentially fixed on their lattice sites, in contrast to liquids and gases where atoms move freely. However, some crystals show almost liquid-like ionic conductivity for one or more types of ions. These materials have common structural properties, some having intrinsic defects, some having large interstitial sites, possessing open channels, layers or complex three dimensional cages through which ions may easily move by various mechanisms such as hopping, vehicle, vesicle and more (Phillips [25], Bruce [26], Hagenmuller and van Gool [27], Kudo and Fueki [28], Shewmon [29]). Generally solid oxygen ion-conducting materials tend to be metal oxides with high crystallographic symmetry and motional disorder at higher, working, temperatures, forming necessary open channels and pathways for ionic motion.

There has been great interest in studying properties of ionic conductors so as to develop new materials for use in solid state devices such as Solid Oxide Fuel Cells (SOFCs), sensors and gas separation membranes.(Shewmon [29], Julien and Nazri [30], Kharton et al. [31], Tillement [32]) SOFCs have the potential to be a clean, low emission, quiet, reliable, fuel adaptable, transportable and highly efficient method for the generation of electricity. The basic principle of operation involves the transport of ions (oxygen or hydrogen) through a solid electrolyte interposed between a cathode and anode, and the subsequent reaction of oxygen with fuel to form an electric current. (Figure 1.1)

In general electrolyte materials are required to have ionic conductivity and

no electronic conductivity. Y-stabilized ZrO_2 (YSZ) is one of the traditional oxygen conducting solid electrolytes, with high ionic conductivity at an order of 10^{-3} Scm^{-1} without electronic conductivity at 500 °C. However, much higher ionic conductivities are observed in contemporary materials such as $La_{0.8}Sr_{0.2}Ga_{0.8}Mg_{0.2}O_3$ (LSGM) at an order of $10^{-1.5}$ Scm^{-1} at 500 °C. On the other hand, hydrated $BaZrO_3$ is one of the traditional proton conducting solid materials with ionic conductivity at an order of $10^{-1.5}$ Scm^{-1}. Yet $BaZrO_3$ requires acceptor doping (such as Y) in order to initiate O vacancy and consecutively H_2O intake to the material.(Kreuer [4]) (Figure 1.2)

Electrodes in general are required to have both ionic and electronic conductivity. For SOFCs the most common anode material is the nano-particle sized Ni metal supported by a high surface are ceramic material (such as YSZ). The common cathode material in the other hand is the $La_{1-x}Sr_xMnO_3$ (LSM) which has a very high electronic as well as oxygen ion conductivity.

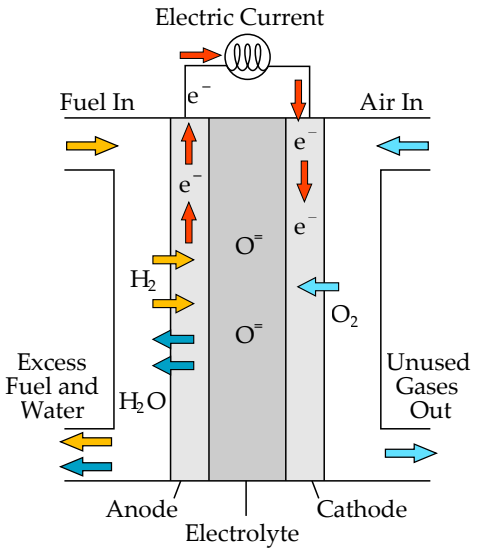

Figure 1.1: Schematic of a solid oxide fuel cell

In this chapter we will introduce various fundamental concepts underpinning ionic conductivity in oxygen and proton conducting solid electrolytes, and briefly discuss the application of solid state NMR, high energy x-ray diffraction and

computer simulations methods such as *ab initio* density functional theory (DFT) calculations, gauge including augmented plane-wave (GIPAW) NMR calculations and cluster expansion (CE) and Monte Carlo simulations to the materials within the family of metal oxides known as perovskites investigated here.

1.1 Ionic Conductivity in Solids

The conductivity of a charged particle, σ , is defined in equation (1.1),

$$\sigma = nZe\mu \tag{1.1}$$

where n is the number of current/charge carriers, Ze is their charge (expressed as a multiple of the electron charge, $e = 1.602189\text{x}10^{-19}$ C) and μ the mobility.

To be able to understand the ionic conductivity in solids we should start from a simple example of electronic conductivity with $Z = 1$ in equation 1.1. The number of electrons in metals in the conduction band is large and virtually constant, but their mobility decreases with increasing temperature due to electron-phonon interactions. You can imagine lack of synchronization between the electronic motion and the narrowing and enlarging of bottle neck positions cycle on the pathway of these electrons. As a result electronic conductivity decreases with increasing temperature. Semiconductors have a smaller number of electrons in the conduction band, similar to ionic conductivity in solids, and their conductivity can be increased by raising the temperature to promote more electrons into the conduction band. The number of current/charge carriers, n is given by

$$n = n_0 exp(-E/RT) \tag{1.2}$$

where n_0 is the total number of charges (e.g. total number of electrons), E is the activation energy, R is the gas constant and T is temperature. The number of charge carriers n and therefore the conductivity, σ, rise exponentially with increasing temperature. Accordingly, small changes in mobility, μ, have little influence on the total conductivity compared to the dominant influence of the number of charge carriers, n. (see equations (1.1) and (1.2)) The example of electronic conductivity in a semiconductor can be applied directly onto solid

state ionic conductors, by taking the activation energy of the rate limiting step in the relevant ionic-motion mechanism for a system.

Figure 1.2 is an Arrhenius plot of both oxygen and proton ionic conductivity of well known electrolytes for SOFCs. $Ba_2In_2O_5$, oxygen and $Ba_2In_2O_4(OH)_2$, proton conductivities are shown with red dashed and solid lines, respectively.

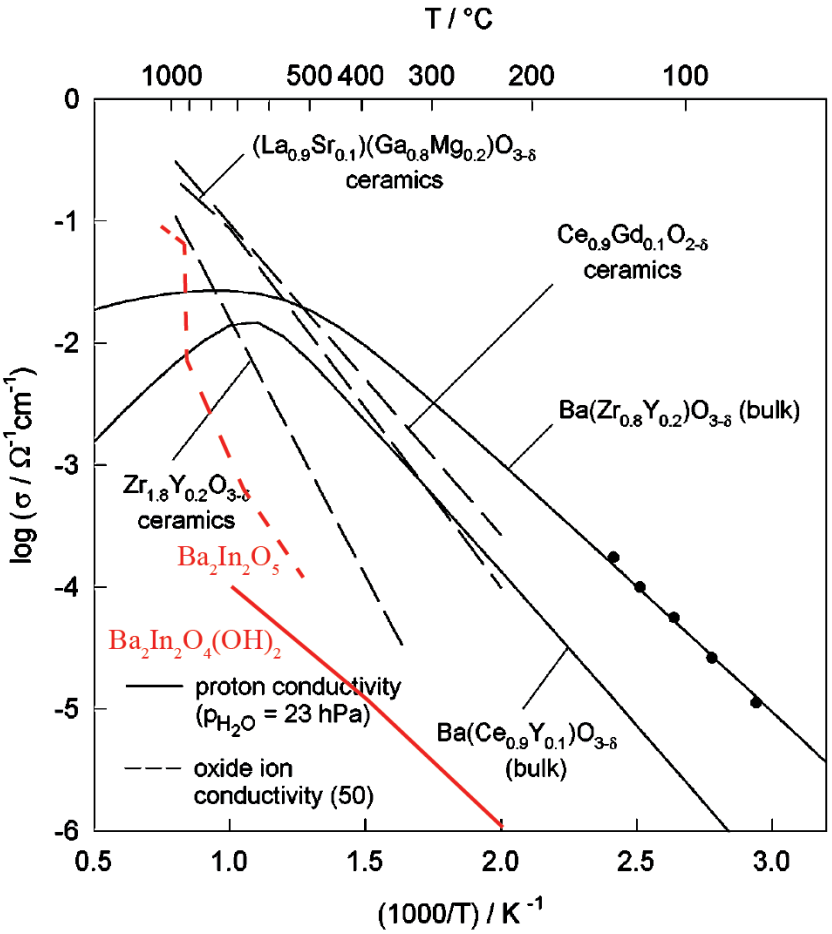

Figure 1.2: Bulk conductivity of 20Y:$BaZrO_3$ compared with the proton conductivity of 10Y:$BaCeO_3$ and the oxide ion conductivity of the best oxide ion conductors.(Kreuer [4], Goodenough [5], Steele and Heinzel [6]) Figure reproduced from work by Kreuer [4] and modified from works by Goodenough et al. [7] and Zhang and Smyth [8]

1.2 Properties of perovskite and perovskite derived structures

Perovskites are a broad class of materials with widespread applications, notably here as electrolytes for intermediate- and high-temperature fuel cells due to their high oxygen and proton conductivities. Perovskites are named after the perovskite mineral with the chemical formula $CaTiO_3$ which adopts a cubic structure in space group $Pm\bar{3}m$. (Figure 1.3) They are increasingly recognized as competitors to more conventional electrolyte phases such as yttria-stabilized zirconia (YSZ) and other fluorite-based compounds. The structural family possesses ABO_3 stoichiometry where the A-cations are typically rare-earths or alkaline-earths and the B-cations are transition metals or semi-metals (Smyth [33], Adler et al. [34]) of varying oxidation states and ionic radii. The B-site cations are each bonded to six O ions to form corner-sharing BO_6 octahedra, while the A-site cations occupy the cubic space formed between eight BO_6 units, coordinated to the twelve nearest-neighboring O ions. Anisotropic expansion of the unit cell, namely deviations from the cubic cell, and significant tilting of the octahedra, as described by Woodward [35, 36], Glazer [37], may occur depending on the relative size of the A and B cations. The tuning of these distortions can potentially lead to increased ionic conductivity due to the change of total lattice energies or more specifically the variation in bottlenecks for diffusion of ions through a given structure.(Woodward [35]) The ideal perovskite structure results in a simple cubic cell with space group $Pm\bar{3}m$. (Figure 1.3) Doping with lower valent cations typically introduces compensating extrinsic O vacancies, and constitutes the most frequently pursued strategy to synthesize phases with increased ionic conductivity.

1.2.1 $Ba_2In_2O_5$

The present study focuses on the $Ba_2In_2O_5$ defect perovskite phase, on the basis that it has been found to have O ionic conductivity significantly exceeding that of YSZ at intermediate and high temperatures. (Goodenough et al. [7], Kharton et al. [31], Kendall et al. [38], Adler [39], Islam et al. [40], Prasanna

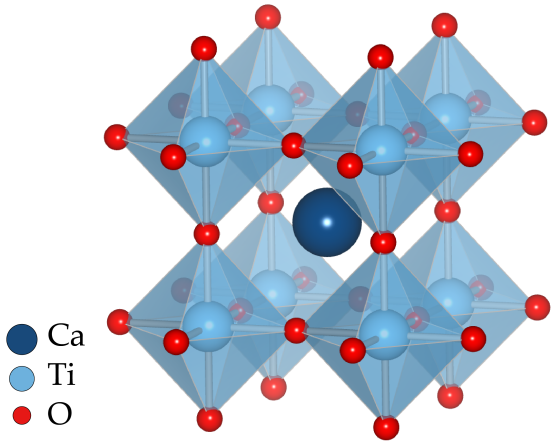

Figure 1.3: The crystal structure of the perovskite, $CaTiO_3$, in space group $Pm\bar{3}m$, which lends its name to a family of compounds with the same general crystal structure.

[41], Mohn et al. [42], Yoshinaga et al. [43], Hashimoto [44], Rolle et al. [45]) $Ba_2In_2O_5$ manifests as a highly O-deficient perovskite, wherein the compensation of the Ba^{2+} and In^{3+} cation charges requires the removal of one-sixth of the O atoms in the perovskite structure, yielding a high intrinsic concentration of O vacancies. The vacancies order at room temperature into an orthorhombic structure with space group $Ibm2$ (Colville and Geller [10], Gregory and Weller [11]). An alternative $Icmm$ space group with disorder of In2 and O3 over $8i$ positions has also been suggested by both Speakman et al. and Berastegui et al.,[12, 13] with both space groups yielding very similar diffraction patterns. Three crystallographically-distinct O sites arise in the $Ibm2$ form, ordered so as to form alternating layers of tetrahedral (Tet, Tet') and octahedral (Oct) In^{3+} centered polyhedra, with successive (010) tetrahedral layers offset from one another in an $\cdots OctTetOctTet' \cdots$ staggered O vacancy pattern (Figure 1.4a). The first high energy state found by Mohn et al. [42], by calculations at a relative energy difference of 5.0 kJ/mol, has an $\cdots OctTetOctTet \cdots$ stacked O vacancy pattern (Figure 1.4b). The labeling adopted hereafter places O1 anions at the equatorial positions of the octahedra, O2 bridging the octahedral and tetrahedral layers, and O3 within the tetrahedral layer. The structure is termed a brownmillerite

phase after the original Ca_2FeAlO_5 mineral manifesting a similar arrangement of O vacancies.(Colville and Geller [10]) $Ba_2In_2O_5$ undergoes a series of phase changes from the room temperature orthorhombic structure just described, to a tetragonal form (in space group $I4cm$) above 925°C, and subsequently to a disordered cubic phase (in space group $Pm\bar{3}m$) above 1040-1075°C, the exact temperature varying betwen studies. (Speakman et al. [12], Steele [46]) It is only in the tetragonal and cubic forms that the material displays substantial ionic conductivity.(Goodenough et al. [7], Speakman et al. [12])

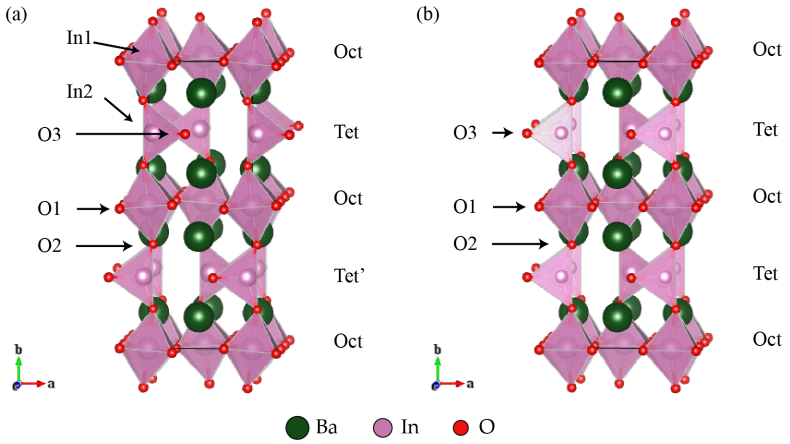

Figure 1.4: Room temperature crystal structure of (a) ground state orthorhombic brownmillerite $Ba_2In_2O_5$ in space group $Ibm2$ with $\cdots OctTetOctTet' \cdots$ staggered O vacancy pattern and (b) the first high energy state $\cdots OctTetOctTet \cdots$ stacked O vacancy pattern.

1.2.2 $Ba_2In_2O_4(OH)_2$

Hydration of $Ba_2In_2O_5$ at high temperature results in a tetragonal structure with space group $P4/mbm$ where the intrinsic vacancies of $Ba_2In_2O_5$ in the O3 layer are fully occupied by the water O atoms. One of the water protons fully occupies the H2 sites over $2c$ positions while the second proton partially occupies (0.125) the H1 sites over $16l$ position according to combined X-ray and neutron diffraction analyses. (Figure 1.5a)(Jayaraman et al. [3]) Conductivity data for

both $Ba_2In_2O_5$ and $Ba_2In_2O_4(OH)_2$ were reported by Goodenough et al. [7] and Zhang and Smyth [8] respectively. While the large number of O vacancies in the tetrahedral layers of $Ba_2In_2O_5$ might be thought to be conducive to rapid anion conduction, freezing of the vacancies in the low temperature orthorhombic phase allows for only limited O motion. The O conductivity increases by several orders of magnitude as the material first enters the tetragonal (925°C) and later the cubic phase at high temperature (1040-1075°C)(Speakman et al. [12], Steele [46]) and the vacancy distribution becomes disordered. Fisher et al. [47] have speculated that this process involves the migration of some fraction of the O1 and O2 oxygens into the tetrahedral layer vacancies, with the effect that the mean coordination numbers of the formerly distinct tetrahedral and octahedral In sites tend toward equality and the material becomes cubic on average. Meanwhile, conductivity studies of $Ba_2In_2O_4(OH)_2$ suggest three regions of protonic conduction corresponding broadly to temperatures below 400°C, between 400 and 925°C, and above 925°C. Zhang and Smyth [8] suggests a Grotthuss (H hopping) or vehicle (OH hopping) mechanism as a means of protonic conductivity. At lower temperatures the material is most likely to express Grotthuss conduction and at elevated temperatures vehicle conduction or a combination of both.

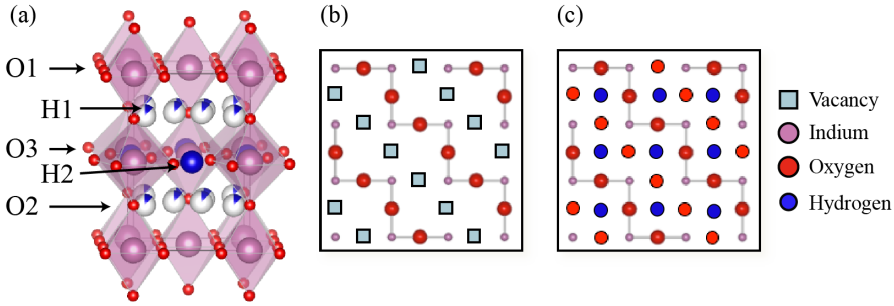

Figure 1.5: (a) Room temperature crystal structure of tetragonal $Ba_2In_2O_4(OH)_2$ in space group $P4/mbm$.(Jayaraman et al. [3]) and schematic representations of the O3 layer of (b) $Ba_2In_2O_5$ and (c) $Ba_2In_2O_4(OH)_2$. The interlayer Ba atoms have been omitted for clarity. Sector filling of atoms in (a) denotes site occupancies.

1.2.3 $Ba_2(In_{1-x}Ga_x)_2O_5$

A more detailed insight is required into the mechanisms governing the coupling between dopants and vacancies, the mutual interactions of these vacancies and the factors that control the formation of the ordered brownmillerite structure. To elucidate some of these phenomena, the pristine and the Ga-substituted phases of barium indium oxide (with chemical formula $Ba_2In_2O_5$ and $Ba_2(In_{1-x}Ga_x)_2O_5$, respectively) have been investigated. Isovalent substitution of Ga on the In sublattice results in a $Ba_2(In_{1-x}Ga_x)_2O_5$ stoichiometry allowing the effect of cation substitution to be investigated while keeping the oxygen concentration (and thus vacancy concentration) constant.

The low temperature orthorhombic form of $Ba_2In_2O_5$ adopts the brownmillerite structure as previosly discussed and shown in Figures 1.4a and 1.5b.(Speakman et al. [12], Fischer et al. [48]) A previous study of the Ga-substituted phases by Yao et al. [2] revealed an orthorhombic structure at ambient temperature for low doping levels, and a cubic structure for $x \geq 0.25$. $Ba_2In_2O_5$ has two phase transformations, a first-order transformation at 950°C and a second-order transformation at 1040°C.(Speakman et al. [12]) The high oxygen ion conductivity, crucial for its application as an SOFC electrolyte occurs only above the 950°C first-order orthorhombic-tetragonal phase transformation.(Goodenough et al. [7]) The first-order transformation is regarded as undesirable, both because it requires a high temperature for oxygen transport and because it can lead to cracking and failure of the electrolyte during operation. According to a study by Yao et al. [2], both phase transformations have been shown to disappear for sufficiently high levels of Ga-doping, which can stabilize the high-temperature disordered phase. While the effect of doping on the phase transformations is known Yao et al. [2], Rolle et al. [49], less is understood about the local environments experienced by dopants, the phase energetics, and the process of oxygen ion conduction in the presence of the dopants.

1.3 NMR spectroscopy

Edward Mills Purcell and Felix Bloch discovered the interaction between nuclear spin and a magnetic field, which forms the basis of NMR, in 1945.(Purcell et al. [50], Bloch et al. [51]) NMR is a versatile tool to probe the electronic environment around most of the atoms in the periodic table of elements, and to investigate local structure and motion at atomic level.

Nuclear spin interactions with nucleus' surrounding environment can be grouped in to internal and external spin interactions. External spin interactions are between the nuclear spin and the external magnetic field generated, e.g. a static magnetic field and a radio frequency. The internal spin interactions are between the nuclear spin and the electro-magnetic fields within the sample itself, such as nuclear-nuclear and nuclear-electronic interactions, i.e. shielding interactions (chemical and paramagnetic shifts), dipolar interactions, the quadrupolar interaction and the spin-rotation interaction.

In the past decade solid state NMR spectroscopy has been improved in many aspects such as developing higher magnetic field, probes with higher sample spinning frequencies, new pulse sequence designs (Amoureux et al. [52]), specialty probes (i.e. micro-coil (Takeda [53]), high temperature laser (Stebbins [54], Taulelle et al. [55]) and in-situ electro-chemical (Letellier et al. [56], Chevallier et al. [57], Letellier et al. [58], Key et al. [59]) probes) and theoretical frameworks to bridge *ab initio* calculations to NMR experiments. Thanks to these developments we can investigate the local structure of solid materials and dynamics of ionic motion in solids with increasing accuracy. Theoretical improvements include the use of *ab initio* density functional theory (DFT) calculations with gauge including projector augmented wave (GIPAW) method to predict NMR parameters and hence the spectra. Thus allows the modelling of local environments in crystal structures and further analysis of complex spectra with resolution and assignment of the different resonances.(Charpentier [60], Bonhomme et al. [61], Pickard and Mauri [62])

Lack of model compounds, describing local environments, for disordered structures have been another issue in the field and has been answered by various methods such as Monte Carlo simulations (van de Walle and Ceder [63]), evolutionary

algorithm (Oganov and Glass [64]) and random structure searching (Pickard and Needs [65]). Here we use the Monte Carlo simulations method in order to generate model compounds for NMR GIPAW calculations as well as to investigate phase transition properties.

In this section we make use of various resources in order to summarize the broad topic of solid state NMR, with a focus on quadrupolar nuclei and *ab-initio* methods.(Keeler [66], Levitt [67], Hore [68], Duer [69], MacKenzie and Smith [70], Apperley et al. [71], Kucukbenli [72])

1.3.1 Nucleus in a static uniform field

The Hamiltonian of an isolated spin in a static uniform magnetic field $\boldsymbol{B}_0$, without considering any other interaction is simply the Zeeman Hamiltonian:

$$H = \boldsymbol{\mu} \cdot \boldsymbol{B}_0 \tag{1.3}$$

where $\boldsymbol{\mu}$ is the nuclear magnetic moment operator:

$$\boldsymbol{\mu} = \gamma \hbar \boldsymbol{I} \tag{1.4}$$

with γ being the nuclear gyromagnetic ratio and $\mathbf{I}$ the nuclear spin operator. The direction of the field, which can be chosen as $\hat{z}$, gives the quantization axis. Therefore the Hamiltonian H is proportional to the operator I_z and the eigenfunctions of I_z, which can be labeled as $|I, m\rangle$, are also the eigen functions of the Hamiltonian:

$$H\,|I, m\rangle = E_{I,m}\,|I, m\rangle \tag{1.5}$$

with eigenvalues $E_{I,m} = -\gamma \hbar B_0 m$ using $I_z\,|I, m\rangle = m\,|I, m\rangle$.

For a spin with $I = \frac{1}{2}, m = \pm\frac{1}{2}$, there are two possible eigenstates with energies $E_m = \pm\frac{1}{2}\gamma\hbar B_0$, which are commonly called Zeeman states. (Figure 1.8)

These two eigenstates have different energies so that any superposition state non-parallel to the eigenstates will have a net time evolution, which results in a precession with the frequency proportional to the energy difference between the

eigenstates:

$$\Delta E = \gamma \hbar B_0 = \hbar \omega_0 \tag{1.6}$$

This phenomenon is referred to as the Larmor precession and the frequency ω_0 is called the Larmor frequency. At a given magnetic field B_0, the Larmor frequency can be used to distinguish different nuclei from each other as it depends on nuclear mass and charge through the gyromagnetic ratio γ. In a macroscopic sample, the spin states are populated according to the Boltzmann distribution, where the population of a state ψ with energy E_ψ, at temperature T is:

$$p_\psi = \frac{e^{-E_\psi/kT}}{\sum_{\psi'} e^{-E_{\psi'}/kT}} \tag{1.7}$$

Therefore, in typical NMR experiments, only the ensemble averages are measured for any observable.

1.3.2 Chemical shift / Shielding

So far we have only considered the interactions with external magnetic fields, and neglected other sources of magnetic fields internal to the sample. In NMR experiments the applied static field is, in general, orders of magnitude larger than the internal local fields. Therefore its direction should still be taken as the axis of quantization. However, local fields in the direction of the static field, or precessing in the plane perpendicular to the static field near the resonance frequency significantly affect the spin states. Some of the important interactions are the chemical shielding, through space nuclear spin dipole-dipole coupling and the quadrupolar interaction. Here we will focus on the chemical shielding interaction.

If only the bare nucleus were to be considered, any atom (e.g. hydrogen) with the same nuclear mass would result in the same nuclear magnetic resonance frequency. However the electrons surrounding each nucleus are influenced by the magnetic field as well and produce a secondary field, which changes the resonance frequency of each nucleus. Due to the response of the electrons, we observe different resonance frequencies for atoms in different chemical environments. This

shift in resonance frequency is called the chemical shift as it provides information on the chemical environment of the nuclei.

The local field contributions from shielding interactions can be divided in two types: A diamagnetic contribution of a primary induced current of electrons that produce a magnetic field opposing the applied field; And a paramagnetic contribution where the external magnetic field can mix the high energy states with paramagnetic properties with the ground state, inducing paramagnetism, which generates a field supporting the applied field.

Since the electron distribution around a current is not spherically symmetric, the shielding associated to a nucleus is given by a second rank tensor, denoted by $\boldsymbol{\sigma}$, and the perturbative Hamiltonian due to this effect can be written as

$$H_{cs} = -\gamma\hbar \boldsymbol{I} \cdot \boldsymbol{\sigma} \cdot \boldsymbol{B}_0 \tag{1.8}$$

where $\boldsymbol{I}$ is the spin of the nucleus of interest. For $\boldsymbol{B}_0$ in the $\hat{z}$ direction, the first order contribution to the energy of a spin level $|I, m\rangle$ from chemical shielding, E_{cs} is:

$$E_{cs} = -\gamma\hbar\sigma_{zz}B_0 \langle I, m| Iz |I, m\rangle - \gamma\hbar\sigma_{zz}B_0 m \tag{1.9}$$

Note also that it is useful to symmetrize the shielding tensor as the symmetric component is the only one with a significant effect on the chemical shifts.

While describing σ, it is possible to choose an axis frame different from the laboratory frame, such as the one where σ becomes diagonal. This axis frame is called the principal axis system (PAS). The diagonal elements of σ in the PAS are often expressed in terms of the isotropic value σ_{iso}, the anisotropy Δ and the asymmetry η, defined as

$$\begin{aligned}\sigma_{iso} &= \frac{1}{3}(\sigma_{xx}^{PAS} + \sigma_{yy}^{PAS} + \sigma_{zz}^{PAS}) \\ \Delta &= \sigma_{zz}^{PAS} - \sigma_{iso} \\ \eta &= \frac{(\sigma_{xx}^{PAS} - \sigma_{yy}^{PAS})}{\sigma_{zz}^{PAS}}\end{aligned} \tag{1.10}$$

Using these definitions, for an axially symmetric shielding tensor and external field in $\hat{z}$, we can write the chemical shift frequency as a function of the polar angles (θ, ϕ) that define the orientation of the external magnetic field B_0 in the PAS:

$$\omega_{cs}(\theta, \phi) = -\omega_0\sigma_{iso} - \frac{1}{2}\omega_0\Delta[(3\cos^2\theta - 1) + \eta\sin^2\theta\cos 2\phi] \tag{1.11}$$

where $-\omega_0\sigma_{iso}$ is the chemical shift frequency relative to a bare nucleus with Larmor frequency ω_0. In powder samples, the line shape of an NMR spectrum can be deduced from the chemical shift parameters and vice versa.

In NMR experiments, due to practical reasons, instead of the absolute frequency $\omega_0 + \omega_{cs}$, the frequency relative to a specific signal of a reference sample is measured. This relative shift is called the chemical shift, δ, and the isotropic chemical shift δ_{iso} is given as,

$$\delta_{iso} = \sigma_{iso}^{ref} - \sigma_{iso} \tag{1.12}$$

Often in experiments the PAS is not known and the principal values of chemical shift tensor are labeled by convention as $\delta_{11}^{PAS} \geq \delta_{22}^{PAS} \geq \delta_{33}^{PAS}$. The chemical shift anisotropy Δ_{cs} and asymmetry η_{cs} are defined as:

$$\Delta_{cs} = \delta_{11}^{PAS} - \delta_{iso}\eta_{cs} = \frac{\delta_{33}^{PAS} - \delta_{22}^{PAS}}{\delta_{11}^{PAS}} \tag{1.13}$$

and the chemical shift that is measured in experiments can be written as

$$\delta = \delta_{iso} + \frac{1}{2}\Delta_{cs}\left[(3\cos^2\theta - 1) + \eta\sin^2\theta\cos 2\phi\right] \tag{1.14}$$

So far we have given a basic introduction to the chemical shielding interaction concept.

1.3.3 Scalar coupling / Spin-spin interactions

In the simplest form the scalar coupling arises from indirect interaction between two nuclear spins, where the interaction is mediated by the electrons participating in the bonds connecting the nuclei. Different energy states due to multiple spin-quantum levels generates quantized deviation in chemical shielding, resulting in multiplet pattern on NMR spectra. The simplest energy splitting arises from parallel vs. anti-parallel coupled electron-spin electron-spin in an orbital of an atom. Another example is the Fermi contact interaction which is a nuclear-spin electron-spin interaction observed in paramagnetic systems where the simplest energy splitting would occur due to parallel vs. anti-parallel nuclear-spin electron-spin coupling. This interaction has many names such as J-coupling, indirect coupling, spin-spin coupling and scalar coupling, which is due to the atomic/molecular/crystallographic configuration, the nuclear spin state(s) and its electronic-spin configuration. Writing an equation of energy, with A and X representing two interacting nuclei,

$$E = hJ_{AX}m_Am_X \tag{1.15}$$

where m_A, m_X are the magnetic quantum numbers of the two nuclei and J_{AX} is the spin-spin coupling constant, we can now write the equation of the NMR shift, as described so far, including the indirect coupling,

$$\nu_A = \frac{\gamma_A B_0(1-\sigma_A)}{2\pi} - \sum_{X\neq A} J_{AX}m_X \tag{1.16}$$

1.3.4 Dipolar coupling

Dipolar coupling is a through space, nuclear-spin nuclear-spin coupling of multiple nuclei, due to magnetic dipole moments of individual nucleus. In order to understand the dipolar coupling one should first understand the point dipole and the magnetic field around it.

Point dipole and its magnetic field: Nuclei with a non zero spin quantum number possess a magnetic dipole moment, $\boldsymbol{\mu}$. This kind of nucleus acts like a small bar magnet with two poles (hence di-pole), north and south. Aligning the north pole with the z axis and positioning the dipole at the origin of the coordinate system and recognizing the $D_{\infty h}$ point group symmetry we can simply describe the magnetic force field around the magnet only in one plane (hence only in 2D), for example the zx plane. Now we can define the magnetic field, B_μ at any point in the zx plane, with the angle, θ, between the z axis, the origin and the point, and the distance, r from the origin to the point.

$$\begin{aligned} B_{\mu x} &= \left(\frac{\mu_0}{4\pi}\right)\left(\frac{\mu}{r^3}\right)(3\sin\theta cos\theta) \\ B_{\mu y} &= 0 \quad \text{“for 2D case in } zx \text{ plane”} \\ B_{\mu z} &= \left(\frac{\mu_0}{4\pi}\right)\left(\frac{\mu}{r^3}\right)(3\cos^2\theta - 1) \end{aligned} \tag{1.17}$$

where μ_0 is the permeability of vacuum, and μ is the magnitude of the magnetic moment $\boldsymbol{\mu}$.

It is important to note that the magnitude of the magnetic field, B_μ decreases in a cubic manner with increasing distance, r. Its direction depends on the position with respect to the origin.

Dipolar interaction between nuclei: Two point dipoles will magnetically effect each other through space due to their individual magnetic fields. Under no influence of an external magnetic field these dipoles will take an anti-parallel alignment. However under a high external magnetic field such as the NMR magnetic field both dipoles will align parallel with the external magnetic field with a

small deviation due to effects from the nuclear dipole moments of each other. For example, if we place nucleus A on the origin and nucleus X on a point (r, θ), both with different gyromagnetic ratios, in the coordinate system defined in paragraph above (section 1.3.4), we can see that the NMR observable resonance frequency of the nucleus X, ν_X, which is dependant only to the z component of the magnetic field $(B_0 \pm B^A_{\mu z})$, creates a spectral splitting,

$$\begin{aligned} \text{heteronuclear dipolar splitting / Hz} &= K_{AX}(3\cos^2\theta - 1) \\ 2\pi K_{AX} &= \left(\frac{\mu_0}{4\pi}\right)\frac{\hbar\gamma_A\gamma_X}{r^3_{AX}} \end{aligned} \tag{1.18}$$

From these equations it is clear that the change in θ from 0° to 90° ($2 \geq (3\cos^2\theta - 1) \geq -1$) will cause the doublet splitting to first decrease, pass through 0 (at the magic angle, 54.74°, 1.3.6) and increase again. In powder samples however, due to the presence of many crystallographic orientations with respect to the external magnetic field there is an overlap of these spectra and they result in Pake doublet shaped spectra (Figure 1.6), where the horns correspond to $\theta \approx 90°$ and the wings come from the $\theta \approx 0°$ orientation.

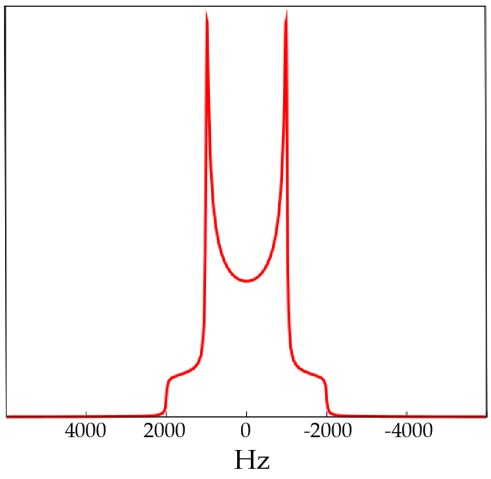

Figure 1.6: A computer simulation of a powder sample with Pake doublet shape with $K_{AX} = 1$ kHz and $\nu_0 = 0$ Hz.

1.3.5 Quadrupolar interactions and ^{17}O NMR

A nucleus with a spin quantum number, I $\geq \frac{1}{2}$ has an electric quadrupole moment, eQ, in addition to the magnetic dipole moment, which interacts with the electric field gradient (EFG) caused by the surrounding electrons of the atom. The quadrupole moment of the nucleus has a charge distribution in an elliptic shape with the high positive (or low positive) charge density concentrated towards the tips of the ellipse and the low positive (or high positive) charge density around the equator of the ellipse, forming (+-+) or (-+-) in (tip-equator-tip) configuration.

The EFG at the nucleus is a measure of the inhomogeneity of the local electron charge. Hence it gives important information about the symmetry surrounding the atom in question. In highly symmetrical atomic environments (e.g. spherical, cubic, tetrahedral, octahedral symmetry) the electric fields cancel each other and the EFG is zero which further results in a zero nuclear quadrupole coupling constant, C_Q as described in equation (1.19). However in less symmetric cases the EFG is not zero and the poles of the ellipse align towards the most electronegative center around the nucleus, in an energy minimizing fashion. As such, the direction of the ellipse changes depending on the alignment of the atomic environment with respect to the magnetic field. Distribution of orientations in powder samples result in broad peaks in a shape shown in Figure 1.7 in powder NMR. This shape is further affected by the asymmetry measured from the asymmetry parameter where $\eta_Q = 0$ produces two horns- and $\eta_Q = 1$ produces a single horn-shape, both with characteristic shoulders. (Figure 1.7)

There are two parameters defining the nuclear electric quadrupole moment, the nuclear quadrupole coupling constant, C_Q defining the anisotropy of the EFG tensor and the asymmetry parameter, η_Q defining the asymmetry of the EFG, with the following equations,

$$C_Q = \frac{eQV_{ZZ}}{h} \tag{1.19}$$

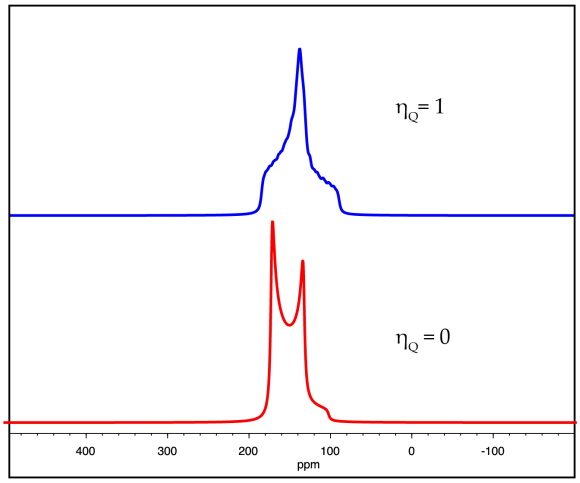

Figure 1.7: A computer simulation of a quadrupolar NMR spectra of a powder sample with $\eta_Q = 0$ and $\eta_Q = 1$, both with $C_Q = 4$ MHz and $\sigma_{iso} = 185$ ppm.

$$\eta_Q = \frac{V_{XX} - V_{YY}}{V_{ZZ}} \tag{1.20}$$

where $|V_{ZZ}| \geq |V_{YY}| \geq |V_{XX}|$ are the principal components of the diagonalized EFG tensor, $\boldsymbol{V}$.

When C_Q is very large a full theoretical treatment should be used with the quadrupolar Hamiltonian,

$$\hat{H}_Q = \frac{eQ}{2I(2I-1)} \hat{\boldsymbol{I}} \cdot \boldsymbol{V} \cdot \hat{\boldsymbol{I}} \tag{1.21}$$

Equation (1.21) can be written in terms of components C_Q and η_Q in the PAS as

$$\hat{H}_Q = h \frac{C_Q}{4I(2I-1)} \left[3\hat{I}_z^2 - \hat{\boldsymbol{I}}^2 + \frac{1}{2}\eta_Q(\hat{I}_+^2 + \hat{I}_-^2) \right] \tag{1.22}$$

However, the energy states of the electric quadrupole moment can also be derived by perturbation theory. Perturbation theory allows an expression of the quadruple moment with a sum of terms with decreasing significance. In most cases second-order perturbation theory is sufficiently accurate for calculating elec-

tric quadrupole moment interactions.

$$\hat{H}_Q = \hat{H}_Q^{(1)} + \hat{H}_Q^{(2)} \tag{1.23}$$

The first order Hamiltonian will produce the first order contribution of the energy as

$$E_Q^{(1)} = h\left[\left\{\frac{3m_I^2 - I(I+1)}{8I(2I-1)}\right\}[(3cos^2\theta - 1) + \eta_Q cos2\phi sin^2\theta]C_Q\right] \tag{1.24}$$

where m_I is the spin-component quantum number and the polar angles θ and ϕ are of V_{ZZ} in $\boldsymbol{B}_0$.

The second order Hamiltonian will produce the second order contribution of the energy as

$$\begin{aligned} E_Q^{(2)} = \frac{hm_I}{2\nu_0}\left(\frac{C_Q}{2I(2I-1)}\right)^2 \Bigg[&\frac{3}{5}\{I(I+1) - 3m_I^2\}P_0(cos\theta) + \\ &+\frac{3}{14}\{8I(I+1) - 12m_I^2 - 3\}P_2(cos\theta) - \\ &-\frac{9}{70}\{18I(I+1) - 34m_I^2 - 5\}P_4(cos\theta)\Bigg] \end{aligned} \tag{1.25}$$

where θ is the angle between V_{ZZ} and the $\boldsymbol{B}_0$, ν_0 is the Larmor frequency, and m_I is the spin-component quantum number of the energy level. The zeroth-, second- and fourth-degree *Legendre polynomials* in the equation are,

$$\begin{aligned} P_0(cos\theta) &= 1 \\ P_2(cos\theta) &= \frac{1}{2}(3cos^2\theta - 1) \\ P_4(cos\theta) &= \frac{1}{8}(35cos^4\theta - 30cos^2\theta + 3) \end{aligned} \tag{1.26}$$

Effects of the electric quadruple moment on the spin-component quantum number can be seen in Figure 1.8 for an $I = \frac{5}{2}$ system.

For a central transition ($m_I = \frac{1}{2} \rightarrow m_I = -\frac{1}{2}$) the spectra will have the

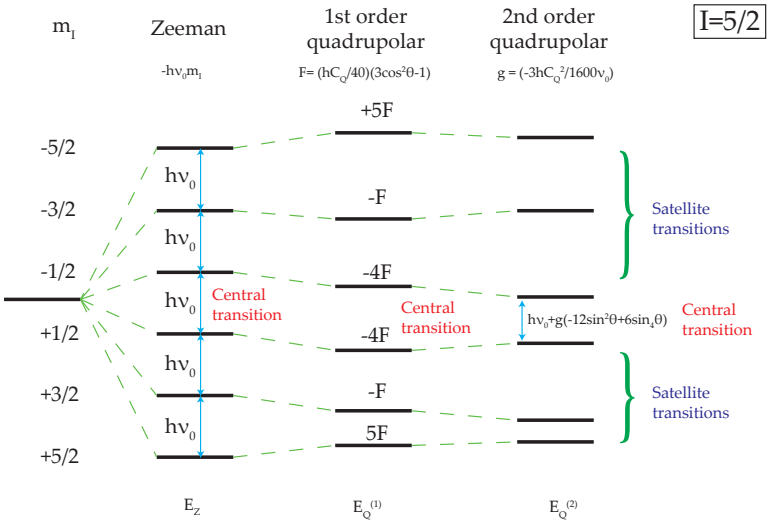

Figure 1.8: Energy level diagram for a spin 5/2 nucleus showing the effects of the Zeeman interaction and the quadrupolar interactions. ν_0 is the Larmor frequency and the energy changes are exaggerated.(Dupree [9]) $F = (hC_Q/40)(3\cos^2\theta - 1)$ and $g = (-3hC_Q^2/1600\nu_0)$

following simplified resonance frequencies,

$$\begin{aligned}
\nu_Q &= \nu_0^{(1)} + \nu_0^{(2)} \\
\nu_0^{(1)*} &= -\frac{3C_Q}{4I(2I-1)}\left(1-3\cos^2\theta\right) \\
\nu_0^{(2)*} &= -\frac{C_Q^2}{\nu_0} f(I)\left[\frac{3}{10}+\frac{6}{7}P_2(\cos\theta)-\frac{81}{70}P_4(\cos\theta)\right]
\end{aligned} \tag{1.27}$$

where due to the complicated form only the $\eta_Q = 0$ case is given. $f(I)$ is the spin dependant factor:

$$f(I) = \frac{I(I+1)-\frac{3}{4}}{[2I(2I-1)]^2} = \frac{2I+3}{16I^2(2I-1)} \tag{1.28}$$

The centre of gravity of the central transition of a powder pattern is mainly affected by $\nu_0^{(2)}$ and the magnitude of the effect is roughly given by the first term of the equation (1.27),

$$-\frac{(3+\eta_Q^2)C_Q^2}{10\nu_0} f(I) \tag{1.29}$$

There are four major techniques in order to eliminate the second-order effects on NMR spectra. First being the use of as high as possible magnetic field which will reduce the broadening since the broadening is proportional to $\frac{C_Q^2}{\nu_0}$. There are also dynamic angle spinning (DAS) (Llor and Virlet [73]) and double rotation (DOR) (Samoson et al. [74]) techniques which involve mechanical averaging of the second order broadening. The most recently developed technique, multiple quantum magic-angle spinning (MQMAS) (Frydman and Harwood [75], Medek et al. [76]), uses different second-order quadrupolar broadenings of the single and triple (or higher) transitions in order to average out the broadening. (Ashbrook and Wimperis [77]) In this study, high magnetic field and MQMAS techniques are used in order to overcome the quadrupolar interaction complications on the NMR spectra.

MQMAS experiment: This technique involves magic angle spinning (MAS) (explained in section 1.3.6) in order to average out the second term of the second-order quadrupolar interaction (see equation (1.25) and (1.26)). In order to average

out the third term (the fourth-degree Legendre polynomial part) in equation (1.25) we can use the multiple quantum transitions; for example in the $I = \frac{3}{2}$ system we use the $m_I = +\frac{3}{2} \rightarrow m_I = -\frac{3}{2}$ transition, also denoted as 3Q and the $m_I = +\frac{1}{2} \rightarrow m_I = -\frac{1}{2}$ transition, also denoted as 1Q. It is observed that the ratio of the constants of the fourth-degree Legendre polynomial, now defined as $A_{4(nQ)}$ with appropriate I and m_I, in the equation (1.25) is,

$$\frac{A_{4(1Q)}}{A_{4(3Q)}} = -\frac{54}{42} \tag{1.30}$$

Therefore if we let the spins evolve in different time periods in the single and multiple quantum dimensions, t_1Q and t_nQ, the second-order term, becomes zero, i.e. $\frac{t_{1Q}}{t_{3Q}} = \frac{42}{54}$.

Frydman *et al.* demonstrated that the dependence of ν_Q on coherence order, n in nQ which is $|m_I^+ - m_I^-|$ of the relevant transition, could be used to average out the second order interactions and developed the MQMAS experiment. (Frydman and Harwood [75], Medek et al. [76])

1.3.6 Magic-angle spinning

In solution state NMR experiments, the effects due to the chemical shift anisotropy and dipolar coupling are not observed directly. The angular dependencies of the quantities, i.e. $(3\cos^2\theta - 1)$ in equation (1.14) are averaged to zero due to the rapid tumbling of the molecules in solution and sharp peaks are generally observed. Magic-angle spinning (MAS) is a method that is devised to play the role of tumbling for solid samples. By spinning the sample around an axis at an angle $\theta_{MAS} = 54.74°$ (a value which makes $(3\cos^2\theta - 1)$ equal to zero) with respect to the external magnetic field at a rate higher than the size of the interaction, the measured NMR shifts average out due to pseudo-rapid-tumbling and sharp peaks are observed on a spectra.

In addition to the shielding tensor averaging, MAS experiments also allow the dipole-dipole magnetic interactions (equation (1.18)) to be averaged out. As discussed in the previous section (1.3.5), a nucleus with a spin larger than $\frac{1}{2}$ has a nuclear quadrupole coupling that depends on the EFG tensor at the nucleus. These quadrupolar intearctions can be simplified but not totally removed by MAS

experiments, and characteristic line shapes can be achieved as seen in Figure 1.7. Under MAS conditions, due to the $(3\cos^2\theta - 1)$ term, the second-order Legendre polynomial part of the electric quadrupole moment equation (1.25) will become zero and partially reduce the total quadrupolar broadening. It is apparent that rapid spinning in multiple angles in combination will result in further simplification of the quadrupolar nuclei NMR spectra, which is implemented in dynamic angle spinning (DAS) (Llor and Virlet [73]) and double rotation (DOR) (Samoson et al. [74]) techniques.

1.4 Computational Methods

Ab-initio DFT calculations with GIPAW formalism, and cluster expansion derived Monte Carlo simulations are used for *i*) The calculation of NMR parameters from structural models and *ii*) generating realistic, variable temperature structural models and simulation of phase transformations with increasing temperature. Further information about this section can be found in the following resources by Phillips [25], Bonhomme et al. [61] and Sholl and Steckel [78].

1.4.1 Density Functional Theory (DFT) calculations

The Born-Oppenheimer (also called adiabatic) approximation, introduced in 1927, allows the disentanglement of the atomic/ionic degrees of freedom from the electronic ones by considering that although the momenta of these particles are comparable, the ratio of the electronic mass to nucleus mass is very small ($m_e/M_I \leq 10^{-3}$). Therefore the time scale of atomic/ionic dynamics is much longer than the electronic one. This allows us to neglect the atomic/ionic kinetic energy when studying the electronic motion, so that we can solve the problem of N interacting electrons, considering fixed ions acting as an external potential V_{ext}.

Within the adiabatic approximation, the many-body Schrödinger equation that describes the quantum mechanical properties of a system of N_e electrons in the external potential of the nucleus reduces to,

$$H\psi_{\boldsymbol{R}}(r) = E(\boldsymbol{R})\psi_{\boldsymbol{R}}(r) \tag{1.31}$$

with the Hamiltonian,

$$H = -\sum_{i=1,N_e} \frac{\hbar^2}{2m_e}\nabla^2_{\boldsymbol{r}_i} + \frac{1}{2}\sum_{i\neq j}\frac{e^2}{|\boldsymbol{r}_i - \boldsymbol{r}_j|} - \sum_{i,I}\frac{Z_I e^2}{|\boldsymbol{r}_i - \boldsymbol{R}_I|} \tag{1.32}$$

where $\boldsymbol{R}_I$ and $\boldsymbol{r}_i$ are coordinates of the nuclei and electrons respectively, Z_I is the charge of the I-th nucleus and the electron charge and mass are e and m_e respectively. $\psi_{\boldsymbol{R}}(r)$ is the many-body wavefunction of electrons at fixed nuclear positions $\boldsymbol{R}$. The first term describes the electronic kinetic energy, T_e, the second term is for the electron-electron Coulomb interaction, U_{ee}, and the last term defines the external potential of nuclei V_{ext} and parametrically depends on nuclei positions. To this the direct ion-ion Coulomb interaction must also be added, which is just a constant term with respect to the electronic part, and will be neglected in the following discussion.

The electronic wavefunction $\psi_{\boldsymbol{R}}(r)$ is a function of all $3N_e$ electronic degrees of freedom supplemented by the spin degrees of freedom. Therefore the complexity of equation (1.31) increases exponentially with the number of electrons and solving it in order to obtain the ground state wavefunction becomes an intractable problem even for systems containing 100 atoms (a small nano scale system).

A numerically efficient and often successful approach to solve this problem is density functional theory (DFT). DFT was introduced in 1964 by Hohenberg and Kohn (HK) [79], who proved a one-to-one correspondence between an external potential V_{ext} and a non-degenerate ground-state electronic charge density $n_0(\boldsymbol{r})$:

$$n_0(\boldsymbol{r}) = \langle\psi_0(\boldsymbol{r}_1,\ldots,\boldsymbol{r}_N)|\sum_{i=1}^{N}\delta(\boldsymbol{r}-\boldsymbol{r}_i)\,|\psi_0(\boldsymbol{r}_1,\ldots,\boldsymbol{r}_N)\rangle \tag{1.33}$$

where ψ_0 is the non-degenerate ground state wavefunction. In other words, HK theory suggests not only that there is one possible ground-state density $n_0(r)$ for

each external potential V_{ext}, but also that there is only one external potential that has $n_0(r)$ as its ground-state density. Since the external potential also determines the many-body wavefunction of the ground state ψ_0, every observable of the system in its ground state can be expressed as a functional of the ground state electron density $n_0(r)$.

Therefore the ground state total energy as a functional of the electronic charge density is,

$$E[n_0(\boldsymbol{r})] = \langle\psi_0| H |\psi_0\rangle = F[n_0(\boldsymbol{r})] + \int_V d^3\boldsymbol{r} V_{ext}(\boldsymbol{r}) n_0(\boldsymbol{r}) \tag{1.34}$$

where the integral is over the volume of the system, V. The functional $F[n_0(\boldsymbol{r})]$ is the universal functional which is the integral of kinetic and interaction terms evaluated at the ground state. According to HK theorem, the minimum of the total energy functional $E[n(\boldsymbol{r})]$ occurs at the ground state charge density $n_0(r)$. Therefore, minimizing the total energy functional in (1.34) with respect to density $n(\boldsymbol{r})$, for a given number of electrons N, yields the ground state total energy and electronic density.

However the exact form of the kinetic and interaction density functional $F[n(\boldsymbol{r})]$ is not known. In 1965 Kohn and Sham [80] introduced a mapping of this many-body functional onto one of an auxiliary non-interacting electron system with the same ground state density and defined it in three separate contributions:

$$F[n] = T_s[n] + E_H[n] + E_{xc}[n] \tag{1.35}$$

The kinetic energy of the non-interacting system, $T_s[n]$, is given by

$$T_s[n] = \sum_i f_i \langle\psi_i| - \frac{\hbar^2}{2m_e}\nabla^2 |\psi_i\rangle \tag{1.36}$$

where f_i and ψ_i are the occupation and wavefunction of state i respectively. The classical Hartree electrostatic energy of a system with charge density n is

defined as:

$$E_H[n] = \frac{1}{2}\int d^3\boldsymbol{r}d^3\boldsymbol{r}'n(\boldsymbol{r})\frac{e^2}{|\boldsymbol{r}-\boldsymbol{r}'|}n(\boldsymbol{r}') \tag{1.37}$$

The remaining term, the so called exchange-correlation functional, E_{xc}, is defined as the remainder of equation (1.35). This is the term which holds all the many-body details of the system, after the mapping from the interacting to non-interacting system is performed. The energy functional associated with the external potential can also be written as:

$$E_{xc}[n] = \sum_i f_i \langle\psi_i| V_{ext} |\psi_i\rangle \tag{1.38}$$

We can now rewrite equation (1.34) as:

$$E[n] = T_s + E_H + E_{xc} + E_{ext} \tag{1.39}$$

and minimize this functional with respect to the orthonormal single particle wavefunctions ψ_i using Lagrange multipliers. The solution of this minimization leads to the Kohn-Sham equations

$$\left(-\frac{\hbar^2}{2m_e}\nabla^2 + V_{KS}(\boldsymbol{r})\right)\psi_i(\boldsymbol{r}) = \epsilon_i\psi_i(\boldsymbol{r}) \tag{1.40}$$

where the effective Kohn-Sham potential V_{KS} is defined as:

$$V_{KS} = V_{ext} + V_H + V_{xc} \tag{1.41}$$

with the Hartree potential,

$$V_H = \int d^3\boldsymbol{r}' n(\boldsymbol{r}) \frac{e^2}{|\boldsymbol{r} - \boldsymbol{r}'|} \tag{1.42}$$

and the exchange correlation potential is defined as the functional derivative of the exchange-correlation energy term,

$$V_{xc}(\boldsymbol{r}) = \left. \frac{\delta E_{xc}[n]}{\delta n(\boldsymbol{r})} \right|_{n(\boldsymbol{r})=n_0(\boldsymbol{r})} \tag{1.43}$$

Therefore from the solution of the KS equations one can obtain the auxiliary one electron wavefunctions, ψ_i, and construct the ground state density through

$$n_0(\boldsymbol{r}) = \sum_i f_i |\psi_i(\boldsymbol{r})|^2 \tag{1.44}$$

Based on these single particle equations, one can interpret the KS scheme as a mean-field approach where an electron is affected by the potential of the surrounding nuclei and interacts with other electrons through the charge density. Therefore the ground state charge density depends on the single particle solutions, which in turn, depend on the density. The solution can be achieved via a self-consistent iterative procedure or via global minimization strategies such as the conjugate gradient (Stich et al. [81]). In this study we use a self-consistent iterative procedure.

The DFT theory explained so far is exact within Born-Oppenheimer approximation, but not useful since the analytical expression for the exchange correlation density functional, E_{xc}, is not known. A critical step in DFT is to replace this unknown functional with an approximation. The first and simplest approach to be proposed was the Local Density Approximation (LDA) where the exchange correlation energy density of a homogeneous gas of interacting electrons with constant charge density, $\varepsilon_{xc}^{hom}(n)$, was used as an approximation for the non-homogeneous system at hand:

$$E_{xc}[n(\boldsymbol{r})] = \int_V d^3\boldsymbol{r}\varepsilon_{xc}^{hom}(n(\boldsymbol{r}))n(\boldsymbol{r}) \tag{1.45}$$

where $\varepsilon_{xc}^{hom}(n)$ is a well defined function that can be calculated using Monte Carlo simulations (Ceperley and Alder [82]).

Since the beginning of DFT, many functional forms have been proposed for the exchange correlation energy density. The Local Density Approximation (LDA), as proposed by Kohn and Sham, has been used in several early works. Different interpolation schemes have been proposed for ε_{xc}^{hom}, such as the one of Perdew and Zunger [83], and are still in use. A significant step that improved the performance of DFT was the proposal of Perdew and Wang in 1991 [84]. They introduced a new functional form which depends not only on the local density but also on its gradient, which is better known today as the Generalized Gradient Approximation (GGA). GGA improved successfully the shortcomings of LDA especially for systems with strong inhomogeneities in charge density. Many different reformulations and extensions of GGA have been proposed and tested over the years. One of the most commonly used GGA functionals in the condensed matter community is the PBE functional, proposed by Perdew, Burke, and Ernzerhof [85]. A revision of PBE was suggested by Zhang and Yang and demonstrated improved atomic energies for several elements [86]. In this study due to its wide spread use and proven robustness the PBE functional is used.

Bloch's theorem and periodic boundary: For any realistic crystal, such as perfect crystals, the total number of electrons is huge. Hence the DFT calculations with electronic energy density would become very difficult. Therefore it is desirable to use the symmetry of crystals, at least the translational symmetry, to represent the whole in a smaller set, a unit cell under periodic boundary conditions. Felix Bloch in his 1928 thesis (Quantum mechanics of electrons in crystal lattice) and following publication [87] states that if the potential has a lattice periodicity, then the eigenstates of the single-particle Hamiltonian are

$$\Psi_{n,\boldsymbol{k}}(\boldsymbol{r}) = e^{i\boldsymbol{k}\cdot\boldsymbol{r}} u_{n,\boldsymbol{k}}(r) \tag{1.46}$$

where $u_{n,\boldsymbol{k}}$ is a periodic function and $u_{n,\boldsymbol{k}}(\boldsymbol{r}) = u_{n,\boldsymbol{k}}(\boldsymbol{r} + \boldsymbol{R})$ for all lattice vectors $\boldsymbol{R}$. These Bloch states are labelled by their crystal momentum $\boldsymbol{k}$. The unique values of $\boldsymbol{k}$ are in the reciprocal unit cell, within the first Brillouin Zone.

With this theory we convert the problem of an infinite number of electrons to a finite number of bands and infinite number of $\boldsymbol{k}$-points. Thanks to the fact that physical properties change smoothly with $\boldsymbol{k}$, many integrals can be greatly approximated by a finite sampling of $\boldsymbol{k}$. A common scheme for Brillouin zone integration consists of the sets of regular integration grids introduced by Monkhorst and Pack.[88]

The plane wave basis set: To be able to numerically solve the eigenvalue problem in the Kohn-Sham equation (1.40), the eigenstates must be represented by some basis set. While there are many possible choices, the one made here is to use planewaves as the basis. There are many advantages to the use of planewaves: they form a mathematically simple basis, they naturally incorporate periodic boundary conditions, and, perhaps most importantly, planewave calculations can be taken systematically to convergence as a function of the size of the basis. The Kohn-Sham eigenstates are expressed as

$$\Psi_{n,\boldsymbol{k}}(\boldsymbol{r}) = \sum_{\boldsymbol{G}} c_{n,\boldsymbol{k}}(\boldsymbol{G}) e^{i(\boldsymbol{k}+\boldsymbol{G})\cdot\boldsymbol{r}} \tag{1.47}$$

where the sum is over all reciprocal lattice vectors $\boldsymbol{G}$, and the $c_{n,\boldsymbol{k}}(\boldsymbol{G})$ are the coefficients to be determined for solving the Kohn-Sham equation (1.40). The basis set is then truncated by including only a limited number of reciprocal lattice vectors, defined within a sphere with a radius defined by the cutoff energy, E_{cut}

$$\frac{\hbar^2|\boldsymbol{k}+\boldsymbol{G}|^2}{2m} \leq E_{cut} \tag{1.48}$$

In this way the basis set is defined by the maximum kinetic energy component. Physical quantities such as the formation energy of the cell can be converged by iterative computations and an increase of the cutoff energy. The upper limit of the cutoff energy is the inclusion of the ghost states (states with a wrong number of nodes) which can be detected by vibrational frequency calculations and checking for negative vibrations.

The Pseudopotential approximation: Electrons in atoms can be roughly grouped into two. The core electrons, which are nearer to the nucleus and in general do not interact with the nearby atoms, and the valence electrons, which are responsible for all the chemistry as they interact with the nearby atoms. Due to their higher spherical symmetry core electrons can be represented by simpler functions rather than complicated wave functions in turn reducing the number of electronic degrees of freedom and reducing the computational time and resources required. With the pseudopotential approximation a much smaller number of planewaves are required to represent the valence wavefunctions. Common pseudopotentials are the norm-conserving potentials (Troullier and Martins [89]) and the Vanderbilt ultrasoft potentials (Vanderbilt [90]). Here in this study we used Vanderbilt ultrasoft pseudopotentials which require smaller cutoff energies in general and hence have less problems with having ghost states.

1.4.2 Gauge including projector augmented wave (GIPAW) calculations

GIPAW method is a way of calculating NMR parameters in crystalline materials based on DFT. The success of the method arises from the compensation for the problems sourced from the translational symmetry of crystals. Different from the molecule-based methods, GIPAW incorporates pseudopotential approximation with the use of projector augmented wave and can deal with heavier atoms

that have many core electrons. GIPAW was introduced by Mauri and Pickard in 2001 [62]. The following sections related to GIPAW are derived from detailed descriptions by Yates et al. [91] and more practical information can be found in the following review articles by Harris et al. [92] and by Charpentier [60].

Shielding in a periodic system: A uniform external magnetic field applied to a material generates an electric current in it due to motion of atomic and sub-atomic particles. An insulating, non-magnetic material has only the electronic motion in orbitals contributing to the electric current. This electronic current density $\boldsymbol{j}(\boldsymbol{r})$, produces an induced magnetic field $\boldsymbol{B}_{induced}(\boldsymbol{r})$, in the opposite direction of the external magnetic field, which is described by the Biot-Savart law as,

$$\boldsymbol{B}_{induced}(\boldsymbol{r}) = \frac{\mu_0}{4\pi} \int d^3r' \boldsymbol{j}(\boldsymbol{r'}) \times \frac{\boldsymbol{r} - \boldsymbol{r'}}{|\boldsymbol{r} - \boldsymbol{r'}|^3} \tag{1.49}$$

The reducing effect of the induced magnetic field hence can be represented by the external magnetic field and a shielding component, the magnetic shielding tensor, $\boldsymbol{\sigma}(\boldsymbol{r})$.

$$\boldsymbol{B}_{induced}(\boldsymbol{r}) = -\boldsymbol{\sigma}(\boldsymbol{r})\boldsymbol{B}_{external} \tag{1.50}$$

Therefore if we can calculate the shielding tensor we can calculate the induced electronic current. One way is to use perturbation theory since the Zeeman interactions, eq. (1.3), are small as compared to the total energy of the system in the Hamiltonian, eq. (1.32). Under an external magnetic field, when applying the first order perturbation, we have to keep quantities linear as marked with the superscript "lin" in following equations.

$$\boldsymbol{j}^{lin}(\boldsymbol{r'}) = 2\sum_i \left[\left\langle\psi_i^0\right| \mathbf{J}^p(\boldsymbol{r'}) \left|\psi_i^{lin}\right\rangle + \left\langle\psi_i^{lin}\right| \mathbf{J}^p(\boldsymbol{r'}) \left|\psi_i^0\right\rangle\right] + 2\sum_i \left\langle\psi_i^0\right| \mathbf{J}^d(\boldsymbol{r'}) \left|\psi_i^0\right\rangle \tag{1.51}$$

where the multiplicity of 2 is due to spin degeneracy and the current operator. The summation is over the whole occupied states "i". The $\mathbf{J}(\boldsymbol{r'})$, is the sum of the paramagnetic (superscript p) and the diamagnetic (superscript d) terms as described by,

$$\mathbf{J}(\boldsymbol{r'}) = \mathbf{J}^p(\boldsymbol{r'}) + \mathbf{J}^d(\boldsymbol{r'}) \tag{1.52}$$

Using these expressions, a symmetric gauge, linear-order Hamiltonian and the Greens function expression one can write an equation (here the resultant paramagnetic current pseudo-operator is denoted as $\mathbf{J}_G^p$) of the induced current with respect to the ground state charge density, $\rho(r')$ and the external magnetic field, $\mathbf{B}_{ext}$.

$$\boldsymbol{j}^{lin}(\boldsymbol{r'}) = \frac{4e}{m_e}\sum_i Re\left[\left\langle\psi_i^0\right| \mathbf{J}_G^p \left|\psi_i^0\right\rangle\right] \cdot \mathbf{B}_{ext} - \frac{e^2}{2m_e}\rho(\boldsymbol{r'})\mathbf{B}_{ext} \times \boldsymbol{r'} \tag{1.53}$$

Where R are the coordinates of the center of an atom, and m_e and e are respectively the mass and the charge of an electron. This is the main equation for calculating the chemical shielding, one of the NMR parameters. Now we can apply this equation to a crystalline system with periodicity, and improve computability with the following implementations.

Position operator problem: The equation (1.53) can be easily used for a finite system calculation. However in the crystalline system the diamagnetic part (which does not have first-order perturbation and only depends on the charge

density) will cause a divergence in the calculation of the induced current, due to $\boldsymbol{r} \neq 0$ in the long range. Thankfully with the increase of $|\boldsymbol{r}|$ the paramagnetic part (involving the first-order perturbation) also causes a divergence in the opposite direction. With a gauge inclusion which keeps track of the origin of the system two parts can be combined. Therefore only the sum of these terms result in a meaningful value, and paramagnetic and diamagnetic parts should not be used separately. With inclusion of the Bloch's periodic boundary conditions and the application of the method to an insulator (the Green's function is localized hence induced current remains finite at large $\boldsymbol{r}$) we achieve a reproducible inductive current representation and in turn a reproducible chemical shielding value.

Core states and Pseudopotentials: The chemical shielding calculations can be performed much faster, if the core electrons are separated from the valence electrons and treated separately to be added later into the total chemical shielding, which is proven to be correct by Gregor et al. [93] if the core and valence shell electrons are separated in a gauge invariant way. Hence for the core shielding one can place the gauge origin onto the center of the atom making the shielding diamagnetic and calculable by the Lamb formula,

$$\sigma_{ij} = \delta_{ij} \frac{\mu_0 e^2}{4\pi m_e} \int d^3 r \frac{n(\boldsymbol{r})}{r} \tag{1.54}$$

Calculations for valence shielding using pseudopotentials as they are results in pure shielding. One must reproduce core electrons for the valence shell shielding calculations which is achieved with projector augmented waves (PAW) as shown by Yates et al. [91].

Chemical shielding: As a result of lengthy induced current calculations we achieve the following absolute chemical shielding equation,

$$\sigma = \sigma_{core} + \sigma_{bare} + \sigma_{\Delta d} + \sigma_{\Delta p} \tag{1.55}$$

Where σ_{core} is the isotropic contribution of the core electrons, σ_{bare} is the

contribution from the pseudo-valence wave function and $\sigma_{\Delta d}$ and $\sigma_{\Delta p}$ are the contributions from the reconstruction of the core interaction with the projector augmented wave.

GIPAW model calculations are compared with all electron calculations and show excellent agreement in results for broad variety of nuclei, where electronic properties of respective atoms can be well described with the DFT calculations, such as for protons, boron, nitrogen, oxygen, silicon (Yates et al. [91]), sodium, aluminium, silicon (Profeta et al. [94]) and phosphorus.

Electric field gradient calculations: The electric quadruple moment can be calculated as discussed in section 1.3.5 using the equations (1.19) and (1.20). Practically, the first method involves using the Q values from the study by Pyykkö [95] with the V_{ZZ} value in the quadruple moment tensor being observed from the GIPAW calculations. The second method would be a fit of experimental C_Q values to the GIPAW calculated V_{ZZ} values, keeping the Q as a variable. Here we used the tabulated values from Pyykkö [95] as implemented in GIPAW without any change.

1.4.3 Cluster expansion and Monte Carlo simulations

Monte Carlo simulation: Monte Carlo simulations (MC) are used to investigate physical and chemical properties of both doped and pure systems under variable temperature. Predicted properties include, but are not limited to, phase stability and atomic order-disorder behaviour.

A Monte Carlo simulation generates configurations of a system by making random changes to the positions of the species present, in our case the type of the species in an idealized lattice model (see Figure 1.9) is switched between suitable pairs, i.e. oxygen-vacancy and indium-gallium. The MC uses an *importance sampling* technique which finds states of low energy, as this enables properties to be calculated accurately. Importance sampling is introduced by Metropolis et al. [96] in the Metropolis algorithm where outcome of each trial depends only on the preceding trial and not on any previous trials allowing us to find structural models for high temperatures.

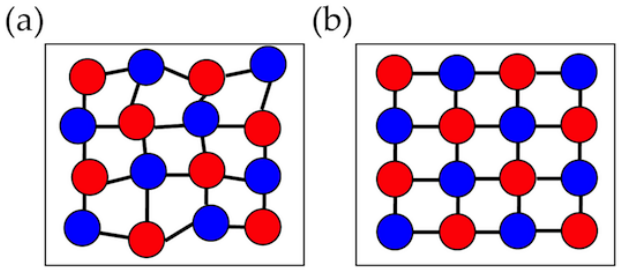

Figure 1.9: Schematics of (a) real and (b) idealized lattices, where blue and red circles represent the distinct possible ion types or vacancies.

Cluster expansion: First principles, DFT, energy calculations of the large supercells needed for Monte Carlo simulations would be too slow and even impossible due to the size of supercells. However the cluster expansion (CE) is a method of calculating structural energies for very large supercells with minimal resources, based on first principles calculations of smaller unit cells. CE approximates the real distorted crystal structure as an idealized lattice of appropriate symmetry (Figure 1.9), where the various inter-ionic interactions and importantly, the local structural distortions are incorporated into a set of effective cluster interactions (ECIs) (Farrell et al. [97]). The CE approach has been shown to work particularly well in alloy systems, where there is often no orientational dependence of inter-site interactions. Here the CE method is applied to a strongly ionic oxide with significant directionality of bonding, to the effect that such a system must be parametrized with many more structural configurations than for the average metallic alloy.

The CE (Sanchez et al. [98], de Fontaine [99], Zunger [100]) for a binary substitution upon a single sublattice may be written in the form,

$$E(\sigma) = E_0 + \sum_i V_i \sigma_i + \sum_{ij} V_{ij}(\sigma_i \sigma_j) + \sum_{ijk} V_{ijk}(\sigma_i \sigma_j \sigma_k) + \ldots \tag{1.56}$$

$$\sigma = -1 \; for \; blue \; site$$

$$\sigma = +1 \; for \; red \; site$$

where $E(\sigma)$ is the CE-representation of the energy, σ is the configuration of a site, e.g. for oxygen-vacancy (O-Vac) binary substitution, σ may assume $+1$ for having O in crystallographic sites and -1 for having the counterpart, Vac, configuration, the series of V-values represent the interaction coefficients or ECIs for site clusters upon the oxygen and indium sub-lattices (V may represent points V_i, pairs V_{ij} etc). The expansion is mathematically complete in the sense that if all terms are included then the expansion is exact, although in practice it is truncated at a manageable number of terms. When considering which terms to include in the expansion, clusters are usually ordered in importance by increasing number of components (triplets are less important than pairs) and separation of sites, since the larger clusters tend to have less physically important interactions. Clusters related by symmetry operations of the parent lattice will possess equal ECIs. The ECIs are fitted so as to reproduce as closely as possible a set of values of target energy (TE) for different configurations by application of standard linear regression methods Kutner et al. [101] TE represents a ground state total energy for a fully optimized configuration obtained here from first principles electronic structure calculations. Error in the fitting is measured by a cross-validation (CV) score that yields the formation energy per site as described by van de Walle et al. [102].

Further information about the CE and the MC simulations can be found in articles by van de Walle and Ceder [63], van de Walle et al. [102], van de Walle and Asta [103], van de Walle and Ceder [104] and the book, Molecular Modeling Principles and Application, by Leach [105].

Chapter 2

Structural Characteristics of $Ba_2In_2O_5$ via Experimental and Computational ^{17}O Solid State NMR

2.1 Introduction

Perovskites are a broad class of materials that find widespread application, notably here as electrolytes for intermediate temperature fuel cells as a consequence of their high O and, when hydrated, their even higher proton conductivities.(Malavasi et al. [106]) They are increasingly recognized as competitors to more conventional electrolyte phases such as yttria-stabilized zirconia (YSZ) and other fluorite-structured compounds. The structural family possesses the ABO_3 stoichiometry where the A-cations are typically rare-earths- or alkaline-earths; and the B-cations, transition metals or semi-metals (Adler et al. [34]) of varying oxidation states and ionic radii. The B-site cations are each bonded to six O ions to form corner-sharing BO_6 octahedra, while the A-site cations occupy the cubic space delimited by eight BO_6 units, and in turn coordinate with twelve nearest-neighboring O ions. Anisotropic expansion of the unit cell and significant tilting of the octahedra may occur as a function of relative size of the cations. The tun-

ing of such distortions may potentially lead to increased ionic conductivity due to change of total lattice energies or more specifically variation in bottlenecks for diffusion of a given structure.(Woodward [35]) The ideal perovskite structure manifests a simple cubic cell with space group $Pm\bar{3}m$. Doping with lower valent cations typically introduces compensating extrinsic O vacancies, and constitutes the most frequently pursued strategy to synthesize phases with increased ionic conductivity.

The present chapter focuses on the $Ba_2In_2O_5$ defect perovskite phase, a material that has O ion conductivity significantly exceeding that of YSZ (Goodenough et al. [7]) in the high temperature cubic phase, and protonic conductivity at 180°C temperature if hydrated.(Adler et al. [1], Jayaraman et al. [3], Goodenough et al. [7], Kendall et al. [38], Islam et al. [40], Prasanna [41], Mohn et al. [42], Yoshinaga et al. [43], Hashimoto [44], Rolle et al. [45], Kharton et al. [107]) The compensation of the Ba_2^+ and In_3^+ cation charges in $Ba_2In_2O_5$ requires the removal of one-sixth of the O atoms in the perovskite structure, yielding a high intrinsic concentration of O vacancies. The vacancies order at room temperature into an orthorhombic structure with space group $Ibm2$. (Colville and Geller [10], Gregory and Weller [11]) Three crystallographically-distinct O sites result, ordered so as to form alternating layers of tetrahedral (Tet, Tet') and octahedral (Oct) In_3^+ centered polyhedra, with successive (010) tetrahedral layers offset from one another in an $\cdots OctTetOctTet'\cdots$ staggered O vacancy pattern (Figure 2.1a). The labeling adopted hereafter has O1 anions at the equatorial positions of the octahedra; O2, bridging octahedral and tetrahedra; and O3, within the tetrahedral layer. The structure is termed brownmillerite after the original Ca_2FeAlO_5 mineral manifesting a similar arrangement of O vacancies. (Colville and Geller [10]) The $Ba_2In_2O_5$ structure has been described by using a variety of space groups. Gregory and Weller used the $Ibm2$ space group (Gregory and Weller [11]) while both the $Pnmm$ and $Icmm$ space groups have been suggested based on other brownmillerite systems. (Steele [46]) The structure shown (Figure 2.1a) corresponds to the $Ibm2$ structure. Fischer et al. [48] chose to refine the structure in the $Ima2$ space group (an equivalent space group with a different setting to the $Ibm2$ (no. 46)) and derived a structure that is related to the $Ibm2$ structure but differing slightly in terms of the In-O bond distances and distortions of the InO_6

octahedra, but the octahedral tilt directions were unchanged. Speakman et al. [12] and Berastegui et al. [13] performed refinements in both the $Ibm2$ and $Icmm$ space groups, using neutron and X-ray diffraction data, these two space groups yielding more satisfactory fits to the data than any performed using other possible brownmillerite space groups. They eventually rejected the $Ibm2$ structure in favor of an $Icmm$ (no. 74) solution, based on slightly lower $\chi^2/\mathrm{R_w}-$ factors values, a better fit to a series of weaker reflections, and more satisfactory site occupancies. (Speakman et al. [12], Berastegui et al. [13]) The resultant structure, is however, disordered, with partial occupancy of In(2) and O3 on the $8i$ positions. Mohn et al. [42] explored these structures by DFT calculations and identified a first high energy state at a relative energy difference of 5.0 $kJmol^{-1}$, with an $\cdots OctTetOctTet\cdots$ stacked O vacancy pattern (Figure 2.1b). Thus, the structural and theoretical studies suggest that the room temperature itself may contain a degree of disorder in the tilting of the octahedra and/or the oxygen/cation occupancies.

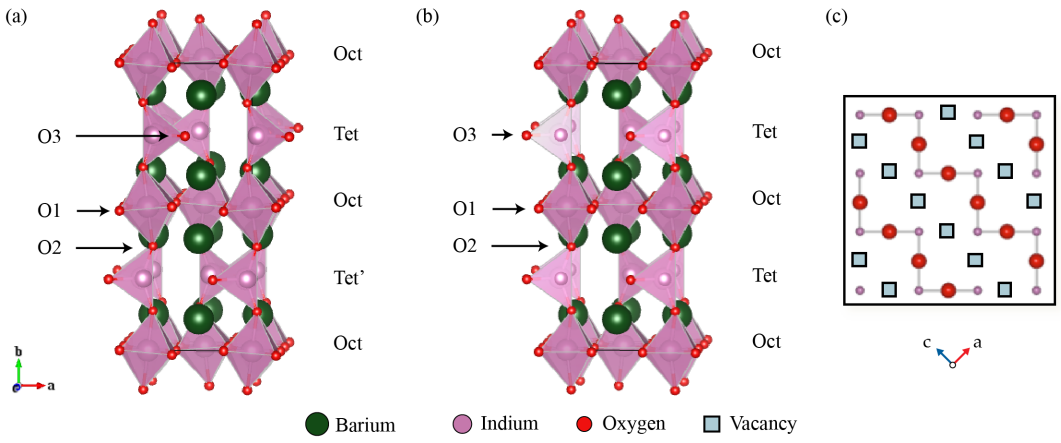

Figure 2.1: Room temperature crystal structure of (a) ground state orthorhombic brownmillerite $Ba_2In_2O_5$ in space group $Ibm2$ with $\cdots OctTetOctTet'\cdots$ staggered O vacancy pattern and (b) the first high energy state $\cdots OctTetOctTet\cdots$ stacked O vacancy pattern. (Colville and Geller [10], Gregory and Weller [11]) (c) A schematic representations of the O3 layer, showing the O3 vacancy ordering.

$Ba_2In_2O_5$ undergoes a series of phase changes from the room temperature orthorhombic structure just described, to a tetragonal form (in space group $I4cm$) above 925°C, in which the O3 sites and the vacant site exchange, and subsequently to a disordered cubic phase above approximately 1040°-1075°C. (Speakman et al. [12], Steele [46]) It is only in the tetragonal and cubic forms that the material displays substantial ionic conductivity. (Goodenough et al. [7], Speakman et al. [12]) Conductivity data for $Ba_2In_2O_5$ was reported by Goodenough et al. [7]. While the large number of O vacancies in the tetrahedral layers of $Ba_2In_2O_5$ might be thought to be conducive to rapid anion conduction, freezing of the vacancies in the low temperature orthorhombic phase allows for only limited O motion. Hydration of the $Ba_2In_2O_5$ at moderate temperatures results in a tetragonal structure with space group $P4/mbm$ where the intrinsic vacancies of $Ba_2In_2O_5$ in the O3 layer are fully occupied by the water O atoms as further described in the following chapter 4.

Previous static high temperature ^{17}O solid-state NMR measurements by Adler et al. [1] observed three ^{17}O resonances at room temperature: two very broad peaks that were attributed to the O1 and O2 environments, and a narrow peak at 220 ppm assigned to the O3 environment. The peak broadening and line shapes of the O1 and O2 environments were ascribed to second-order quadrupolar effects arising out of the highly asymmetric distributions of charge at these sites. The narrow third resonance was shown to nutate on the order of liquid $H_2^{17}O$, and was attributed to a site lying upon a crystallographic inversion center (in space group $Pcmn$, the space group used in the earlier refinements of this structure by Bertaut et al. [108]). However, as discussed above, Speakman et al. [12] and Berastegui et al. [13] subsequently showed that $Ba_2In_2O_5$ crystallizes in an orthorhombic structure with space group $Ibm2$ or $Icmm$ rather than $Pcmn$, both space groups lacking an inversion center, suggesting that the previous assignment of the ^{17}O NMR spectra of $Ba_2In_2O_5$ was based on an inaccurate crystallographic model. Furthermore, the presence or lack of inversion symmetry does not necessarily imply a non-zero quadrupole coupling constant, C_Q, so the origin and assignment of this third resonance remains unclear.

Brownmillerite $Ba_2In_2O_5$ has also been the subject of a number of prior theoretical studies, largely focused on understanding the oxygen transport mecha-

nisms and phase transformations and the structure of the hydrated phase. (Martinez et al. [20], Islam et al. [40], Mohn et al. [42], Fisher et al. [47], Fisher and Islam [109], Kanzaki and Yamaji [110]) Of particular relevance to this work, Mohn et al. [42] performed a comprehensive treatment of the energy hypersurface of a 36-atom supercell of $Ba_2In_2O_5$ within a series of periodic density functional theory (DFT) calculations and showed that the orthorhombic structure having a stacking of O vacancies in a staggered fashion (Figure 2.1a) is favored over the stacked structure (Figure 2.1b) as discussed earlier, (Mohn et al. [42, 111]) and in agreement with the experiments.(Gregory and Weller [11]) Optimizations of all crystallographically non-equivalent configurations in a reasonable supercell provided static thermodynamic parameters directly, revealing in particular that the low energy minima all conserve the 50% tetrahedral In and 50% octahedral In alternating layer motif.

The current work re-examines $Ba_2In_2O_5$ using current solid state ^{17}O NMR spectroscopy techniques, applying higher field strengths than previous studies and two-dimensional multiple-quantum magic angle spinning (MQMAS) experiments (Frydman and Harwood [75], Medek et al. [76]), a technique that was unknown when the previous ^{17}O NMR studies of $Ba_2In_2O_5$ was reported by Adler et al. [1] and which allows for high-resolution solid state NMR spectra of quadrupolar nuclei (such as ^{17}O, spin $I = 5/2$) to be obtained. The application of a similar approach to the hydrated $Ba_2In_2O_5$ [i.e. $Ba_2In_2O_4(OH)_2$] phase will be presented in the subsequent chapter 4. First principles periodic DFT NMR calculations within the gauge-including projector augmented wave (GIPAW) approach (Pickard and Mauri [62]) are also performed, providing a robust interpretation of the experimental spectra assignments. Similar theoretical approaches have previously been fruitfully applied to a very large range of systems,(Charpentier [60], Gervais et al. [112], Wong et al. [113], Salager et al. [114]) relevant studies of perovskites including the ^{17}O and ^{29}Si spectra of the $MgSiO_3$ perovskite, (Ashbrook et al. [115]) the multinuclear ^{23}Na and ^{93}Nb MQMAS spectra of the $NaNbO_3$ and $NaTaO_3$ perovskites by Ashbrook et al. [116], Johnston et al. [117, 118], a recent work on doped $LaGaO_3$ by Blanc et al. [119, 120] and $BaSnO_3$ by Buannic et al. [121] perovskites. In this chapter we first present the DFT and GIPAW calculations of $Ba_2In_2O_5$, examining a series of energetically similar structures. These calcu-

lations then helped to assign the experimental ^{17}O NMR results.

2.2 Materials and Methods

2.2.1 Experimental

Sample preparation: $Ba_2In_2O_5$ powder was prepared by a solid state route (West [122]) using stoichiometric quantities of $BaCO_3$ (Sigma-Aldrich, $\geq$ 99%) and In_2O_3 (Sigma-Aldrich, 99,99% trace metals basis) which were first ground in a planetary ball mill (Retsch PM100) at 600 rpm for 4 hours. $Ba_2In_2O_5$ was then pelletized, sintered at 1300°C for 24 hours and re-ground by agate mortar and pestle , these steps were repeated until a pure phase was obtained as determined by powder X-ray diffraction (Figure 2.2). ^{17}O enriched $Ba_2In_2O_5$ was obtained by heating dry $Ba_2In_2O_5$ (dried at 900°C under vacuum for 12h) in 50% ^{17}O enriched O_2 gas (Isotec, 99%, used as received) in a sealed quartz tube at 1000°C for 24 hours.(Ashbrook and Smith [123]) Powder X-ray diffraction patterns were obtained on Panalytical Empyrean and Bruker D8-Focus X-ray diffractometers using Cu K_α radiation ($\lambda = 1.5418$Å) (see Figure 2.2).

Solid State NMR Spectroscopy: Solid state ^{17}O MAS NMR experiments on ^{17}O enriched $Ba_2In_2O_5$ were performed on a 9.4 T Bruker Avance 400 MHz spectrometer using a Bruker 4 mm HX probe, a 11.7 T Oxford magnet with a Varian Infinity Plus 500 MHz spectrometer using a Chemagnetics 4mm HX probe, a 14.1 T Bruker Avance 600 MHz spectrometer using a Bruker 4 mm HFX probe, and finally a 21.1 T Bruker Avance II 900 MHz spectrometer equipped with a 3.2 mm HX probe. Spectra were recorded using a $\sim \pi/2$ pulse length of 1.2 μs at a radio frequency (RF) field amplitude of ~70 kHz and a MAS frequency of 15 kHz at 9.4, 11.7, 14.1 T, and of $\sim 2\mu s$ at a RF field amplitude of ~40 kHz and a MAS frequency of 20 kHz at 21.1 T. The ^{17}O two dimensional (2D) triple-quantum MAS (3QMAS) (Amoureux et al. [52], Frydman and Harwood [75], Medek et al. [76]) z-filter experiment of ^{17}O enriched $Ba_2In_2O_5$ was carried out at 14.1 T and at a MAS frequency of 13 kHz. Twenty-eight t_1 increments of 1024 scans were co-added. Hard and soft pulses were performed at RF fields of

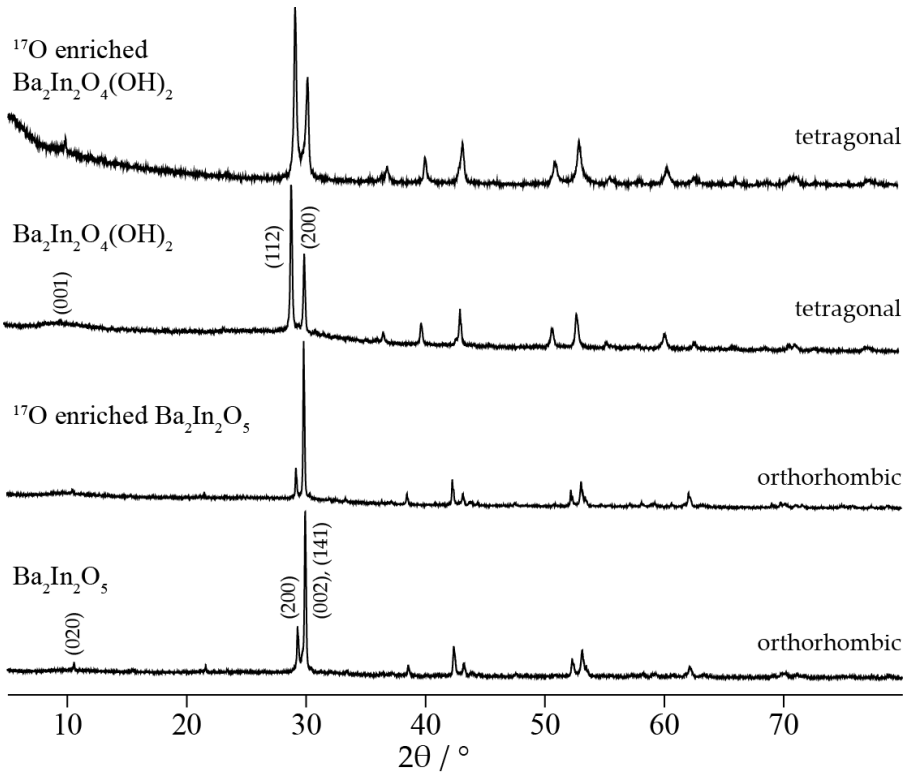

Figure 2.2: Powder X-ray diffraction patterns of $Ba_2In_2O_5$, ^{17}O enriched $Ba_2In_2O_5$, $Ba_2In_2O_4(OH)_2$ and ^{17}O enriched $Ba_2In_2O_4(OH)_2$. The unit cell is given on the right. The broad component in $Ba_2In_2O_4(OH)_2$ observed at low 2θ has been observed previously. (Jayaraman et al. [3])

∼80 and ∼10 kHz, respectively. All ^{17}O NMR data were collected on freshly ^{17}O enriched sample and packed in ZrO_2 rotor. A recycle delay of 10 s was used for all experiments averaging from ∼6500 to ∼30000 scans. ^{17}O chemical shifts were externally referenced to water at 0.0 at 20°C. NMR data were processed using the Bruker TopSpin 3.0 (BRUKER [124]) package, and the MatNMR (van Beek [125]) package, the latter running on MatLab. Simulations and deconvolutions were also performed using the TopSpin 3.0 and the MatNMR packages.

2.2.2 Computational Methods

Energetics and configurations: The first principles solid-state electronic structure calculations used here are similar to those used in various recent studies of oxides and gallates,(Middlemiss et al. [126]) perovskites (Johnston et al. [118], Blanc et al. [119], Buannic et al. [121], Barrow et al. [127]) and pyrochlores (Reader et al. [128], Mitchell et al. [129]), and were all performed within the CASTEP code (Clark et al. [130]). Full structural optimisations (both cell and atomic positions) of $Ba_2In_2O_5$ were performed in the absence of any symmetry constraints (i.e. space group $P1$), a plane wave kinetic energy cut-off of 40 Ry ($\sim 53 MJmol^{-1}$) and a linear spacing of 0.04 $Å^{-1}$ or smaller for the reciprocal space sampling mesh, yielding Monkhorst-Pack meshes of dimension $5 \times 2 \times 5$ for the $Ba_8In_8O_{20}$ supercell. All the geometry parameters (Table 2.1) reported subsequently were averaged from five $\cdots OctTetOctTet' \cdots$ (Figure 2.1a) and four $\cdots OctTetOctTet \cdots$ (Figure 2.1b) $Ba_2In_2O_5$ optimized configurations, proceeding initially from configurations in which the unit cell size and atomic position were randomly perturbed in a 0.0 to 0.1Å distance range. Resultant optimized configurations for both $\cdots OctTetOctTet' \cdots$ and $\cdots OctTetOctTet \cdots$ sets have $0.2 kJmol^{-1}$ energy deviations within sets and $5.0 kJmol^{-1}$ energy difference between two sets, $\cdots OctTetOctTet' \cdots$ being the lower energy set. Full representation of all these structures is detailed in the Appendix A.1. The Perdew-Burke-Ernzerhof GGA-type exchange-correlation functional has been used throughout. (Perdew et al. [85]) Convergence of total energy with respect to numerical parameters was estimated at $0.2 kJmol^{-1}$ per atom or better. The optimisation was pursued until energy difference, maximum atomic force, maximum atomic

displacement and maximum stress tensor component fell below tolerances of 1×10^{-6}eV, 1×10^{-3}eVÅ^{-1}, 1×10^{-3}Å and 5×10^{-3}GPa, respectively. The effect of decreasing the tolerances listed above by a further order of magnitude was investigated, yielding only minimal changes in geometry and computed NMR parameters.

NMR Calculations: Fully periodic calculations of NMR parameters within the gauge-including projector augmented wave (GIPAW) method (Pickard and Mauri [62], Yates et al. [91]) have been performed using the CASTEP code, including determinants of electric field gradient tensors and associated quadrupolar interaction parameters for ^{17}O sites. ([94]) The NMR parameters were obtained from a single point calculation within the optimised geometry, differing only from the earlier optimizations in that a larger basis set cut-off of 60 Ry ($\sim 79 MJmol^{-1}$) was applied. The isotropic shielding was obtained as $\sigma_{iso} = \frac{1}{3}(\sigma_{xx} + \sigma_{yy} + \sigma_{zz})$, where σ_{xx}, σ_{yy} and σ_{zz} are the principal components of the shielding tensor, ordered such that $|\sigma_{zz} - \sigma_{iso}| \geq |\sigma_{xx} - \sigma_{iso}| \geq |\sigma_{yy} - \sigma_{iso}|$. The chemical shift δ_{iso} is then derived from the computed site shielding σ_{iso} by application a shielding reference σ_{ref} with the expression $\delta_{iso} = \sigma_{ref} + m\sigma_{iso}$. Both σ_{ref} and m for ^{17}O are obtained from a previous work by Middlemiss et al. [126] which yielded $\sigma_{ref} = 223.70 \pm 3.03$ppm, $m = -0.888 \pm 0.014$ with a mean absolute error (MAE) of 12.1 ppm. The chemical shift anisotropy and asymmetry are also computed, defined as $\sigma_{aniso} = \sigma_{zz} - \frac{1}{2}(\sigma_{xx} - \sigma_{yy})$ and $\eta_{CS} = \frac{(\sigma_{yy} - \sigma_{xx})}{(\sigma_{zz} - \sigma_{iso})}$, respectively. The quadrupole coupling constant for ^{17}O sites is obtained as $C_Q = eQV_{zz}/h$; and the asymmetry, as $\eta_Q = \frac{(V_{xx} - V_{yy})}{V_{zz}}$; where an ordering $|V_{zz}| \geq |V_{yy}| \geq |V_{xx}|$ of the principal components of the traceless electric field gradient tensor is assumed. The experimental value Q = -0.02558 barns has been used for the ^{17}O nuclear electric quadrupole moment.(Pyykkö [95]) All the chemical shift and quadrupolar NMR parameters of $Ba_2In_2O_5$ were averaged from the five $\cdots OctTetOctTet' \cdots$ and four $\cdots OctTetOctTet \cdots$ optimized configurations obtained using small perturbation as discussed above, with the full representation of NMR parameters for each structure given in the Appendix A.2. Unless otherwise specified, all the corresponding simulated ^{17}O NMR spectra were obtained by simulation of each individual O site with SIMPSON code by Bak et al. [131] which were then summed

together to result in the final spectra.

2.3 Results and Discussion

2.3.1 DFT Calculations (Structures and Energetics)

The DFT-based structural optimisation for $Ba_2In_2O_5$ proceeded from the two models with the $Ibm2$ and the $Ima2$ space groups proposed by Berastegui et al. [13] and Speakman et al. [12] and Fischer et al. [48], respectively. Note that although Speakman et al. [12] and Berastegui et al. [13] reject the $Ibm2$ structure in favour of an $Icmm$ (no. 74) solution, it is difficult to faithfully represent a lattice bearing fractional occupancies in the present theoretical approach, and so we regard the $Ibm2$ cell as the closest available structure consistent with the constraint to full site occupancies. This approach was also adopted by Mohn et al. [42] in their theoretical studies. The final optimized lattice constants, along with relevant bond lengths and angles of $Ibm2$ derived $\cdots OctTetOctTet' \cdots$ are compared with the ground state $Ibm2$ calculated structure of Mohn et al. [42], and the $Ima2$ Fischer et al. [48] and $Ibm2$ Speakman et al. [12] experimentally derived structures, in Table 2.1. The final optimised structure deviates markedly from that due to Fischer et al. [48], most notably in regard to the nature of the internal distortions of the In-O polyhedra away from their respective ideals. Specifically, the optimisation yields InO_6 octahedra wherein the In-O bond lengths fall in a 4-short and 2-long pattern, in agreement with the $Ibm2$ structure of Speakman et al. [12], Berastegui et al. [13], and Gregory and Weller [11] whereas the Fischer et al. [48] structure has a distortion in the opposite sense. Assuming that the disposition of and standard deviation in the In-O bond lengths constitutes a reasonable basis upon which to judge the agreement of the various structures, it is concluded that the present calculations are more supportive of the Speakman et al. [12] and Berastegui et al. [13] structure. We state again that further tightening of the optimization tolerances yields no appreciable change in the calculated structural parameters.

The $Icmm$ structure of Speakman et al. [12] and Berastegui et al. [13] suggests that we need to consider the possibility of residual disorder in the room temper-

ature structure. (Figure 2.3a) To explore this, we introduced deviations from the ground state, by randomly perturbing all atomic positions by as much as 0.1Å and structurally optimizing these structures with DFT, thereby generating 5 potential ground state structures that differ by only $0.2kJmol^{-1}$ in energy from the lowest energy structure discussed above, giving an information about the thermal atomic displacement. These structures are all based on the $\cdots OctTetOctTet' \cdots$ motif. We also investigated the first high energy state structure of Mohn et al. [42] again generating a series of structures (4) with slightly different atomic positions by applying the same random disorder in atomic positions. The first high energy state proposed by Mohn et al. [42] is a brownmillerite type of structure with stacked O3 vacancy channels, $\cdots OctTetOctTet \cdots$, as can be seen in Figure 2.1b. These series of calculations reveal that small but significant variations in, for example, In-O-In bond angles of 1-4°are possible within the difference between the formation energies ($5kJmol^{-1}$) of the ground state and the first high energy state structures noticeably (Table 2.1).

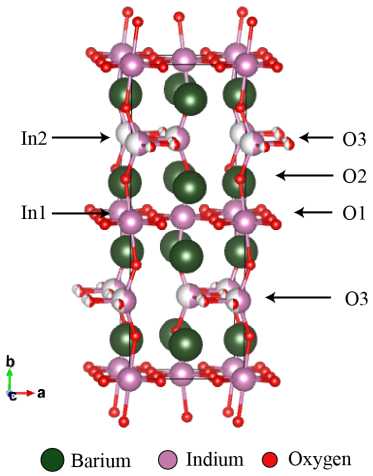

Figure 2.3: (a) *Icmm* space group structure proposed by Speakman et al. [12] and Berastegui et al. [13] with atomic disorder and partial site occupancy (seen as sector filling of atoms)

Table 2.1: Cell constants (Å, °), In-O bond distances (Å) and In-O-In bond angles (°) for O1, O2 and O3 environments obtained from optimizations of the initial perturbed P1 symmetry $Ba_8In_8O_{20}$ cells, both ground state, $\cdots OctTetOctTet' \cdots$, (5 structures) and the first high energy state, $\cdots OctTetOctTet \cdots$, (4 structures), and as compared with corresponding experimental and computational literature values. Means and standard deviations in the values are shown.

		Optimized-$Ba_2In_2O_5$ ground state present calculation ($P1$)	**Optimized-$Ba_2In_2O_5$ first high energy state present calculation ($P1$)**	**Computational Mohn et al. [42]**	**Experimental Fischer et al. [48] ($Ima2$)**	**Experimental Speakman et al. [12] ($Ibm2$)**
Environment	**Unit cell parameters** (Å, °)	a = 6.233, b = 16.905, c = 6.043 $\alpha = \beta = \gamma = 90.0$	a = 6.190, b = 17.072, c = 6.045 $\alpha = \beta = \gamma = 90.0$	a = 6.279, b = 16.841, c = 6.085, $\alpha = \beta = \gamma = 90$	a = 16.719, b = 6.083, c = 5.956, $\alpha = \beta = \gamma = 90$	a = 6.087, b = 16.784, c = 5.970, $\alpha = \beta = \gamma = 90$
In-O1-In	distances (Å)	2.174 (sd 0.000), 2.177 (sd 0.001)	2.160 (sd 0.000), 2.168 (sd 0.001)	2.188, 2.196	1.844, 2.421	2.127, 2.143
	angle (°)	172.2 (sd 0.0)	178.1 (sd 0.3)	-	173.1	173.1
In-O2-In	distances (Å)	2.064 (sd 0.000), 2.364 (sd 0.001)	2.068 (sd 0.001), 2.376 (sd 0.001)	2.096, 2.341	1.927, 2.412	2.012, 2.310
	angle (°)	147.4 (sd 0.1)	150.0 (sd 0.3)	-	149.7	154.6
In-O3-In	distances (Å)	2.111 (sd 0.000), 2.122 (sd 0.000)	2.116 (sd 0.000), 2.125 (sd 0.001)	2.137, 2.144	2.184, 2.369	2.091, 2.109
	angle (°)	127.6 (sd 0.1)	124.6 (sd 0.2)	-	115.8	129.3

2.3.2 Diffraction and NMR

The experimental X-ray powder diffraction patterns obtained here for both $Ba_2In_2O_5$ (Jayaraman et al. [3], Gregory and Weller [11], Speakman et al. [12]) and ^{17}O enriched $Ba_2In_2O_5$ prepared are consistent with previous reports by Jayaraman et al. [3] and Speakman et al. [12] (Figure 2.2) and indicate that at room temperature the structures are orthorhombic. The patterns match structures modelled in either space groups *Ibm*2 (Jayaraman et al. [3], Gregory and Weller [11], Speakman et al. [12]) or *Icmm* (Speakman et al. [12], Berastegui et al. [13]), both space groups yielding very similar diffraction patterns.

The one-dimensional ^{17}O MAS NMR spectrum of ^{17}O enriched $Ba_2In_2O_5$ obtained at 21.1 T shows two similarly broadened and well-resolved resonances centered at 179 and 138 ppm with an intensity ratio of approximately 3:2. Appreciable broadening of the resonances occurs as the field strength is decreased from 21.1 T to 9.4 T, indicative of the presence of significant second order quadrupolar broadening. (Figure 2.4a) A large quadrupolar coupling constant is to be expected, given the asymmetry inherent to In-O-In, O environments and to concomitantly large electric field gradients. The broad lines are also an indication that there is little O motion at room temperature to average out anisotropic effects such as the quadrupolar coupling.

The variable temperature ^{17}O NMR study seen in Figure 2.4b shows two broad peaks overlapped with 3 kHz spinning side bands. With the information about two major sites from the better resolved room temperature spectra (Figure 2.4a) and our DFT calculations (see NMR GIPAW calculations section) we can analyse the variable temperature data in Figure 2.4b. Following the intensity change of respectively high and low frequency shifts at around 179 ppm and 138 ppm with increasing temperature, we can clearly observe that both peaks loose intensity. In addition, the intensity of the 179 ppm peak decreases more rapidly than the 138 ppm peak reaching almost equal intensity at around 450 °C, with increased temperature. This can be ascribed to an exchange of oxygen sites or a structural change. Our DFT calculations help identify these possibilities as described further in the following section, and we propose an increased concentration of the first high energy state structure (Figure 2.1b) co-existing with the ground state

structure (Figure 2.1a) with increasing temperature.

As discussed above, structural refinements of both space groups *Ibm*2 or *Icmm* give rise to three O sites O1, O2, O3 (Figure 2.1) with a 2:2:1 ratio. However, only two O chemical-environments are detected in the 1D ^{17}O NMR spectra. Thus, ^{17}O 3QMAS experiments (Amoureux et al. [52], Frydman and Harwood [75], Medek et al. [76]) were also performed in an effort to try to resolve any additional ^{17}O sites in $Ba_2In_2O_5$ that may have been missed. However, again only two ^{17}O sites in an approximately 3:2 ratio are observed (Figure 2.4a). Simulations of the ^{17}O 1D and MQMAS NMR spectra yield a quadrupole coupling constant (C_Q) value of 5 MHz for the O environment associated with the high frequency signal at an isotropic chemical shift $\delta_{iso} = 179 \pm 4$ ppm and a slightly larger value of 5.8 MHz for the low frequency signal at $\delta_{iso} = 138 \pm 4$ ppm on, Figure 2.4 and 2.6. We note that the high frequency signal shows a broadening along the +1 (positive slope, diagonal) direction of the MQMAS spectrum corresponding to a small distribution of chemical shifts, suggesting that more than one site is buried under this resonance. The isotropic shifts obtained from the field dependence of the peak positions in the 1D spectra, (Figure 2.5; Table 2.2), differ slightly from those obtained by simulation of the 1D and MQMAS data, suggesting that the data cannot be fitted by a single set of NMR parameters for each resonance.

The ^{17}O MAS NMR spectra of the $Ba_2In_2O_5$ presented above are obtained when $Ba_2In_2O_5$ was dried at 1000 °C prior to ^{17}O enrichment (see the Materials and Methods section). The resonance at 220 ppm observed previously by Adler et al. [1] (note that no explicit pre-drying step prior to ^{17}O enrichment was mentioned by these authors) appears only very weakly in the 8.5 T spectrum in Figure 2.4a, and its presence depends strongly on the $\frac{\pi}{2}$ pulse length used to acquire the spectra It cannot reasonably be ascribed to a BaO impurity, as might be present if the sintering step of the $Ba_2In_2O_5$ synthesis was not complete, since this gives rise to a much higher shift of 629 ppm.(Smith and van Eck [15]) The most likely assignment of this resonance is that it is due to surface water. This is also consistent with the nutation frequency behaviour and the absence of second-order quadrupolar broadening (Bastow et al. [132]) observed previously. In fact, the ^{17}O MAS NMR spectrum of ^{17}O enriched $Ba_2In_2O_4(OH)_2$ obtained using a pulse

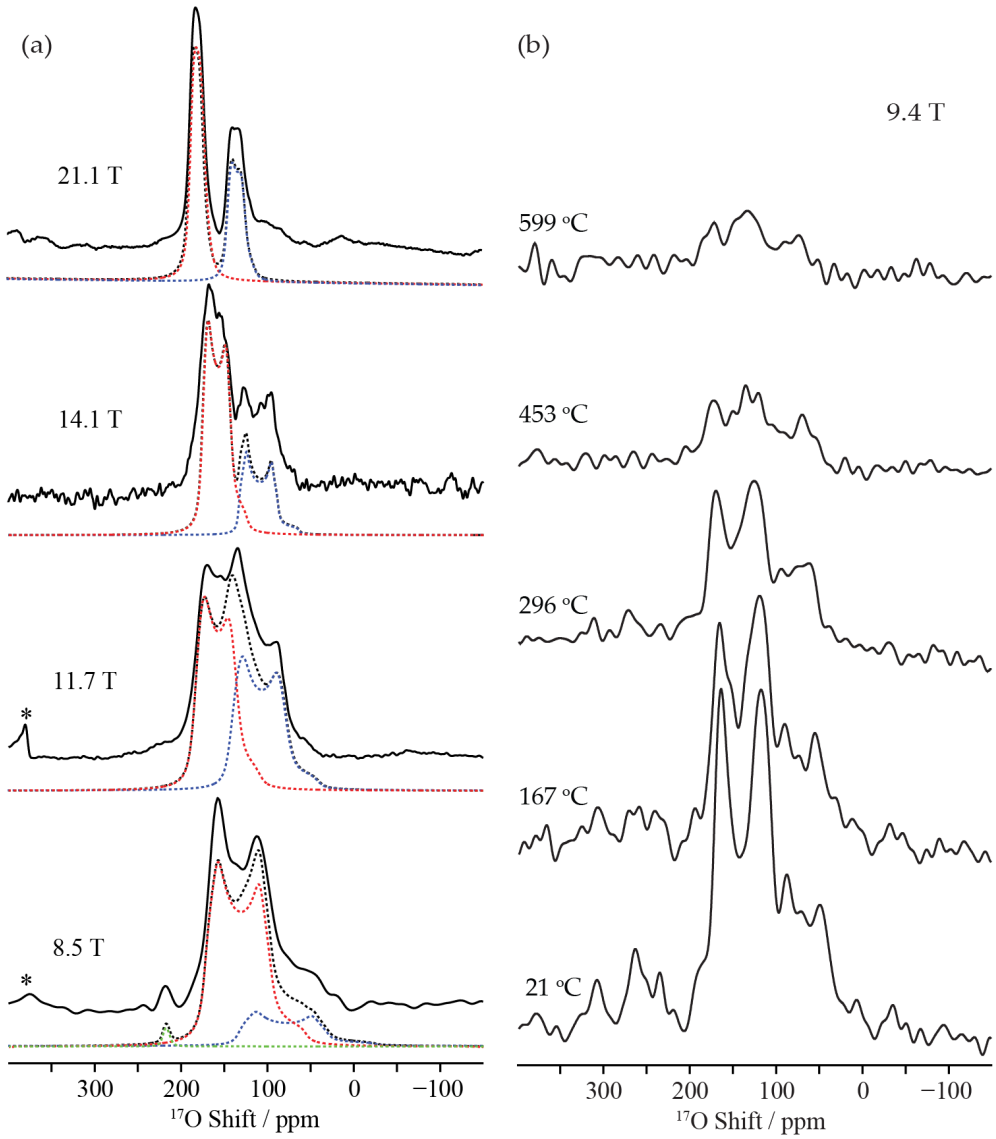

Figure 2.4: (a) ^{17}O MAS NMR spectra of ^{17}O enriched $Ba_2In_2O_5$ as a function of magnetic field strength. Experimental spectra are shown in full lines, and best-fit simulations in black dashed lines. The simulations using site components are shown with dashed lines, in red (site A (O1 and O3)) and blue (site B (O2)) obtained by the experimental parameters given in the Table 2.2. The green dashed line represents an O site, which might appear due to partial hydration of the sample from air. The asterisks denote the O signal from the ZrO_2 rotor.(Turner et al. [14]) (b) ^{17}O MAS NMR spectra of ^{17}O enriched $Ba_2In_2O_5$ as a function of temperature with 3KHz spinning speed and 9.4T magnetic field.

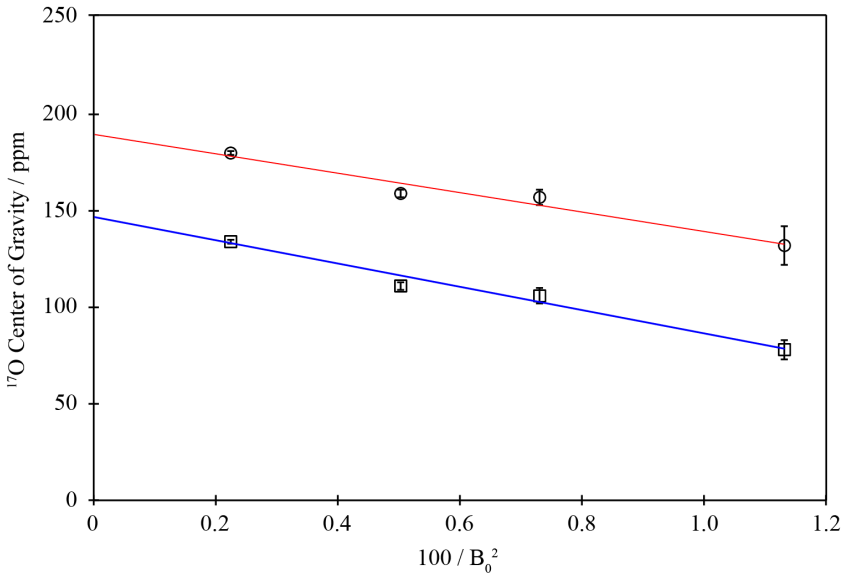

Figure 2.5: Variable B_0 field dependence of the ^{17}O MAS NMR shift of the centre of gravity of the two ^{17}O signal in $Ba_2In_2O_5$. The straight lines denote least squares fits, yielding isotropic chemical shifts of 189(8) and 146(8) ppm for the high and low shift ^{17}O sites, respectively.

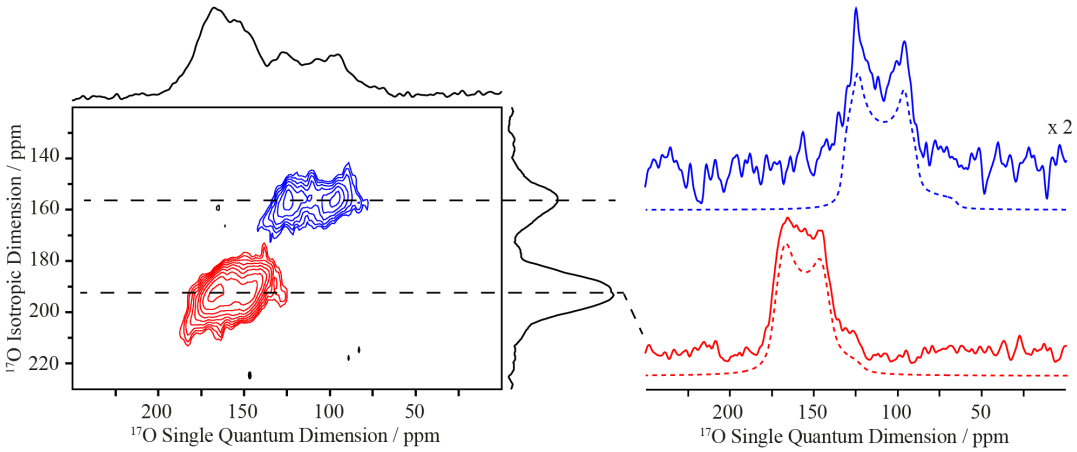

Figure 2.6: Two-dimensional ^{17}O 3QMAS spectrum of ^{17}O enriched $Ba_2In_2O_5$ obtained at 14.1 T. Right: experimental cross sections (full lines) obtained at δ_1 = 156 (blue) and 192 (red) ppm along with best-fit simulations (dashed lines) using the experimental parameters given in Table 2.2.

length similar to the one measured by nutation on a water reference, reveals an intense and sharp resonance at 220 ppm (Figure 2.7)

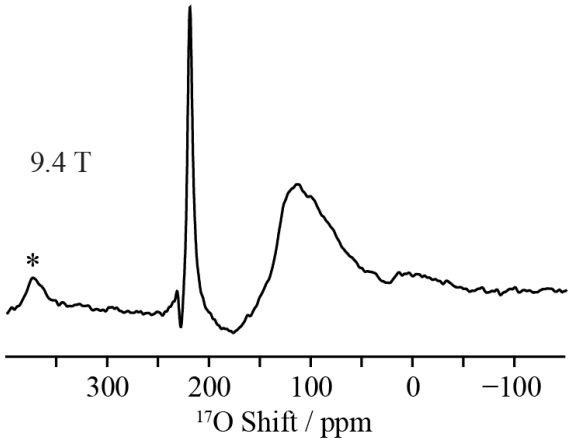

Figure 2.7: ^{17}O MAS NMR spectrum of ^{17}O enriched $Ba_2In_2O_4(OH)_2$ at 9.4 T obtained using a 3 μs pulse length corresponding to $\frac{\pi}{2}$ pulse at a radio frequency field amplitude of 80 kHz as measurement in liquid water. The lineshape distortion of the broad site at $\sim$ 100 ppm arise from the long pulse length used in this experiment.(Smith and van Eck [15]) The asterisks denote the oxygen signal from the ZrO_2 rotor. (Turner et al. [14])

2.3.3 NMR GIPAW Calculations

It has been shown previously that differences in the chemical shifts and quadrupole parameters of ^{17}O NMR in ABO_3 metal-oxides depend strongly on the B site cation species, to the B-O bond distances, and the M-O-M bond angles. (Ashbrook and Smith [123], Bastow et al. [132], Palumbo et al. [133]) It is not obvious, however, how the observed resonances can be definitely assigned and rationalized making use of these trends. Recent work on doped perovskites and other oxides, (Blanc et al. [119], Middlemiss et al. [126], Reader et al. [128]) demonstrate that the ^{17}O GIPAW calculations are very reliable and could thus be used here. The optimised structure obtained for $Ba_2In_2O_5$ is used for the single point NMR calculation, subject to increased basis set cut-off energy as described above. The computed ^{17}O chemical shifts, anisotropies, asymmetries and quadrupole NMR

Table 2.2: Experimental and calculated ^{17}O isotropic chemical shift, δ_{iso} (ppm); quadrupole coupling constant, C_Q (MHz); and quadrupole asymmetry η_Q for $Ba_2In_2O_5$. Standard deviations are also given for the calculated parameters; deviations of both quadrupolar parameters are less than 0.01.

Structure	**Environment**	δ_1 **(ppm)**[a]	δ_{iso}	C_Q **(MHz)**	η_Q	**N**[b]
			Experimental[c]			
$Ba_2In_2O_5$	Site A (O1+O3)	192	179(4)/189(8)[d]	5.0(2)	0.2(1)	0.6
	Site B (O2)	156	138(4)/146(8)[d]	5.8(2)	0.2(1)	0.4
			Calculated[e]			
$\cdots OctTetOctTet' \cdots$	O1	-	181.6 (sd 4.2)	-5.74	0.05	0.4
	O2	-	158.2 (sd 3.1)	-6.27	0.15	0.4
	O3	-	195.4 (sd 2.6)	-4.70	0.89	0.2
$\cdots OctTetOctTet \cdots$	O1-1	-	203.6 (sd 1.7)	-5.77	0.02	0.2
	O1-2	-	152.1 (sd 1.2)	-5.73	0.09	0.2
	O2	-	158.2 (sd 2.7)	-6.19	0.14	0.4
	O3	-	198.4 (sd 3.2)	-4.57	0.98	0.2

[a]Slices were extracted from the isotropic dimension of the MQMAS spectrum at isotropic shifts of δ_1 (ppm). [b] Molar fraction of the site in the structure specified. [c] Obtained from the 3QMAS experiment and 1D spectra. [d] The first listed δ_{iso} value is obtained by a joint fit of the 1D and MQMAS spectra. The second value was obtained by analysing the field dependence of the 1D spectra. [e] Obtained from the averaged DFT calculated NMR parameters of the five perturbed and structurally re-optimized ground state structures ($\cdots OctTetOctTet' \cdots$) and the four perturbed and structurally re-optimized first high energy state structures ($\cdots OctTetOctTet \cdots$) ($E_{rel}$= +5.0 kJ/mol).

parameters are presented in the SI. The chemical shifts (δ_{iso}) were obtained using the fitted reference parameters discussed above cover a wide range of values (Figure 2.9a). Averaging over the shifts obtained for the ground state structure and the 5 perturbed structures (that differ only by $0.2 kJmol^{-1}$ in energy from the lowest energy structure) for each sublattice leads to values of 181.6ppm, 158.2ppm and 195.4ppm in a 2:2:1 ratio for the O1, O2 and O3 sites, respectively (in the $\cdots OctTetOctTet' \cdots$ configuration), respectively. The range in O2 values, amounting to approximately 5.5 ppm, is larger than those computed for the other two sites. This relates directly to the broader range of In-O bond lengths experienced by the O2 sites (see Table 2.1).

Calculations reveal a small In-O2-In bond angle together with asymmetric In-O2 bond lengths, that in return result in a very different chemical environment for the O2 oxygen sites as opposed to the O1 and the O3 for the $\cdots OctTetOctTet' \cdots$ configuration in Table 2.1. The computed oxygen Mulliken charges have also been examined, so as to discern any potential correlation with σ-values, but it is found that the charges vary in only a narrow range from -0.94 to -0.96 $|e|$

across the ten O sites. So, we instead turn to examine the distribution of In-O bond lengths and Mulliken overlap populations, anticipating that each O site forms two close coordinations with neighboring In cations. We find that the comparatively large shieldings of the O2 nuclei are associated with a strongly asymmetric bonding environment, with mean bond lengths of 2.066 and 2.368 Åleading to mean overlap populations of 0.50 and 0.26 $|e|$, respectively. For comparison, the mean distances and overlap populations at O1 sites are 2.170 and 2.177 Å, and 0.34 and 0.34 $|e|$, respectively; and at O3 sites, 2.116 and 2.121 Å, and 0.39 and 0.37 $|e|$, respectively. On this basis, it is suggested that the high shieldings of the O2 sites may be due to the heightened polarization of these anions. In support of this suggestion, we note the study by Bastow et al. [132] of a wide range of ABO_3 and A_2BO_3 phases, which found a strong correlation between the degree of anion polarization and the measured chemical shift. ^{115}In and $^{135/137}$Ba NMR parameters are also calculated and presented in Appendix A.2.

The ^{17}O GIPAW calculations support the conclusion that the experimental ^{17}O resonance at δ_{iso} of 179 ppm (Table 2.2) arises due to the combination of all the O1 and O3 sites while the experimental site seen at $\delta_{iso} = 138$ ppm is assigned to the O2 site (Figures 2.4a and 2.6). However, it is clear that the experimental splitting $\Delta\delta = 41$ ppm is underestimated by the calculations (the splitting being 30 ppm, the mean absolute error in calculated ^{17}O shift calculation due to σ_{ref} being 12 ppm). (Middlemiss et al. [126]) Figure 2.9b plots the comparison between the experimental and calculated ^{17}O spectra at both 14.1 and 21.1 T (Figure 2.8 for the ^{17}O spectra as a function of magnetic field strengths, 8.5, 11.7, 14.1 and 21.1T) where the underestimated separation of peaks by the calculations is clearly visible. The reasons for this apparent discrepancy remain the subject of ongoing work.

The present calculations provide relatively similar C_Q-values for all three sites (Table 2.2), while the EFG asymmetry parameters, η_Q, vary more markedly, reaching a maximum for the tetrahedral sublattice. The difference in the mean computed O1 + O3 and O2 C_Q-values, at approximately 0.88 MHz, is in very good agreement with the 0.8 MHz value obtained from the fits to the experimental spectrum discussed above (Table 2.2). In summary, the present first principles

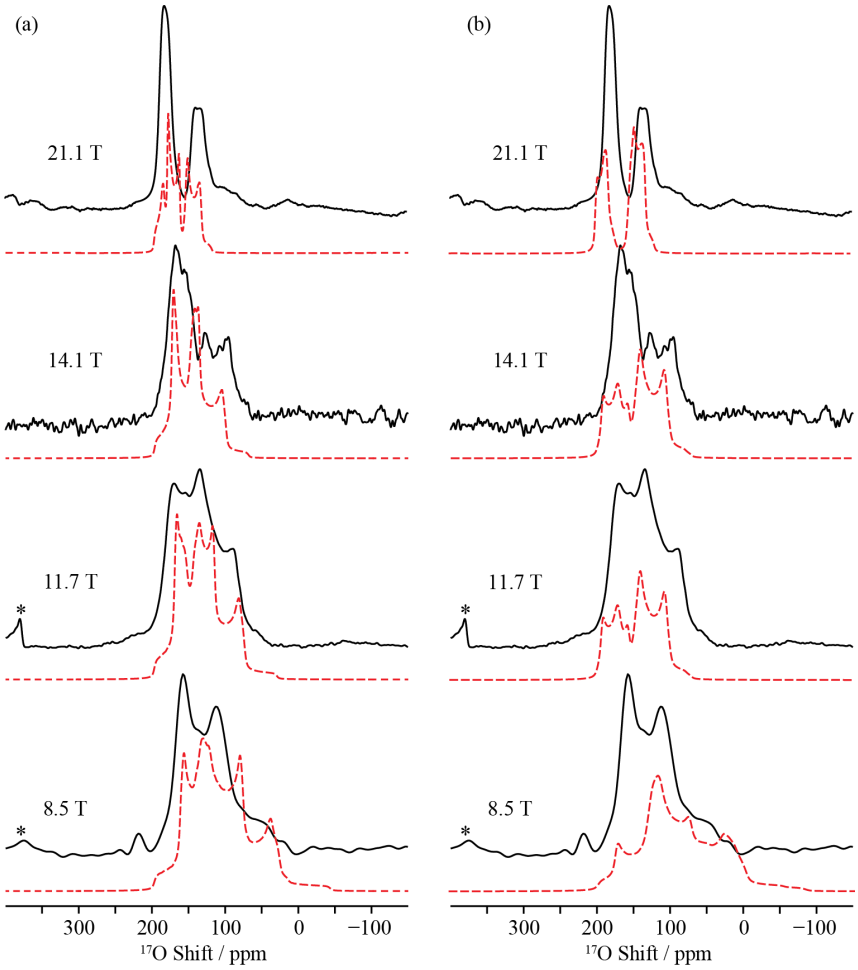

Figure 2.8: Comparison of the experimental (full lines) ^{17}O MAS NMR spectra of $Ba_2In_2O_5$ and the simulation (red dashed lines) of the GIPAW calculated ^{17}O NMR spectra of computed $Ba_2In_2O_5$ in (a) the ground state $\cdots OctTetOctTet' \cdots$ staggered oxygen vacancy configuration and (b) the first high energy state $\cdots OctTetOctTet \cdots$ stacked oxygen vacancy configuration as a function of magnetic field strengths. The asterisks denote the oxygen signal from the ZrO_2 rotor. (Turner et al. [14])

calculations allow clear assignment of the experimental NMR data of $Ba_2In_2O_5$, although some discrepancies remain. It is likely that some of these discrepancies may be due to O dynamics not taken into account in the calculations and additional O disorder. No evidence for any sites with a small quadrupole coupling constant emerge from these calculations, confirming that narrow resonance at 220 ppm is unlikely to arise from an O3 site in the dry material.

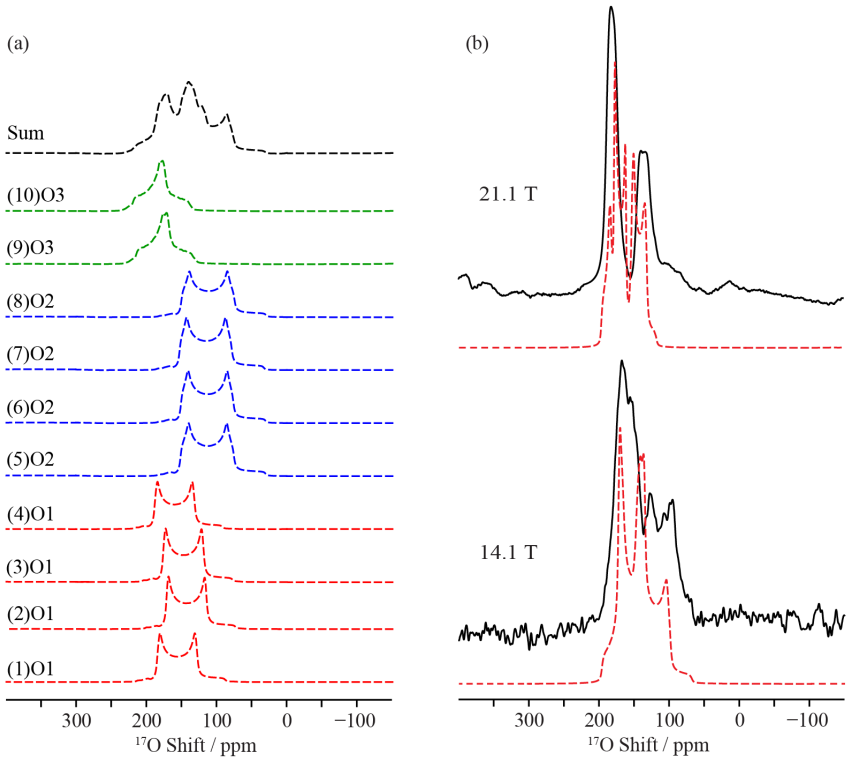

Figure 2.9: (a) Full black line: experimental ^{17}O NMR spectra of $Ba_2In_2O_5$. Dashed black line: simulation of the GIPAW calculated ^{17}O NMR spectra of the sum (scaled down by a factor 10) of all O sites of one of the five optimized $Ba_2In_2O_5$ structures having the $\cdots OctTetOctTet' \cdots$, staggered O vacancy configuration. Color dashed lines: simulation of the GIPAW calculated ^{17}O NMR spectra of the individual O sites (color grouped and noted for O1, O2 and O3 sublattices) of the same structure. All the spectra were recorded/simulated at 14.1 T. (b) Comparison of the experimental ^{17}O NMR spectra of $Ba_2In_2O_5$ (black lines) and the sum of the simulation of the GIPAW calculated ^{17}O NMR spectra (dashed red lines) of all five $Ba_2In_2O_5$ ground state configurations at two magnetic field strengths.

In order to explore whether the first high energy state $\cdots OctTetOctTet \cdots$ structures contribute to the experimental NMR spectrum we note that the difference in formation energies of these two structures is only $5kJmol^{-1}$ (equivalent to 600 K). Therefore it is possible that an high energy state structure exists or could be trapped in at room temperature. The calculated spectra of the $\cdots OctTetOctTet \cdots$ and individual oxygen sites can be seen in Figure 2.10. Interestingly, the O1 sites in this structure split into groups, one group having similar chemical shifts (205 ppm) to the ground state structures while the second being similar to those observed for O2 (150 ppm). Thus it is possible that there is a contribution from the high energy state structure to the experimentally observed spectrum, which is difficult to resolve. However it cannot be significant because simulations of the high energy state structure predict an intensity ratio for the high and low frequency resonances of 2:3, which is not consistent with the experimentally observed intensity ratio. Interestingly, these results suggest that disordering of the O3 sublattice as occurs at higher temperatures will result in noticeable changes in the other oxygen resonances as seen in Figure 2.4b where relative intensity of the high frequency shift is decreasing with increasing temperature.

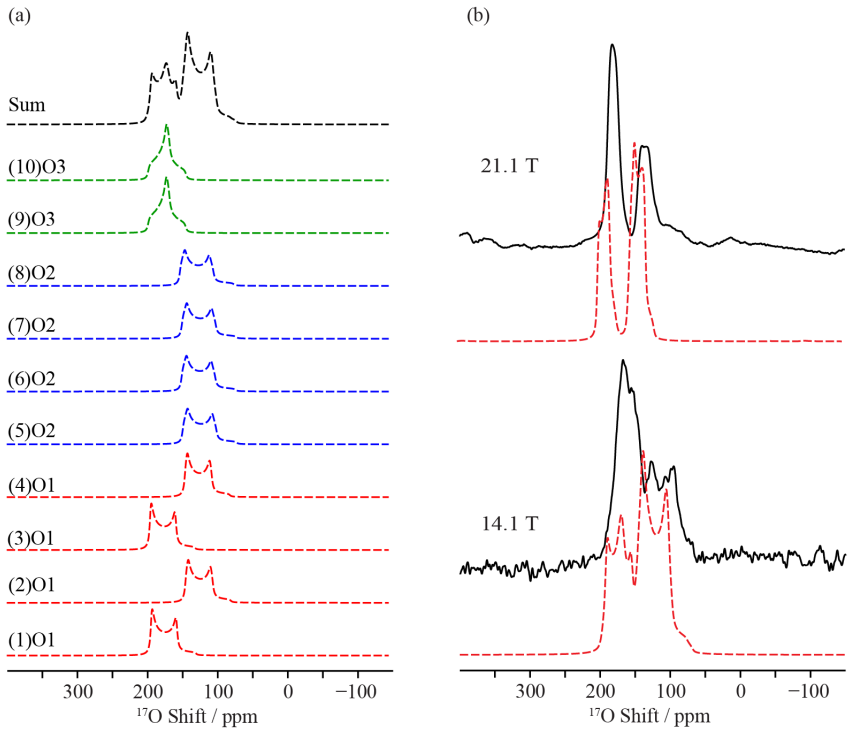

Figure 2.10: (a) Full black line: experimental ^{17}O NMR spectra of the first high energy state of the $Ba_2In_2O_5$. Dashed black line: simulation of the GIPAW calculated ^{17}O NMR spectra of the sum (scaled down by a factor 10) of all O sites of one of the four optimized $Ba_2In_2O_5$ structures having the $\cdots OctTetOctTet\cdots$, stacked O vacancy configuration. Color dashed lines: simulation of the GIPAW calculated ^{17}O NMR spectra of the individual O sites (color grouped and noted for O1, O2 and O3 sublattices) of the same structure. All the spectra were recorded/simulated at 14.1 T. (b) Comparison of the experimental ^{17}O NMR spectra of $Ba_2In_2O_5$ (black lines) and the sum of the simulation of the GIPAW calculated ^{17}O NMR spectra (dashed red lines) of all four $Ba_2In_2O_5$ first high energy state configurations at two magnetic field strengths.

2.4 Conclusion

In summary, we have performed a comprehensive structural analysis of the brownmillerite $Ba_2In_2O_5$ structure using multinuclear solid state NMR spectroscopy in combination with solid-state DFT calculations. An analysis of its corresponding hydrated form, $Ba_2In_2O_4(OH)_2$, will be presented in a subsequent chapter 4. Two distinct O environments in a 3:2 ratio were observed by ^{17}O MAS NMR in ^{17}O enriched $Ba_2In_2O_5$ and were assigned to the crystallographic O1+O3 and O2 sites. The more intense resonance seen at 179 ppm (at 21.1 T) is attributed to the combination of the O1 and O3 sublattices, while the weaker resonance at 138 ppm comprises the O2 sublattice alone. The assignment is based on GIPAW NMR calculations on both the ground state $\cdots OctTetOctTet' \cdots$ and high energy state $\cdots OctTetOctTet \cdots$ structures, which indicate that O1 and O3 sites have similar chemical shifts and quadrupolar couplings, preventing their separate resolution even at a very high magnetic field strength of 21.1 T. Notably the bridging O1 and O2 sites have similar calculated asymmetry parameters 0.05 and 0.15, the O1 value reflecting the more linear In-O-In bonding arrangement. In contrast, the asymmetry parameter for the bent (127.6°) In-O-In, O3 site is very different (0.9). The MQMAS data reveals a small distribution of environments consistent with some disorder in this material and making the separation of the O3 and O1 sites more difficult. An analysis of the first excited $\cdots OctTetOctTet \cdots$ structure reveals an intensity ratio for the high and low frequency shifts that is not consistent with that observed experimentally, suggesting that it is not present in significant concentrations.

This new assignment is in contrast with the previous proposal that the two dominant but very different ^{17}O resonances arose due to the presence of InO_4 tetrahedra and InO_6 octahedra.(Adler et al. [1]) The sharp resonance at 220 ppm previously attributed to the O3 site by Adler et al. [1] is here shown to appear only upon exposure of the sample to moisture and is therefore tentatively re-assigned as originating from hydration surface water; structural models investigated here do not reproduce the 220ppm shift and further study is required to address this point.

Chapter 3

Cluster expansion and Monte Carlo simulation of the Ga doped $Ba_2In_2O_5$ fast anionic conductor

3.1 Introduction

Highly defective $Ba_2In_2O_5$ perovskite and brownmillerite structures (Figure 3.1) have been proposed as a promising class of electrolyte materials due to their large inherent oxygen vacancy concentrations, doping flexibility, and high oxygen conductivities, particularly at higher temperatures.(Goodenough et al. [7]) Further optimization of such classes of materials to create electrolytes with even higher conductivities is inhibited by a poor understanding of the fundamental mechanisms by which the dopants influence oxygen transport. In particular, a more detailed insight is required into the mechanisms governing the coupling between dopants and vacancies, the mutual interactions of the latter and the factors that control ordering to form the ordered brownmillerite structure. To elucidate some of these phenomena, we have chosen to investigate the pristine and the Ga-substituted phases of barium indium oxide. Isovalent substitution of Ga on the In sublattice results in a $Ba_2(In_{1-x}Ga_x)_2O_5$ stoichiometry allowing the effect of cation substitution to be investigated while keeping the oxygen concentration (and thus vacancy concentration) constant.

The low temperature orthorhombic form of $Ba_2In_2O_5$ adopts the brownmillerite structure as shown in Figure 3.1.(Speakman et al. [12], Fischer et al. [48]) A previous study of the Ga-substituted phases revealed an orthorhombic structure at ambient temperature for low doping levels, and a cubic structure for $x \geq 0.25$.(Yao et al. [2]) $Ba_2In_2O_5$ has two phase transformations, a first-order transformation at 950°C and a second-order transformation at 1040°C.(Speakman et al. [12]) The high oxygen ion conductivity, crucial for its application as an SOFC electrolyte occurs only above the 950°C first-order orthorhombic-tetragonal phase transformation.(Goodenough et al. [7]) The first-order transformation is regarded as undesirable, both because it requires a high temperature for oxygen transport and because it can lead to cracking and failure of the electrolyte during operation. According to a study by Yao et al. [2], both phase transformations have been shown to disappear for sufficiently high levels of Ga-doping, which can stabilize the high-temperature disordered phase. While the effect of doping on the phase transformations is known (Yao et al. [2], Rolle et al. [49]), less is understood about the local environments experienced by dopants, the phase energetics, and the process of oxygen ion conduction in the presence of the dopants.

Approach here is in the same spirit as the work on first principles using thermokinetic modelling with full configurational counting for the $Ba_2In_2O_5$ system by Mohn et al. [42], Stølen et al. [134], Mohn et al. [135], although we make use of an explicit lattice model to study the thermodynamics. Previous work by Lee and Morgan [136] demonstrated that a first principles based thermodynamic model capturing the key phase transitions in $Ba_2In_2O_5$ can be constructed, including the first- and second-order character of these transitions. The model was then applied to understand the nature of the disordering process and the oxygen sites available for transport in the $Ba_2In_2O_5$ system.

Here we undertake theoretical calculations of phase thermodynamics and local structure via variable temperature Monte Carlo (MC) simulations based upon a cluster expansion (CE) approach. The effective cluster interactions are parameterized by first principles density functional (DFT) calculations. Complementary to the theory work, X-ray diffraction and high-energy X-ray pair distribution function (PDF) analyses of both $Ba_2In_2O_5$ and $Ba_2(In_{1-x}Ga_x)_2O_5$ are performed. The specific issues we aim to address include the nature of the local structure

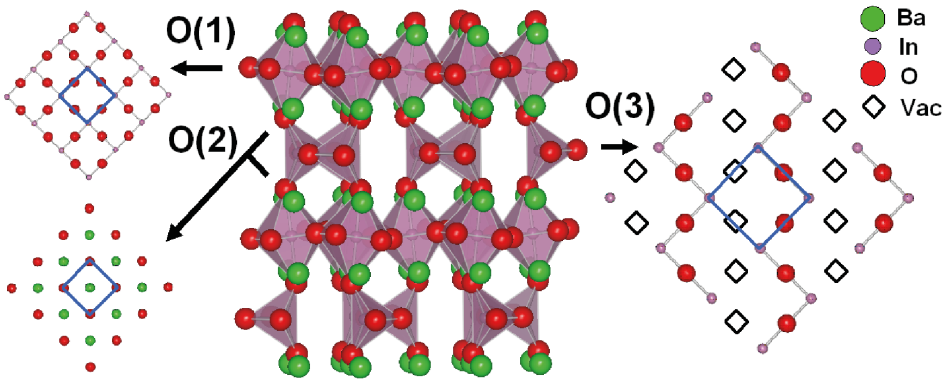

Figure 3.1: The orthorhombic Ibm2 structure of $Ba_2In_2O_5$ and oxygen layers of the orthorhombic phase where squares indicate oxygen vacancies with respect to a perovskite structure, red circles oxygen, green circles barium and purple circles indium atoms.

on either side of the orthorhombic-tetragonal and tetragonal-cubic transitions in $Ba_2In_2O_5$, and the variations caused by Ga-doping.

Monte Carlo simulations can in principle yield detailed insight into the physical and chemical properties of both undoped and doped systems at varying temperatures. The properties often sought in these types of calculations include phase stabilities and state of atomic order. However, MC simulations based directly upon first principle energies are generally intractable, given the large supercells typically required. The problem is instead addressed within a CE approach. This method uses a configurational Hamiltonian parameterized on the basis of DFT calculations that may subsequently be efficiently applied to calculate the energies of configurations of essentially arbitrary size.(Sanchez et al. [98], de Fontaine [99], Zunger [100], Kutner et al. [101], van de Walle and Asta [103]) The CE approach has been shown to work particularly well in alloy systems lacking strong orientational dependence of the intersite interactions. Here, however, the CE method is applied to an ionic oxide with significant directionality of bonding, with the effect that the CE must be parameterized with reference to significantly more structural configurations than for the average metallic alloy. Longer-range interactions also feature significantly here, essentially due to the weak screening common to all insulating oxides.

The next section describes the theoretical and experimental methods used, and subsequent sections, the computed results and experimental findings. An overview of both sets of results and consequences for the application of the doped materials as SOFC electrolytes is presented in the conclusions.

3.2 Methods

3.2.1 Theoretical

First principles DFT calculations within the projector augmented wave (PAW) method (Blöchl [137], Kresse and Joubert [138]) were performed using the Vienna ab-initio simulation package (VASP) (Kresse and Furthmüller [139]). Electron exchange and correlation were treated in the generalized gradient approximation parameterized by Perdew et al. [85] A plane wave cut-off energy of 500 eV was used for all calculations. The Brillouin zone was sampled using a Monkhorst-Pack (Monkhorst and Pack [88]) k-point grid of dimensions $4\times4\times4$ along the respective reciprocal space cell axes of the $Ba_2In_2O_5$ primitive cell, the k-point density being kept as constant as possible thereafter for the various cells used. The energy convergence for the $Ba_2In_2O_5$ primitive cell with respect to k-point density was better than 1 meV/atom. Inorganic crystal structure database (ICSD)(Bergerhoff and Brown [140]) was used for the triple phase diagram end-member and known stable structures, removing their symmetries for the DFT calculations. A total of 81 $Ba_2In_2O_5$ and 24 $Ba_2(In_{1-x}Ga_x)_2O_5$ configurations were used to fit the CE, each structure representing a distinct arrangement of O vacancies preserving the vacancy/oxygen ratio of $\frac{1}{6}$ appropriate for the $Ba_2In_2O_5$ and isovalently-doped $Ba_2(In_{1-x}Ga_x)_2O_5$ phases. (Appendix A.1 and A.3) These structures are generated by randomly distributing In, Ga, O and Vac species over an idealized perovskite lattice with increasing supercell size (up to $4 \times 2 \times 2$ in this work), eliminating symmetrically equivalent structures and implementing an iterative process with a goodness fit criterion. The DFT derived energies are iteratively compared to the CE generated energies until the goodness of fit (making a concave line with number of structures, hence having a minima) is reached as described by van de Walle and Ceder [63], van de Walle and Asta [103], Newman and Barkema [141].

Namely, the DFT derived energies are compared for each generated structure with the energy derived by using that of a minimum number of pairs, triplets, etc. clusters from the CE, increasingly larger numbers of clusters being added until the goodness of fit of 25.2 meV/site for the Ga-substituted systems and 15.9 meV/site for the pure In systems was achieved. However, the code used did not produce a sufficiently large number of Ga doped structures to capture the essential structural motifs (only 3 that do not have 1/6 Vac to O ratio) hence we generated Ga doped structures manually from $Ba_2In_2O_5$ structures by substituting In with Ga in desired concentrations sampling all possible GaO_m coordinations (m between 2 and 6) and also sampling Ga pairing effects by using small and large supercells, ranging from $2 \times 2 \times 1$ to $4 \times 2 \times 2$ supercells of a perovskite type unit cell. These $Ba_2(In_{1-x}Ga_x)_2O_5$ phases are at $x = 0.125$, 0.166, 0.25, 0.33 and 0.5.

A cluster expansion approach is adopted here for the efficient calculation of configurational energies. The DFT total energies of a series of model configurations are expanded in terms of a series of site clusters (point, pairs and triplets), each weighted by an appropriate multiplicity and an effective cluster interaction (ECI), the latter parametrized by fitting to the full set of DFT model energies. First, for $Ba_2In_2O_5$, the DFT energies for O/vacancy configurations were fit with 12 effective cluster interactions (ECIs), yielding a cross validation (CV) score of 15.9 meV/site. Meanwhile a multicomponent (two sublattices, four species) fit for $Ba_2(In_{1-x}Ga_x)_2O_5$ yielded 23 ECIs with a corresponding CV score of 25.2 meV/site. Metropolis algorithm MC simulations using the respective CEs were performed within an $8 \times 8 \times 8$ supercell of the perovskite unit cell, save for $Ba_2(In_{1-x}Ga_x)_2O_5$ at $x = 0.166$ where, due to Ga concentration constraints, an $8 \times 8 \times 6$ supercell was used. The starting configuration for all MC simulations was the brownmillerite type structure, which was generated as the ground state structure during the CE.

As will be discussed in section 3.3.2, cation kinetics is such that many experiments effectively study a material with a kinetically frozen disordered Ga/In arrangement. In order to model a frozen cation structure a mean-field effective cation is used on the Ga/In sublattice and a mean-field MC simulation is performed. The Mean-field MC required a transformation of multicomponent CE

ECIs, which include explicit contributions from Ga/In configurations, into mean-field ECIs that only consider effective interactions on the O sublattice. These mean-field ECIs were for just O-O interactions and were obtained by projecting the full CE Hamiltonian onto an O sublattice CE. The projection is performed by summing over all the Ga/In degrees of freedom as described by (Sanchez et al. [98]). In site interaction (In-In, In-O, In-O-O) energies were thereby distributed into corresponding reference, single O site or O pairs energies.

The CE fitting and MC simulations were performed using the ATAT code developed by van de Walle and Ceder [63], van de Walle and Asta [103], Newman and Barkema [141]. Structural visualization was performed with the VESTA code of Momma and Izumi [142]. Symmetry analysis of the MC derived $x = 0.25$ $Ba_2(In_{1-x}Ga_x)_2O_5$ ground state structure was investigated with the FINDSYM web based code of Stokes and Hatch [143].

3.2.2 Experimental

$Ba_2In_2O_5$ and $Ba_2(In_{1-x}Ga_x)_2O_5$ samples were synthesized with a solid state route, wherein stoichiometric amounts of $BaCO_3$, In_2O_3 and Ga_2O_3 were ball-milled, pellet pressed and calcined at 1100°C for 12h, re-ground and finally sintered at 1300°C for 12h. Two different cooling schemes were followed during synthesis: (I) slow cooled, where the alumina crucibles containing the pellets were extracted from the furnace at 1300°C and then placed on an alumina insulator, and (II) quenched, where the pellets were placed directly on an iron block straight after removal from the furnace at high temperature. The cooling step for both the slow cooled and quenched samples was performed inside a desiccator, in order to prevent the inclusion of humidity, which has been shown by Fischer et al. [48] to occur at lower temperatures. In order to investigate ordering at intermediate temperatures, x=0.25 $Ba_2(In_{1-x}Ga_x)_2O_5$ was annealed at 800°C (1073 K) for three weeks, the sample being kept in a closed quartz tube with $^{17}O_2$ gas and was then cooled with a rate of 5 °C/min. This temperature profile also provides information about the long-term stability of $Ba_2(In_{1-x}Ga_x)_2O_5$ under fuel cell working conditions.

X-ray powder diffraction data were acquired with a Bruker D8-Focus instru-

ment with a copper K_α source. Rietveld refinements were done with the GSAS program (Larson and Von Dreele [144]) and a powder diffraction database search and structural match was accomplished with the MDI Jade© program.

Total scattering (Bragg and diffuse scattering) data for pair distribution function (PDF) analysis were acquired at beam line 11-ID-C of the advanced photon source (APS) at Argonne National Laboratory, IL. A wavelength of 0.107480 nm (115 KeV) was used, and the sample was held 300 nm away from the Perkin-Elmer a-Si two-dimensional (2D) image plate detector. Data processing from 2D to 1D (Q space) was performed using a CeO_2 calibration standard. Conversion to the PDF pattern ($G(r)$) and structural model fitting onto the PDF data were successively performed with the programs; Fit2D, used for data extraction from 2D to 1D; PDFgetX2, used for data analysis and PDF pattern generation; and PDFgui used for structural model fitting and refinement.(Hammersley [145], Qiu et al. [146], Farrow et al. [147])

3.3 Theoretical results and discussion

3.3.1 $Ba_2In_2O_5$ phase

Cluster expansion: The DFT energies for $Ba_2In_2O_5$ were reasonably well reproduced by a CE with a cross validation (CV) score of 15.9 meV, where the CV score is as defined in the ATAT documentation (van de Walle et al. [102]) giving a measure of wellness of the DFT to CE fit, the smaller the value the better fit. The effective cluster interactions (ECIs) were found to be physically reasonable, in that they became progressively weaker with increasing inter-site distance, reaching a pair distance of 7.98 Å(pair 9 in Figure 3.2 and 3.3a). Pair 9 connects two non-adjacent InO_6 octahedra oxygen sites and physically defines the brownmillerite type alternating octahedral and tetrahedral layers. The corresponding pair and triplet clusters are shown in Figure 3.3(a) and 3.3(b) respectively. The strongest interaction corresponds to the first O-O pair interaction (Figure 3.2 and 3.3a), where the large positive value indicates a high degree of O-O and vacancy-vacancy repulsion. The pair interactions generally decrease in strength with increasing distance to pair 6, save for pair 2 which is noticeably smaller. Pair

2 and pair 3 both correspond to the next-nearest neighbor O-O interactions, however, pair 2 has an intervening In in between the two O sites, which presumably screens the OO interactions.

The longer ranged pairs, such as 7 and 9, have larger ECIs than the shorter ranged 5 and 6 pairs. This non-monotonic trend in the ECI is likely a consequence of the fact that pairs 7 and 9 connect two non-adjacent perovskite unit cells, and are therefore responsible for the second shell ordering (alternating layers of InO_6 and InO_4) typical of the brownmillerite-type structure.

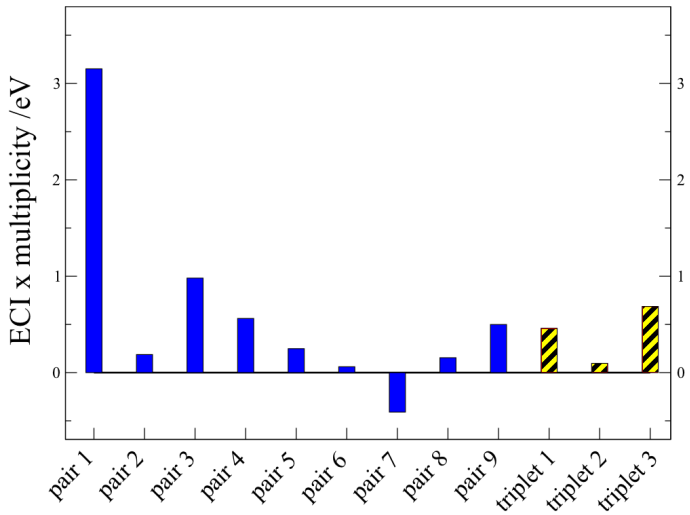

Figure 3.2: Pair and triplet ECIs in BIO, where the ECIs include the respective cluster multiplicities. The labeling of pairs and triplets is as in Figure 3.3.

Examining the triplet ECIs, and using the site assignment of O to (-1) and Vac to (+1), it is found that the location of three oxygen atoms next to each other $[(-1) \times (-1) \times (-1) \times \text{ECI}]$ is favoured, and three vacancies, disfavoured, as is clear from the large positive ECIs for triplets 1 and 3. An intervening In site affects these interactions: both triplets 1 and 3 are directly related to the InO_6 octahedra, while the second triplet connects sites between different InO_6 octahedra and the interactions are not screened by an intervening In site (Figures 3.2 and 3.3b).

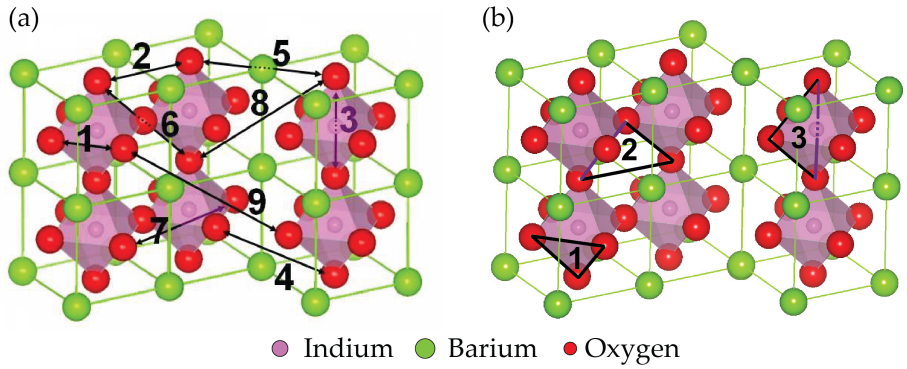

Figure 3.3: The (a) nine pair- and (b) three triplet-clusters in BIO.

Monte Carlo simulation: Monte Carlo simulations were used to find the CE Hamiltonian ground state by cooling from 3000 K in steps of 10 K and then equilibrating at 10 K. The CE Hamiltonian ground state was found to match the brownmillerite type ground state structure of $Ba_2In_2O_5$. Octahedral InO_6 and tetrahedral InO_4 groups, alternating along a single perovskite lattice vector, are observed, as in Figure 3.1. An increase in temperature yields two phase transformations, as shown in the plot of site energy vs. temperature in Figure 3.4. The lower temperature phase transformation at approximately 1030 K (located from a peak in the graph of $\frac{\delta E}{\delta T}$) is first-order in character, while the second transformation at approximately 1930 K (located approximately as a peak in the graph of $\frac{\delta^2 E}{\delta T^2}$) is of a second-order type. The calculated transitions qualitatively match the experimental phase transformations temperatures of 1223 and 1313 K (Speakman et al. [12]), particularly in terms of the character of the transitions. It is difficult to assign a space group to the higher temperature structures, due to the progressive increase in disorder in the MC cell. However, the MC site correlations can be transformed to yield specific oxygen site occupancies, which may then be tracked as a function of temperature yielding further insight into the structural changes underlying the phase transformations, as shown in Figure 3.5.

At low temperatures, the equatorial octahedral O1 and apical O2 sites are fully occupied and the equatorial tetrahedral O3 sites are half occupied. The

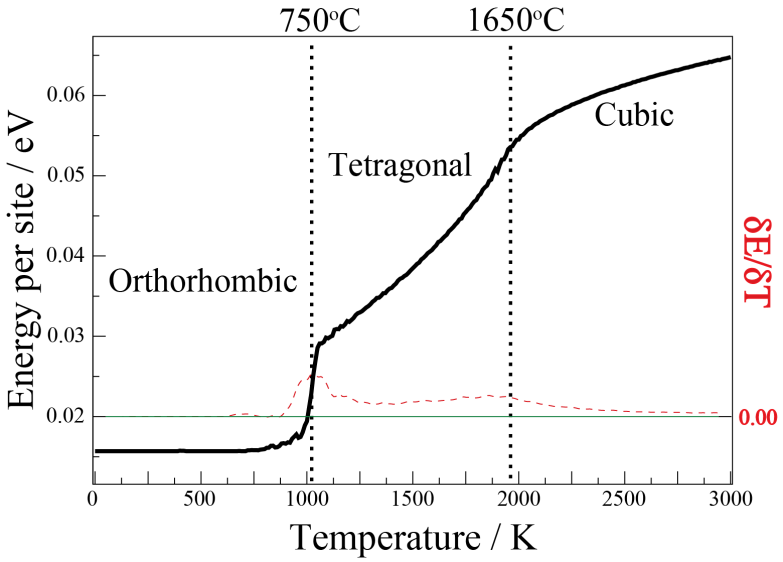

Figure 3.4: The energy vs. temperature plot of BIO as obtained from MC simulations.

first phase transformation corresponds to a decrease in O2, and a corresponding increase in O3 occupancies, indicating exchange between the O2 and O3 sublattices, i.e., between the InO_4 oxygen atoms. The first phase transformation is also the beginning of disorder in the tetrahedral indium-oxide clusters plane, as observed by the degeneracy of the O3 sites in the MC simulations (i.e., both the O3 sites and vacancies shown in Figure 3.1 are occupied). Such disorder should make the formerly distinct orthorhombic a and b axes equivalent (assuming that c is the long axis), resulting in the tetragonal structure observed experimentally by Speakman et al. [12]. Beyond the second phase transformation, disorder over all oxygen sites is observed, consistent with the formation of the disordered cubic structure. High temperature oxygen site disorder was also confirmed by visualizing series of MC configurations at 2500 K.

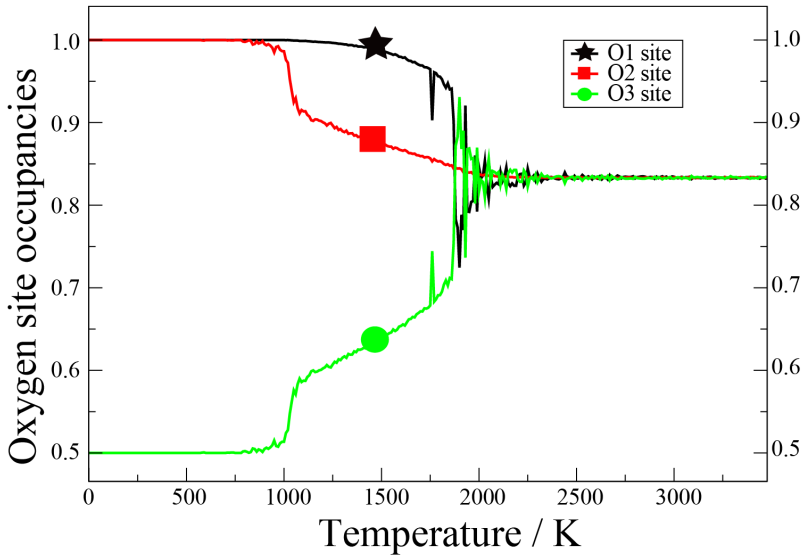

Figure 3.5: The variation in the occupancies of BIO O1, O2 and O3 sites with temperature, as obtained from MC simulations. The oxygen labeling schemes are the same as those used in Figure 3.1.

3.3.2 $Ba_2(In_{1-x}Ga_x)_2O_5$ phase

Formation energies and convex hull from DFT calculations: To address the phase stability of $Ba_2(In_{1-x}Ga_x)_2O_5$ we first carried out a study of the triple phase diagram containing the known stable phases formed from the BaO, β-Ga_2O_3 and In_2O_3 end-members (Figure 3.6a). Then we studied the convex hull of formation energies from the end members $Ba_2In_2O_5$ and $Ba_2Ga_2O_5$ (both brownmillerite type structured), indicated as a green dashed line in Figure 3.6a and detailed in Figure 3.6b. The phase stability problem is typically addressed with first principles computations on a large set of candidate structures. Here we generated these candidate structures with the ATAT code as same as the one we used for the $Ba_2In_2O_5$ system analysis in previous section.

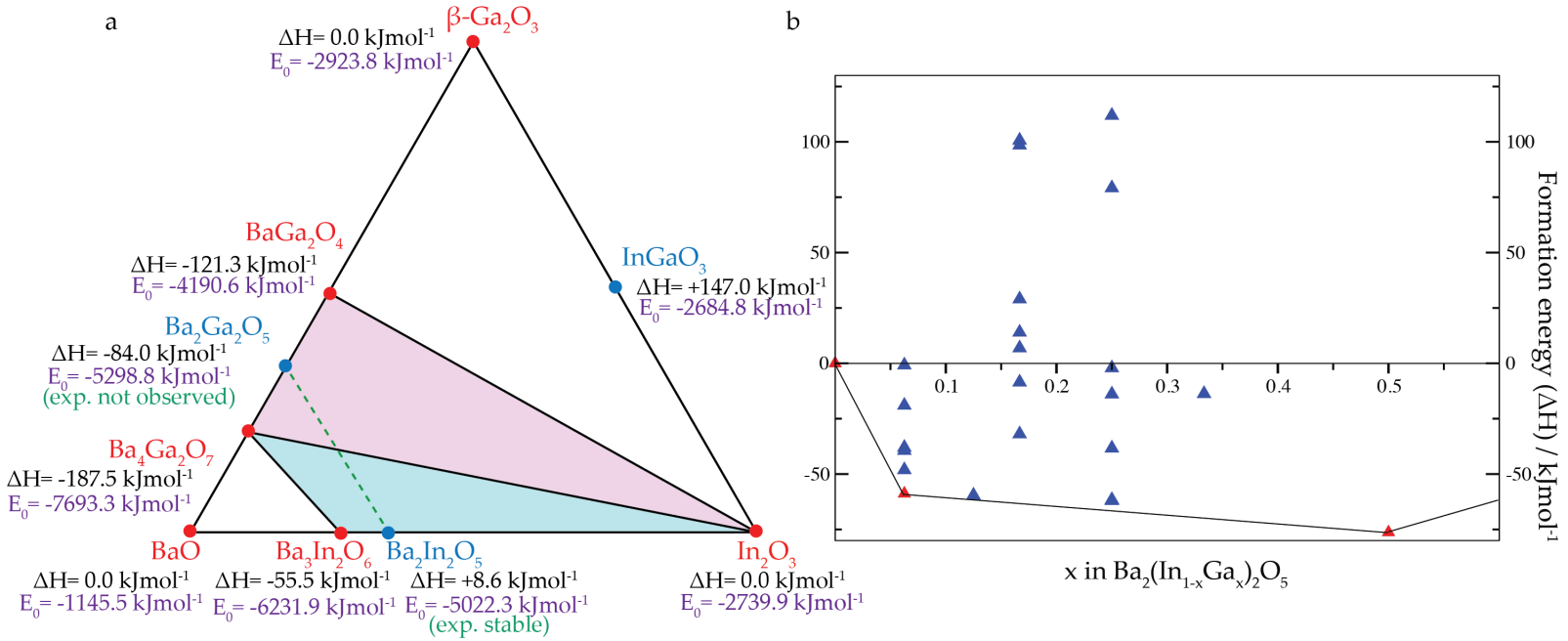

Figure 3.6: a) A triple phase diagram from BaO, β-Ga_2O_3 and In_2O_3 end-members. Where red circles are stable and blue circles are meta-stable structures. The $Ba_2(In_{1-x}Ga_x)_2O_5$ tie line is shown by a dashed green line located over two smaller triple phase boundaries, pink for $x \geq 0.5$ and blue for $x \geq 0.5$. b) Convex hull showing the formation energies of $Ba_2(In_{1-x}Ga_x)_2O_5$ structures, from $Ba_2In_2O_5$ to $Ba_2(In_{1-x}Ga_x)_2O_5$, $x = 0.5$. Where red triangles are stable and blue triangles are meta-stable structures. ΔH is the enthalpy of formation of the different structures from the end-members and E_0 is the DFT calculated energy for each structure.

As a result of our DFT calculations on the triple phase diagram (Figure 3.6a) the two end-members of $Ba_2(In_{1-x}Ga_x)_2O_5$, brownmillerite type structured $Ba_2In_2O_5$ and $Ba_2Ga_2O_5$, appear to be unstable with ∼55 kJmol^{-1} and ∼71 kJmol^{-1} stabilization energies (from ΔH), respectively, calculated from tie line stable structures enthalpies and the enthalpies of formation of relevant structures. This result is in contradiction with the experimental fact that brownmillerite type structured $Ba_2In_2O_5$ is a stable compound with the $Ibm2$ or $Icmm$ space group as shown in section 3.4. This might be explained with the higher amount of tilting of polyhedra, atomic site disorder (both In and O in $Icmm$ space group are disordered (Speakman et al. [12])) and hence higher change of entropy for the formation of the $Ba_2In_2O_5$ system compared to the tie line stable structures $Ba_3In_2O_6$ and In_2O_3. Experimentally, $Ba_2Ga_2O_5$ with the $Ibm2$ space group (or any other) is not observed in agreement with our calculations.

The convex hull shows phases with lower formation energies with respect to the end members, $Ba_2In_2O_5$ for x=0 and $Ba_2Ga_2O_5$ for x=1. We are mainly focused on the low substitution level part of the convex hull because higher Ga substitution levels are experimentally known to be unstable (see section 3.4). We take the x=0.5 to be the highest Ga concentration, similar to the study by Yao et al. [2], apart from the end member $Ba_2Ga_2O_5$ on the x=1. At higher Ga concentrations, the formation energy per unit cell decreases, and thus the x=0.5 structure represents a lowest energy state structure. Due to inadequate sampling we can not take this structure as the ground state structure. However this structure ($x = 0.5$) has a common brownmillerite type structure with all three lowest energy structures (at $x = 0.0625$, 0.125 and 0.25) on the convex hull having a Ga in tetrahedral coordination.

For the $Ba_2(In_{1-x}Ga_x)_2O_5$ with $x = 0.06$, the structure with a single, tetrahedrally-coordinated Ga in a super-cell consisting of 8 brownmillerite type unit cells ($4 \times 2 \times 2$ perovskite supercell) containing alternating octahedral and tetrahedral B cation layers, represents the ground state structure for this concentration (within the structures sampled here) and is also a sample of the biggest super-cell. We compare $x = 0.5$ structure with the lowest energy structure having the biggest super cell in order to achieve a better understanding of the Ga environment without a Ga-Ga nearest neighbor interaction. When we look at the

$Ba_2(In_{1-x}Ga_x)_2O_5$ with $x = 0.5$ structure, a $2 \times 1 \times 1$ supercell of a simple brownmillerite (equivalent to $2 \times 2 \times 1$ perovskite supercell), we observe Ga atoms in a tetrahedral coordination next to each other forming the tetrahedral layer of the brownmillerite type structure and other B site atoms consist of In atoms in an octahedral coordination. We observe that the Ga and In atoms are ordered, with Ga occupying the BO_4 sites and In the BO_6 sites.

Examining only the convex hull in figure 3.6b, indicates that stable Ga doping is possible and system becomes more stable with increasing Ga concentration ($Ba_2(In_{1-x}Ga_x)_2O_5$ at $x = 0.06$ with ΔH = -59 kJmol^{-1} and at $x = 0.5$ with ΔH = -76 kJmol^{-1} on Figure 3.6b). Placing the convex hull on the triple phase diagram (green dashed line on Figure 3.6a) we observe that there are two smaller triple phase boundaries, first the $Ba_3In_2O_6$–$Ba_4Ga_2O_7$–In_2O_3 (lower blue triangle on Figure 3.6a) for the $Ba_2(In_{1-x}Ga_x)_2O_5$ with $0.0 \geq x \geq 0.5$ and second the $Ba_4Ga_2O_7$–$BaGa_2O_4$–In_2O_3 (upper pink triangle on Figure 3.6a) for the $0.5 \geq x \geq 1.0$ phases. Structures of $Ba_2(In_{1-x}Ga_x)_2O_5$ at $x = 0.0$, 0.0625, 0.125, 0.25 and 0.5 with formation enthalpies (ΔH) of +45.6, -11.9, -11.6, -11.2 and -20.3 kJmol^{-1} respectively, lie on the first triple face boundary with $Ba_3In_2O_6$, $Ba_4Ga_2O_7$ and In_2O_3 end members. We observe that increase in Ga concentration, greatly improves the stability from $x = 0.0$ to 0.0625, later slightly reduces the stability of the system from $x = 0.0625$ to $x = 0.25$, but again improves the stability for the $x = 0.5$ phase. The high Ga concentration structures at $x = 0.5$ and 1.0 with formation enthalpies (ΔH) of -20.3 and +59.4 kJmol^{-1} respectively, fall on the second triple phase boundary with $Ba_4Ga_2O_7$, $BaGa_2O_4$ and In_2O_3 end members. In this region we observe that increasing Ga concentration results in destabilization of the system.

With the formation enthalpies study, $Ba_2In_2O_5$ is observed as a metastable phase. However, $Ba_2In_2O_5$ is experimentally a stable phase (see section 3.4). Therefore in addition to formation enthalpies (ΔH), entropy change of formation (ΔS) due to disorder in In and O lattices, in *Icmm* space group as reported by Speakman et al. [12] and Berastegui et al. [13], should also be considered. Experimentally we observe stable $Ba_2In_2O_5$ and unstable $Ba_2Ga_2O_5$ phases, which can be explained by a decrease of disorder in In and O sublattices due to an increase in Ga concentration. Therefore combination of relatively unchanged ΔH of $\sim$ -11

kJmol^{-1} for $x = 0.0625$, 0.125 and 0.25 phases and decreasing ΔS with increasing Ga concentration might result in metastable $Ba_2(In_{1-x}Ga_x)_2O_5$ phases, which is further supported by our experiments in section 3.4.

Multi-component cluster expansion: The initial fitted CE for $Ba_2(In_{1-x}Ga_x)_2O_5$ with x 0.5 consisted of 16 ECIs, yielding a CV score of 16 meV. While this CE produced a Brownmilleride type ground state structure, with alternating octahedral and tetrahedral indium oxide layers, at x = 0 the CE was unable to represent the second high temperature phase transformation accurately. Further investigation revealed that the initial $Ba_2(In_{1-x}Ga_x)_2O_5$ CE lacked the long range ECIs present in the $Ba_2In_2O_5$ CE at distances beyond 6.03Å. In particular, the pair interaction numbers 7 and 9 in Figure 3.2 and 3.3a linking oxygen sites of non-adjacent perovskite unit cells in $Ba_2In_2O_5$ was missing. Such second-shell interactions are very important in brownmillerite-related phases, given that they determine the stacking order of InO_6 and InO_4 units. On this basis, a CE comprising 23 ECIs was substituted (Figure 3.7), in which the long-range interactions were included, yielding a CV score of 25 meV. This longer-range CE does not yield as low a CV score as the shorter-range fit with 16 meV but we believe it better represents the key long-range interactions in the system and is therefore more physical.

The resulting O-O ECIs in $Ba_2(In_{1-x}Ga_x)_2O_5$ are similar to those in $Ba_2In_2O_5$, the first pair being the strongest, the ECIs progressively weakening with distance thereafter, save for the pair 2 and the second-shell interactions represented by pairs 7, 8 and 9. Using the site assignment of O to (-1), Vac to (+1), In to (-1) and Ga to (+1) it is found that the In-O ECIs p1 and p2 indicate first shell repulsion and second-shell p3-p5 attraction for In-O pairs, which also means that Ga-O pairs have, conversely first-shell attraction and second-shell repulsion. The most significant triplet ECI corresponds to an O-In-O attraction. This ECI also represents O-Ga-O and O-In-Vac repulsions. The interactions featuring two In sites are the weakest, and are all repulsive for the In-In pair, which in return permits In-Ga pairs to be slightly attracting each other. This association of In-Ga pairs might yield an ordering of In and Ga at low temperatures which was observed in the previous section for the $Ba_2(In_{1-x}Ga_x)_2O_5$ with $x = 0.5$ (Figure 3.7).

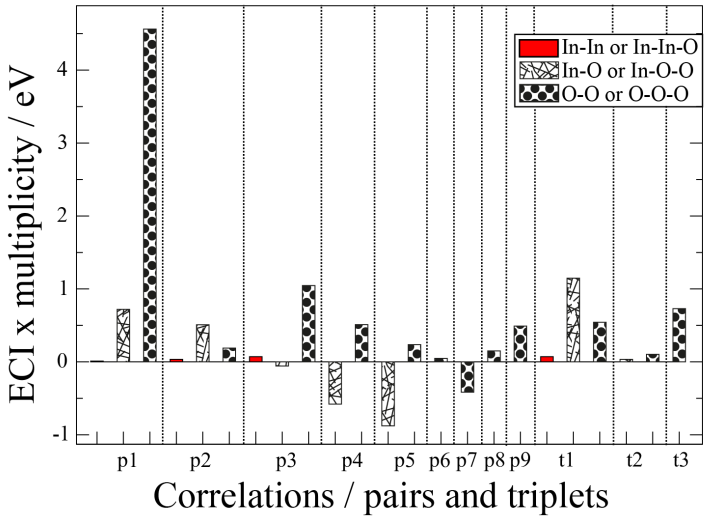

Figure 3.7: Pair and triplet ECIs in BIGO, where the ECIs include the respective cluster multiplicities. Here p1 denotes the shortest-range pair, p2, the next-shortest pair etc. irrespective of their type being In-In, In-O or O-O.

Clusters used in the CE of $Ba_2(In_{1-x}Ga_x)_2O_5$ can be seen in Figure 3.8. Here, just the In-In pair- and In-In-O triplet-clusters (Figure 3.8a) and In-O pair- and In-O-O triplet-clusters (Figure 3.8b) are illustrated. The O-O pair- and O-O-O triplet-clusters are exactly as in the pure $Ba_2In_2O_5$ CE illustrated in Figure 3.3.

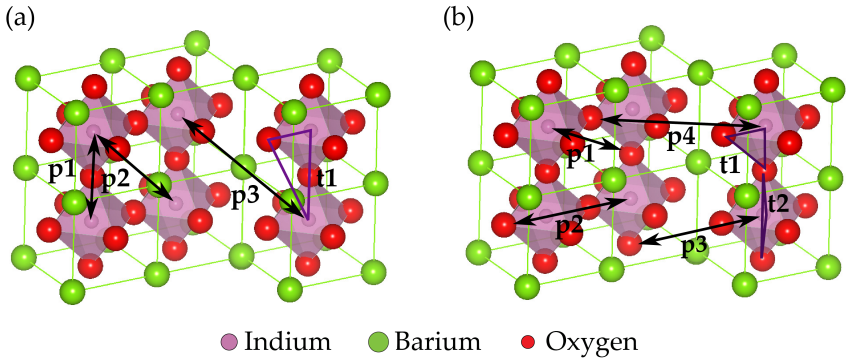

Figure 3.8: BIGO (a) In-In pair- and In-In-O triplet- (b) In-O pair- and In-O-O triplet-clusters as labeled in Figure 3.7. The O-O pair- and O-O-O triplet-clusters are as same as in Figure 3.2. For clarity, in BIGO CE the pn/tn (n being an integer number) notation is used where as for BIO CE only numbers were used (see Figure 3.3 and 3.2). Also note that types of clusters, In-In(-O) and In-O(-O) are represented in groups, labeled as one, for simplicity of presentation.

Full multi-component Monte Carlo simulations: The $Ba_2(In_{1-x}Ga_x)_2O_5$ phases at $x = 0$, 0.125, 0.166, 0.25 and 0.33 are studied by MC simulations in which both the B site cations and anions are allowed to move within the cell. As expected, the x = 0 limit yields energetics and phase transformations that are very similar to those obtained in $Ba_2In_2O_5$ (section 3.3.1)(Lee and Morgan [136]).

The temperature vs. energy graphs shown in Figure 3.9 for the range of stoichiometries indicate two phase transformations for the undoped $Ba_2In_2O_5$ system, and suppression of the second phase transformation in the Ga-doped phases. Unexpectedly, the first phase transformation shifts to higher temperature with increasing Ga content in contradiction of the previous experimental study by Yao et al. [2], which suggested the opposite trend. The theoretical finding is attributed to phase transformations occurring within the segregated sub-domains created by the Ga ordering (see section 3.3.2 for the $x = 0.5$ phase), and would not be expected if we had a homogeneous phase with uniform Ga distribution within $Ba_2(In_{1-x}Ga_x)_2O_5$ (see section 3.3.2). In other words, due to the anion and cation ordering, the transformation to the high temperature cubic phase (which contains homogeneous Ga distributions) must involve disordering of both

the anion and cation sublattices. Separate heating and cooling curves reveal the presence of strong hysteresis in the first order phase transformation, the hysteresis width decreasing with increasing Ga content. This effect may be due to smaller phase fraction of the ordered sub-domain within the system and also because the transitions occur at higher temperatures. We note that the energy-temperature curves at low temperature often differ upon cooling or heating; this is an artifact of the finite equilibration steps used, but it is impractical to run MC for long enough to find the true equilibrium state at low temperature. Simply put, the system at low temperature cannot overcome the energy barriers separating the initial brownmillerite and ordered configurations, only finally doing so by virtue of sufficient heating; letting the MC simulations evolve for longer time should in principle produce a similar result.

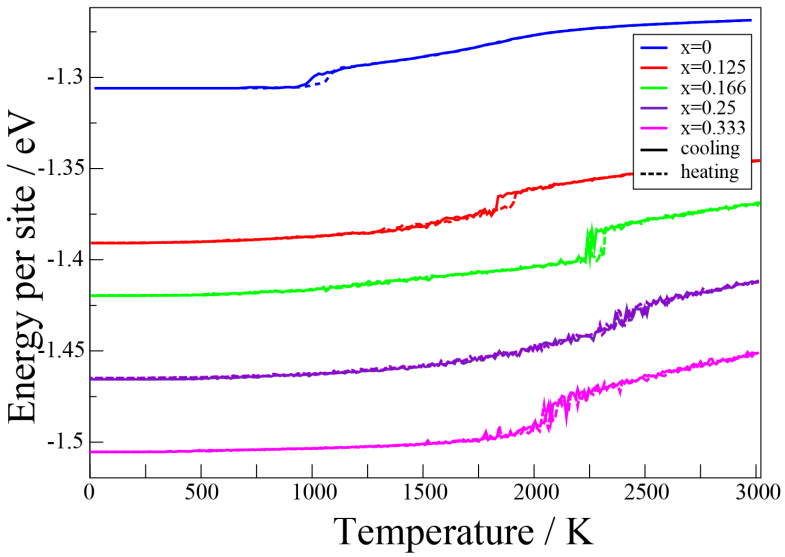

Figure 3.9: Monte Carlo simulations, energy-temperature curves in $Ba_2(In_{1-x}Ga_x)_2O_5$ (BIGO) as a function of Ga concentration.

Mean field Monte Carlo simulations: Previous experimental x-ray diffraction studies do not provide any evidence of Ga/In ordering or phase segregation, nor does our experimental investigation on samples prepared by rapid cooling as

will be described in Section 3.4.1 (Figure 3.14). The present MC simulation however, permitting both In, Ga and O, and Vac movements, yields phase separated or clustered equilibrium conditions, as discussed in the formation energies section (3.3.2) and full multi component Monte Carlo simulations section (3.3.2). We believe that the discrepancy between our model and the previous experimental work is due to the Ga and In being immobile during the experimental studies due to quenching effects. Therefore, in order to more realistically model the experiments, it is necessary to freeze in a disordered Ga/In arrangement in the simulations. In order to include the effects of this disordered Ga/In environment we adopt a mean-field approach, wherein each site upon the In sublattice is occupied by a notional atom comprising fractions of In and Ga species consistent with the overall phase stoichiometry. We note that this approach bears close similarities to the virtual crystal approximation often adopted for disordered alloys by [148]. The virtual crystal approximation however differs from our approach by typically being used for approximate treatment of quantum mechanical problems. The mean-field ECI are provided in the supplemental information.

Within the mean-field approach all $Ba_2(In_{1-x}Ga_x)_2O_5$ ground states reveal an orthorhombic, or tetragonal, brownmillerite type of structure with alternating layers of octahedra and tetrahedra, with high disorder in O sites. Considerable amount of distortion in the tetrahedral layer is observed. Five coordinated InO_5 polyhedra are observed in both octahedral and tetrahedral layers (Figure 3.10). At $x = 0.25$, the orthorhombic brownmillerite structure with a space group and appropriate primitive cell determined by symmetry analysis of an averaged MC supercell using the FINDSYM web page by Stokes and Hatch [143] is in contradiction of the cubic symmetry proposed by the diffraction study of Yao et al. [2] and the experiments detailed in section 3.4. Examining the energy-temperature curves shown in Figure 3.11, two phase transformations are again evident for most phases, being of first- and second-order type at low and high temperatures, respectively. All of the transformations shift to lower temperatures with increasing Ga concentration, and we note in particular that the first-order phase transformation apparently disappears entirely for $x \geq 0.25$, as observed indirectly in experimental measurements of conductivity by Yao et al. [2].

It is clear that freezing the Ga/In sublattice in the mean-field MC simulations

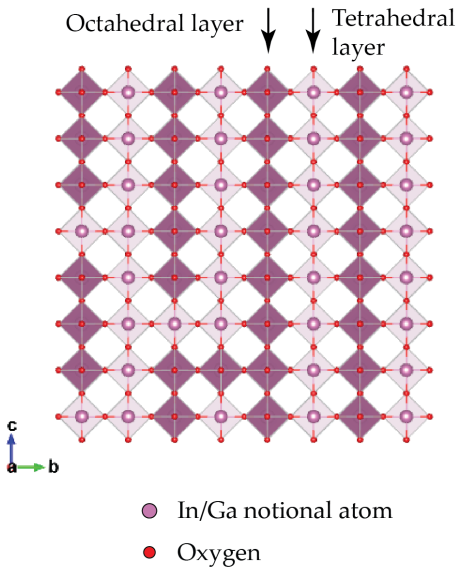

Figure 3.10: Ground state structure of $Ba_2(In_{1-x}Ga_x)_2O_5$ with $x = 0.33$ at 10 K, as obtained from mean field MC simulations.

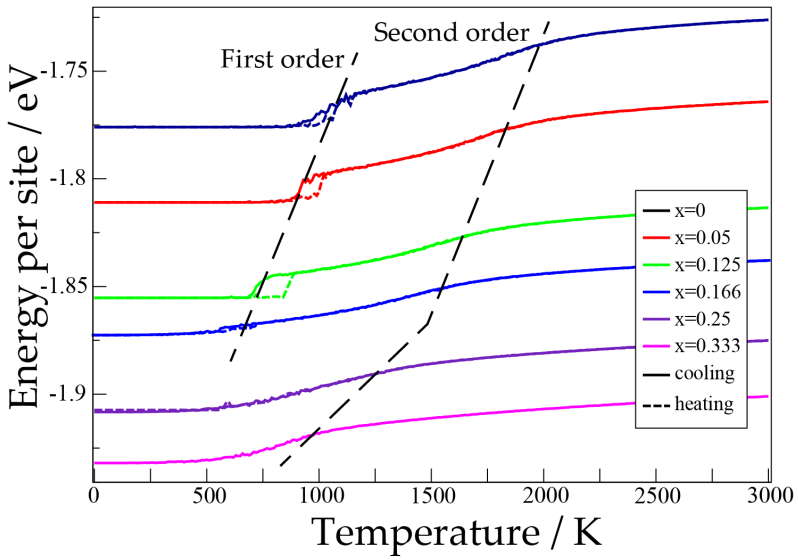

Figure 3.11: Energy-temperature curves in in $Ba_2(In_{1-x}Ga_x)_2O_5$ at various Ga concentrations, as obtained from mean field MC simulations.

reproduces the experimentally observed reduction in temperature and eventual loss of the first-order phase transformation.(Yao et al. [2]) However, the theory predicts an ordered brownmillerite like ground state and an eventual second-order transition to the cubic phase happening gradually with increasing temperature, while the experimental results seem to suggest that the cubic phase is stable at low temperature. Further work is needed to understand and remove this remaining discrepancy.

3.3.3 Density of states (DoS)

The electronic structures of $Ba_2In_2O_5$ and $Ba_2(In_{1-x}Ga_x)_2O_5$ are compared by analysis of computed densities-of-states (DoS) plots. This is a key point, given that Ga-doping will ultimately be unacceptable should it lead to increased electronic conductivity under SOFC operating conditions. Here the DoS plots of three configurations are considered: undoped $Ba_2In_2O_5$ with the brownmillerite type of structure, which is the ground state, and two $x = 0.25$ $Ba_2(In_{1-x}Ga_x)_2O_5$ structures, the first containing exclusively tetrahedrally- and the second exclusively octahedrally-coordinated Ga cations, both in a brownmillerite type O ordering. This choice was made so as to be able to compare Ga environments rather than the structural changes occurring with the presence of Ga in the structure. We pay close attention in particular to the energy gap separating the uppermost valence (VBE) and the lowermost conduction band edge (CBE) states, given that, in an intrinsic semiconductor, electronic conduction proceeds only by thermal excitation of carriers across the band gap. While DFT suffers from well-known problems in relation to underestimation of the band gap of insulators and semiconductors (Perdew [149], Perdew et al. [150]), the relative variations induced by Ga-doping should be reliable. Figure 3.12 shows the computed DoS plots, where the VBE energy is set as zero in each case for ease of comparison. It is clear that substituting Ga into exclusively octahedral sites (within the brownmillerite type O ordering) does not appreciably alter the electronic structure beyond that of $Ba_2In_2O_5$, whereas doping into tetrahedral site leads to a 0.3 eV increase in the band gap to 1.2 eV. Experimental value of 3.02 eV band gap for $Ba_2In_2O_5$ by UV-vis experiments is reported by Wang et al. [151]. In neither case does

Ga-doping decrease the gap width. The dominant atomic character for the VBE is O 2p, and for the CBE is combination of O 3s and In 5s.

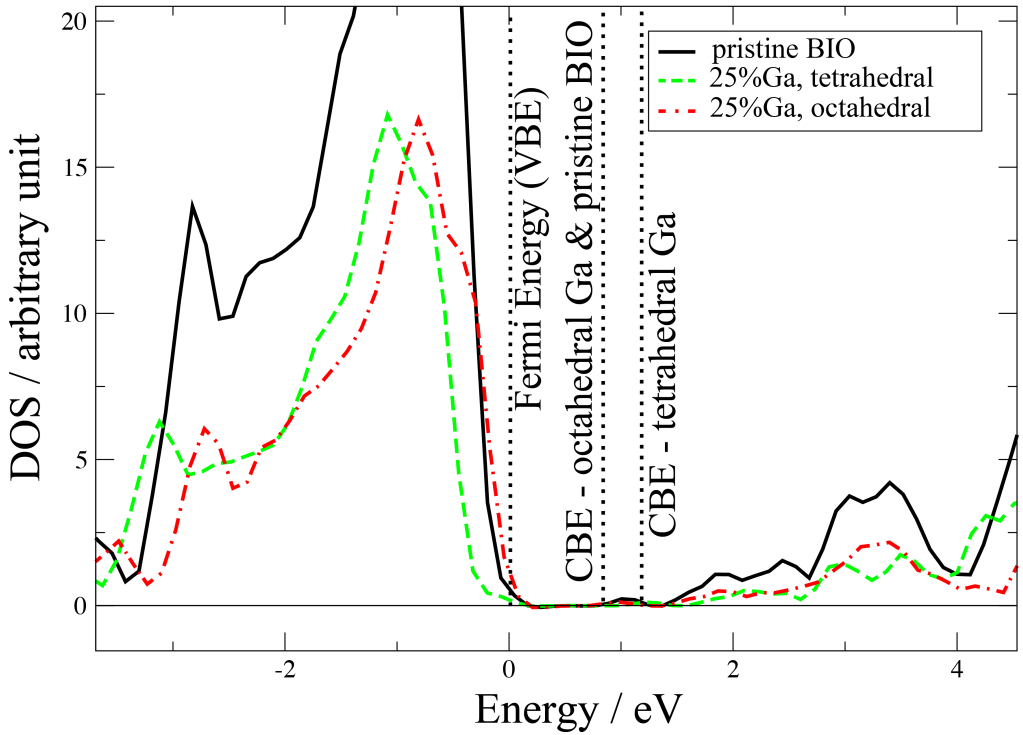

Figure 3.12: Electronic densities-of-states (DoS) plot of BIO and two x = 0.25 BIGO configurations all with brownmillerite type O ordering. Respective valance band edges (VBE) have been aligned to zero in energy. Conduction band edges (CBE) are also shown.

3.4 Experimental Results and Discussion

3.4.1 X-ray diffraction

Powder x-ray diffraction at room temperature yields insight into the structure and the purity of the various synthesized $Ba_2In_2O_5$ and $Ba_2(In_{1-x}Ga_x)_2O_5$ phases. The previous diffraction study of Yao et al. [2] reveals a brownmillerite-type O ordering for undoped $Ba_2In_2O_5$ and a cubic structure for Ga doping of $Ba_2(In_{1-x}Ga_x)_2O_5$ with $x \geq 0.25$ up to $x < 0.50$. Our observations at low doping levels ($x < 0.3$) are similar. However, for $x \geq 0.3$ $Ba_2(In_{1-x}Ga_x)_2O_5$ systems display a tendency to phase separate (Figure 3.13). This phase separation is strongly related to the rate at which the samples are cooled from the high temperatures used in their synthesis.

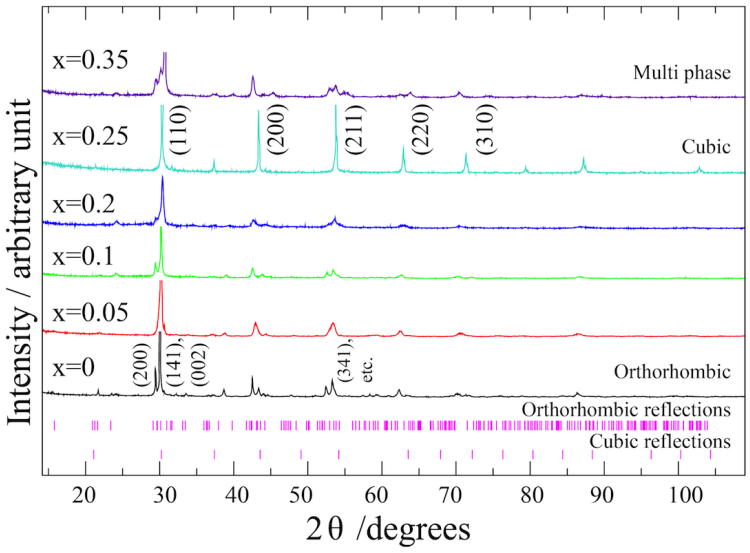

Figure 3.13: X-ray diffraction of slow cooled $Ba_2(In_{1-x}Ga_x)_2O_5$ with increasing Ga doping levels

The room temperature XRD patterns of the $Ba_2In_2O_5$ and $Ba_2(In_{1-x}Ga_x)_2O_5$ phases synthesized by moderately slow cooling from 1573 K reveal the presence of an orthorhombic brownmillerite-type structure for undoped $Ba_2In_2O_5$ and low-moderate Ga substitution levels. The orthorhombic form persists to $x = 0.2$,

albeit with increased peak widths for XRD pattern of this phase consistent with the presence of disorder, decrease in particle size, or both. Since the preparation route, mechanical grinding conditions and synthesis temperatures were same for all the samples, the increased peak broadening is most likely due to smaller coherence lengths for the ordering and/or increased disorder. The $x = 0.25$ material is apparently cubic but the diffraction patterns of the $x = 0.3$ (not shown) and 0.35 sample reveals two phases, one of which is orthorhombic. Attempts were made to index the two phases in the $x = 0.35$ sample, but unfortunately, the effects of peak overlap rendered a le Bail fit and refinement of the second phase unreliable. Recognizing that the cooling routine used to minimize hydration of the samples (involving cooling of samples in a desiccator) is still relatively fast, taking about 2 hours to cool from 1573 K to room temperature, further experiments were performed where samples were slowly cooled in sealed oxygen-containing quartz tubes for over 4 hours (5 °C/min), but the results were similar to those performed with the route described here. In contrast, quenching (at 100 °C/min) of the Ga-doped materials at the end of the synthesis results in an orthorhombic structure up to $x = 0.15$ and a cubic structure above this doping level even at room temperature (Figure 3.14).

In order to explore the reversibility of some of the phase segregations, the quenched samples were then annealed at lower temperatures for longer time periods. Figure 3.15 illustrates the effect of annealing at 1073 K and then subsequent quenching of the $x = 0.25$ $Ba_2(In_{1-x}Ga_x)_2O_5$ sample. This sample was chosen because it adopts a cubic structure on quenching and on moderately slow cooling from 1573 K. By contrast, annealing this sample at 1073 K yielded a multiphase system. Three phases were identified in a le Bail fit to the data, corresponding to a brownmillerite-type orthorhombic, a cubic structure, and a monoclinic structure with similar cell parameters to $BaIn_2O_4$ ($P12_1/a1$ (No:14) space group). We note, however, that there is no Ga bearing structure in the ICSD that matches the third phase extracted from Le Bail refinement. The major reflections due to this third phase are indicated with stars in Figure 3.15. Re-heating of the phase-separated $x = 0.25$ sample to 1573 K and subsequent quenching reforms the cubic structure, indicating that Ga is still present in the system and that there is no loss of Ga during the annealing step (Figure 3.15).

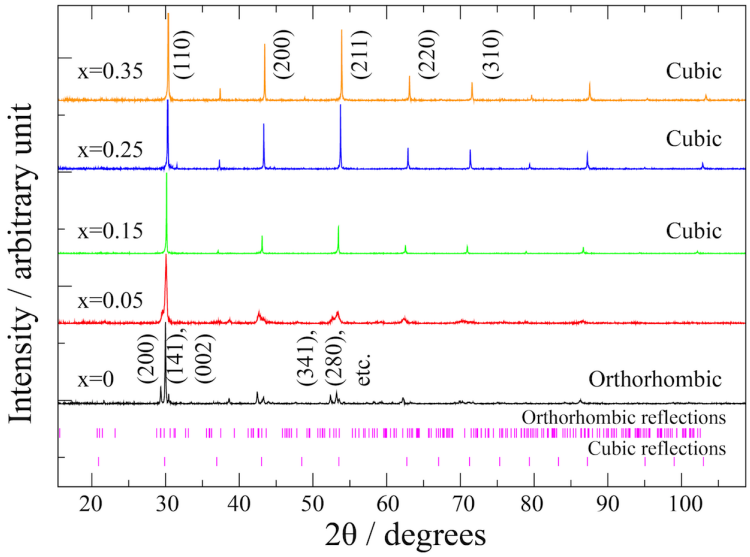

Figure 3.14: X-ray diffraction of quenched $Ba_2(In_{1-x}Ga_x)_2O_5$ with increasing Ga doping levels

The cell volumes were extracted for all the samples via a le Bail fit and were compared by converting them to those corresponding to a single perovskite cell. An increase in the Ga concentration in $Ba_2(In_{1-x}Ga_x)_2O_5$ leads to a decrease in the crystallographic unit cell volume. However, an increase in the Ga-doping levels also causes the x-ray diffraction peak widths to increase, leading to problems of peak overlap and peak position reading, and to greater experimental error in unit cell volume determination. Nevertheless, a significant difference between the normalized unit cell volumes can be observed for higher doping levels between the quenched and the slow cooled synthesis (Figure 3.16). In the case of the $x = 0.35$ slow cooled sample, the data shown here corresponds to the cell parameters of the indexed orthorhombic phase, and the noticeable increase in its cell volume over that of the quenched sample strongly suggests that this orthorhombic phase is Ga deficient, while the unindexed phase is richer in Ga. The smaller cell volume of the slow cooled cubic $x = 0.25$ sample (in comparison to the cubic $x = 0.25$ quenched sample) suggests that this sample is starting to phase segregate and that a second phase or domain, which is deficient in Ga (and thus has a larger cell volume) but which has a coherence length that is too small to be clearly

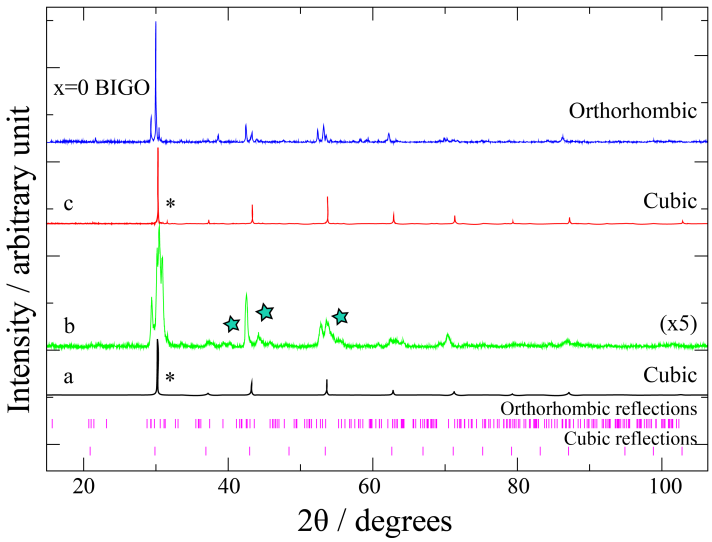

Figure 3.15: X-ray diffraction patterns of $x = 0.25$ $Ba_2(In_{1-x}Ga_x)_2O_5$ annealed at 1073 K. The patterns (a) before annealing at 1073 K, (b) after annealing and (c) after reheating at 1573 K and subsequent quenching are shown, along with that of orthorhombic $Ba_2In_2O_5$ (added for comparison). The stars at 40.2°, 45.8°and 55.5°2θ indicate reflections that cannot be attributed to either an orthorhombic or cubic $Ba_2(In_{1-x}Ga_x)_2O_5$ phase. The asterisks indicate peaks arising from impurities seen in the cubic phases.

detected by XRD, is also present.

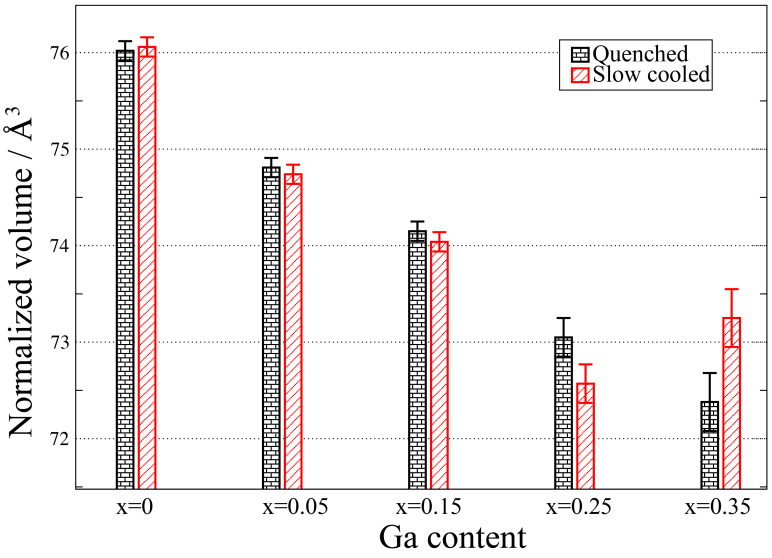

Figure 3.16: Normalized volume of quenched and annealed $Ba_2(In_{1-x}Ga_x)_2O_5$ with increasing Ga percentages

3.4.2 Pair distribution function analyses

The long- and short-range structural changes due to increasing Ga-doping were investigated by application of x-ray pair distribution function (PDF) analyses. The PDF shows the probability of occurrence of a specific atomic pair, weighted by the product of the scattering factors of the relevant atoms and plotted against the corresponding separations of the atom pairs. The PDF analysis of slow-cooled $Ba_2In_2O_5$ and $Ba_2(In_{1-x}Ga_x)_2O_5$ with $x = 0.05$, 0.1, 0.2, 0.25, 0.3 at 50°C is shown in Figure 3.17. Unfortunately, the correlations are dominated by those involving Ba due to the large scattering factor of this species. The small peaks at approximately 3 Å correspond to overlapping In-O and Ba-O pairs, while the first high intensity peak at 3.7 Å can be assigned to Ba-In and Ba-Ba pairs. Progressive increase in Ga content yields no major short-range structural changes up to 8 Å, save for a coalescence of Ba-Ba and In-In peaks around 6 Å in the cubic x=0.25 phase, and broadening of the heavy atom pair peak at 7 Å. The

longer range (8-19 Å) Ba-Ba, Ba-In and In-In distances all apparently contract with increasing Ga content, consistent with the decreasing cell volumes discussed above.

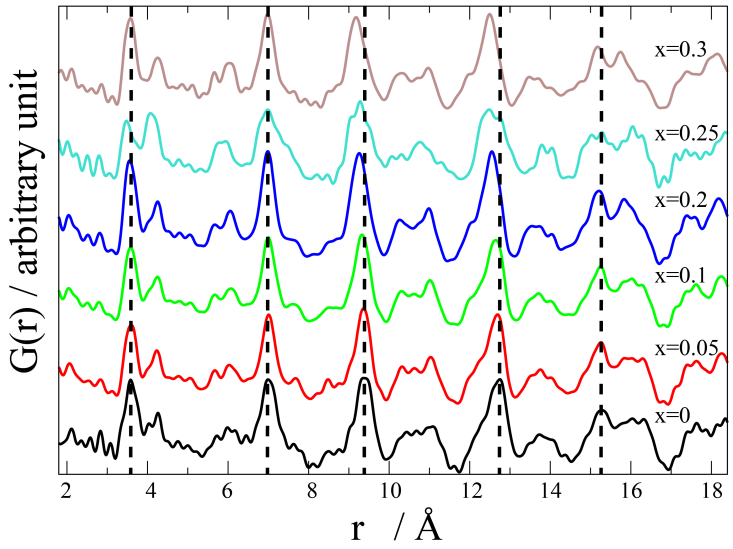

Figure 3.17: PDF of BIO and BIGO at $x = 0.05$, 0.1, 0.2, 0.25 and 0.3 at 50°C. Many of the Ba-Ba, Ba-In(Ga) and In(Ga)-In distances overlap and appear as the most intense peaks. These peaks are indicated with dashed lines for BIO.

3.5 Conclusions

First-principles-derived CE and MC simulations provide the local environment and long-range structures of pristine ($Ba_2In_2O_5$) and Ga-substituted $Ba_2In_2O_5$ ($Ba_2(In_{1-x}Ga_x)_2O_5$) at varying temperatures. They are shown here to work well for the comparatively simpler $Ba_2In_2O_5$ phase. Increasing temperature reveals a first order orthorhombic-tetragonal phase transition, and a subsequent second-order tetragonal-cubic transformation, in accord with the experimental literature (Fischer et al. [48]). The characters of the two phase transformations are therefore well reproduced, albeit with significant errors in onset temperature, the latter likely due to the fact that the differences in vibrational enthalpy and entropy between different states of O ordering are not explicitly considered here. Separate

approaches to the interpretation of the MC data are adopted, namely either averaging site occupancies over many structural snapshots at temperatures of interest or using temperature dependent site correlations obtained directly from the MC simulations. Both reveal the state of O order as a function of temperature, thereby relating directly to the experimental powder x-ray diffraction measurements.

The MC simulation of $Ba_2(In_{1-x}Ga_x)_2O_5$ yielded a brownmillerite-type structure for unsubstituted $Ba_2In_2O_5$ (x = 0), the same result emerging for all levels of Ga-doping under a homogeneous Ga distribution (modeled with a mean-field MC). An increase in Ga concentration, again with homogeneous Ga distribution yields a decrease in both phase transformation temperatures, and, beyond $x = 0.25$, the complete elimination of the first-order phase transformation from orthorhombic to tetragonal symmetry. This loss of the first-order transition is in agreement with experimental measurements (Yao et al. [2]). However, the average configurations form the model at 0 K display a brownmillerite type orthorhombic or tetragonal ordering, while the experimental quenched samples (comparable with the mean field MC results) yield a cubic phase. Phase transformations to cubic symmetry occur at higher temperatures in the presence of increasing amounts of mobile Ga (opposite the trend seen for a frozen in mean-field Ga distribution) and involve both cation and anion redistributions.

The theoretical results are generally supported by x-ray diffraction and pair distribution function (PDF) analyses, the former applied to both quenched and slow cooled samples, the latter only to the slow cooled samples. Samples with $0.35 \geq x \geq 0.15$ were cubic when quenched from high temperature, while slow cooling yielded orthorhombic phases at $x < 0.25$. The $x = 0.25$ phase was cubic following moderately slow cooling, but following annealing at an intermediate temperature and quenching, phase segregation into Ga rich and Ga poor phases was observed, consistent with the theoretical results.

It is clear that an agreement between the theoretical MC simulations and the experimental thermodynamic studies using typical quenching conditions comes only by enforcing a homogeneous Ga distribution. However, both the experiments and the modeling suggest a significant tendency for Ga to form ordered phases. This structural instability of $Ba_2(In_{1-x}Ga_x)_2O_5$ and its tendency to phase separate into different ordered compounds has implications for the long-term sta-

bility of $Ba_2(In_{1-x}Ga_x)_2O_5$ as an SOFC electrolyte material. SOFCs operate in the general region (typically 973-1373K) of the annealing temperature used in this study (1073K). Thus the metastable cubic phase, with its desirable higher anionic conductivity (Yao et al. [2]), will likely phase segregate to form ordered phases with lower conductivities under such conditions. Furthermore, phase segregation is associated with significant changes in cell volume, which may result in the risk of mechanical breakdown of the electrolyte with thermal cycling.

The PDF analyses of $Ba_2(In_{1-x}Ga_x)_2O_5$ shown in Figure 3.17 reveal that the short-range structure of $Ba_2In_2O_5$ (1-8Å) is reasonably well preserved on increase of Ga content. Given that the majority of the doping-induced structural change occurs at longer interatomic distances, the use of the longer ranged CE for Ga containing phases presented in section 3.3.2 is therefore justified, despite the fact that this CE yielded a higher CV score than the shorter ranged alternative.

To conclude, we demonstrate the structural instability of $Ba_2(In_{1-x}Ga_x)_2O_5$ at high Ga contents studied, which in turn suggests that the material with high Ga content may not be a suitable SOFC electrolyte. Beyond Ga, many other B-site substituted elements such as V, Mo and W may be doped into $Ba_2In_2O_5$ (Rolle et al. [49], Shimura and Yogo [152]) together with A-site substituents such as La and Sr (Liu et al. [153], Kakinuma et al. [154]). The long-term phase stability of these candidate SOFC electrolyte materials remain uninvestigated, suggesting an open and potentially important field for further theoretical and experimental investigations. Ab initio and MC simulations together with annealing/quenching experiments and long- and short-range structural probes such as x-ray powder diffraction, PDF analyses and solid state NMR could all play a key role in such studies.

Chapter 4

Structural Characteristics and Dynamics of $Ba_2In_2O_4(OH)_2$ via Experimental and Computational ^{17}O and ^{1}H Solid State NMR

4.1 Introduction

Perovskites are a broad class of materials that find widespread application, notably here as electrolytes for intermediate temperature fuel cells as a consequence of their high O and, when hydrated, their even higher proton conductivities.(Malavasi et al. [106]) The present study focuses on the hydrated form of the $Ba_2In_2O_5$ defect perovskite phase. Chapter 2 considered the dry material. In the dry material, the compensation of the Ba^{2+} and In^{3+} cation charges in $Ba_2In_2O_5$ requires the removal of one-sixth of the O atoms in the perovskite structure, yielding a high intrinsic concentration of O vacancies. The vacancies order at room temperature into an orthorhombic structure, resulting in three crystallographically-distinct O sites (Figure 1.4). The labelling adopted hereafter has O1 anions at the equatorial positions of the octahedra; O2, bridging octahedral and tetrahedral layers; and O3, within the tetrahedral layer. The structure is termed brownmillerite after the original Ca_2FeAlO_5 mineral that contains a

similar arrangement of O vacancies.(Colville and Geller [10])

Hydration of the $Ba_2In_2O_5$ at high temperature results in a tetragonal structure with space group $P4/mbm$ where the intrinsic vacancies of $Ba_2In_2O_5$ in the O3 layer are fully occupied by the water O atoms. One of the water protons (H2) fully occupies the $2c$ positions (O3 layer) while the second proton (H1) partially occupies (0.125) the $16l$ positions (O2 layer) according to a combined X-ray and neutron diffraction analyses (Figure 4.1a).(Jayaraman et al. [3]) Conductivity data for $Ba_2In_2O_4(OH)_2$ was reported by Zhang and Smyth [8] and suggests three regions of protonic conduction corresponding broadly to temperatures below 400°C, between 400°and 925°C, and above 925°C. Zhang and Smyth [8] suggests a Grotthuss (H hopping) or vehicle (OH hopping) mechanism as a means of protonic conductivity, at lower temperatures most likely Grotthuss is dominating while at elevated temperatures a vehicle or a combination of both may occur.

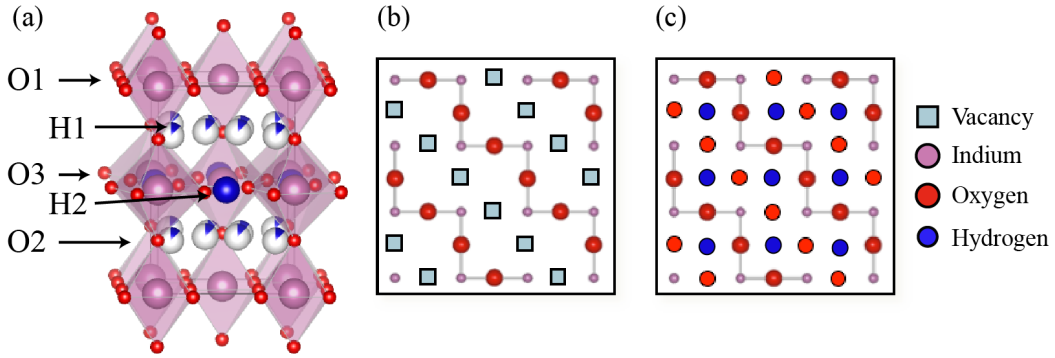

Figure 4.1: (a) Room temperature crystal structure of tetragonal $Ba_2In_2O_4(OH)_2$ in space group $P4/mbm$.([3]) and schematic representations of the O3 layer of (b) $Ba_2In_2O_5$ and (c) $Ba_2In_2O_4(OH)_2$. The interlayer Ba atoms have been omitted for clarity. Sector filling of atoms in (a) denotes partial site occupancies.

A study of $Ba_2In_2O_4(OH)_2$ and of its Ti-doped derivatives (Jayaraman et al. [3]) using ^1H and ^2H solid state NMR experiments under magic angle spinning (MAS) reveal the presence of three distinct proton sites (one distinct resonance and one split resonance), while only two proton sites are anticipated based upon

the tetragonal crystal structure (Figure 4.1a). The further splitting of proton sublattices in the NMR data as compared with the number of crystallographic sites found by neutron diffraction was interpreted as a result of a further ordering of proton sites with respect to the average structure. The authors postulated that this arises from the actual unit cell being much larger than the average unit cell of the $P4/mbm$ space group used in the refinement of the diffraction data, with NMR being sensitive enough to be able to distinguish between variations of different ordering schemes for at least one of the two environments. However, no clear assignments of these three proton resonances were given. Understanding of the moisture uptake and protonic conductive processes in this system is of particular interest as the extremely large number of vacancies in the brownmillerite structure facilitate a level of hydration rarely witnessed in related materials. (Kreuer [4])

Theoretical work done by Islam et al. [40] on $Ba_2In_2O_4(OH)_2$ system reveals the hydration mechanism of $Ba_2In_2O_5$ where oxygen interstitial and Frenkel vacancy sites are involved in the process. Martinez et al. [20] studied the energetics and disorder of protons in the system. In our work we reproduced the study by Martinez et al. [20] and further improve with DFT GIPAW calculations.

The current work examines hydrated $Ba_2In_2O_5$ [i.e. $Ba_2In_2O_4(OH)_2$] using current solid state ^{17}O and ^{1}H NMR spectroscopy techniques, applying high magnetic field strengths which allows for high-resolution solid state NMR spectra of quadrupolar nuclei (such as ^{17}O, spin $I = \frac{5}{2}$) to be obtained. First principles periodic DFT NMR calculations within the gauge-including projector augmented wave (GIPAW) approach (Pickard and Mauri [62]) are also performed, providing a robust interpretation of the experimental spectra assignments. The DFT calculations also provide direct insight into the energetics and structural configurations governing the processes in $Ba_2In_2O_4(OH)_2$ phases. The study of the hydrated phase, $Ba_2In_2O_4(OH)_2$, is then described using solid state NMR spectroscopy supported by DFT and GIPAW calculations. The individual ^{17}O and ^{1}H NMR shifts are assigned to specific proton environments and suggest the existence of three or more types of proton environments at room temperature in the hydrated system.

4.2 Materials and Methods

4.2.1 Experimental

Sample preparation: $Ba_2In_2O_5$ powder was prepared by a solid state route (West [122]) using stoichiometric quantities of $BaCO_3$ (Sigma-Aldrich, $\geq$ 99%) and In_2O_3 (Sigma-Aldrich, 99,99% trace metals basis) which were first ground in a planetary ball mill (Retsch PM100) at 600 rpm for 4 hours. $Ba_2In_2O_5$ was then pelletized, sintered at 1300°C for 24 hours and re-ground by hand, these steps were repeated until a pure phase was obtained as determined by powder X-ray diffraction (Figure 4.2). ^{17}O enriched $Ba_2In_2O_5$ was obtained by heating dry $Ba_2In_2O_5$ (dried at 900°C under vacuum for 12h) in 50% ^{17}O enriched O2 gas (Isotec, 99%, used as received) in a sealed quartz tube at 1000°C for 24 hours.(Ashbrook and Smith [123]) $Ba_2In_2O_4(OH)_2$ was prepared by slow cooling of the dry $Ba_2In_2O_5$ (dried at 400 °C under a flow of dry N2 for 12h) from 350°C to room temperature (at a rate of 0.1°C/min) under a flow of wet N_2 gas. The water vapor pressure corresponds to 2.3 (w/v) % H_2O and was controlled by bubbling the N_2 through water at room temperature.(Schober et al. [155]) ^{17}O enriched $Ba_2In_2O_4(OH)_2$ was produced by heating non-enriched $Ba_2In_2O_4(OH)_2$ under 50% enriched O2 gas (Isotec, 99%, used as received) in a quartz tube, connected to a vacuum line at 1000°C for 24 h. Sufficient water was added to the vacuum line to achieve a vapor pressure of approximately 1atm at 1000°C. Powder X-ray diffraction patterns were obtained on Panalytical Empyrean and Bruker D8-Focus X-ray diffractometers using Cu K_α radiation (λ= 1.5418Å) (Figure 4.2). Thermogravimetric analyses (TGA) were performed on a Mettler Toledo TGA/SDTA851 thermobalance using alumina crucible (Figure 4.3). All measurements were performed under flowing dry nitrogen, with a temperature range of 30°-800°C and at a heating rate of 10°C.min^{-1}. TGA showed that both hydrated and ^{17}O enriched hydrated samples contain 1 mole of water per formula unit, as anticipated. (Figure 4.3)

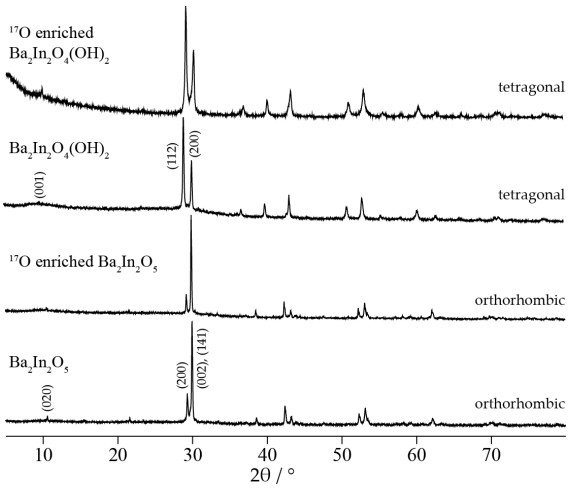

Figure 4.2: Powder X-ray diffraction patterns of $Ba_2In_2O_5$, ^{17}O enriched $Ba_2In_2O_5$, $Ba_2In_2O_4(OH)_2$ and ^{17}O enriched $Ba_2In_2O_4(OH)_2$. The unit cell is given on the right. The broad component in $Ba_2In_2O_4(OH)_2$ observed at low 2θ has been observed previously.([3]) This figure is repeated here from Figure 2.2 for clarity.

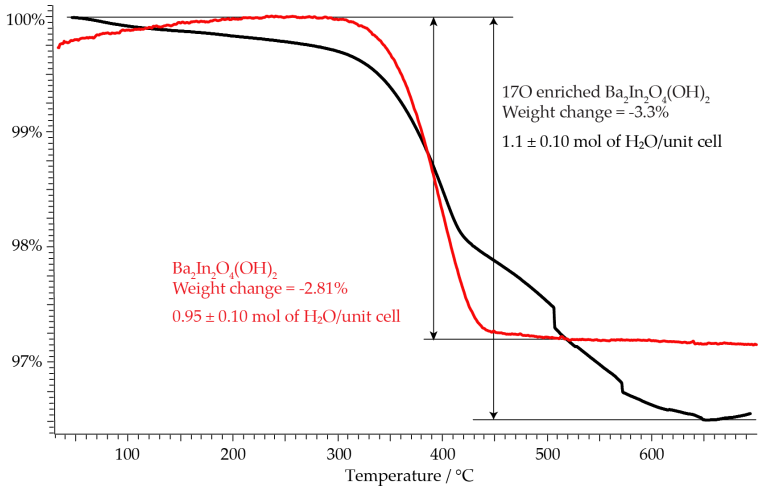

Figure 4.3: Thermogravimetric analysis curve of $Ba_2In_2O_4(OH)_2$ (red) and ^{17}O enriched $Ba_2In_2O_4(OH)_2$ (black). 1 mole of H_2O per 1 mole of $Ba_2In_2O_4(OH)_2$ is lost at around 400°C.

Solid State NMR Spectroscopy: Solid state ^{17}O MAS NMR experiments on $Ba_2In_2O_4(OH)_2$ were performed on a 9.4 T Bruker Avance 400 MHz and on a 16.4 T Bruker Avance III 700 MHz spectrometers using a Bruker 2.5 mm HX probe and a Bruker 3.2 mm HXY (in double resonance mode) probe. Unless otherwise stated, spectra were recorded using a $\sim \pi/2$ pulse length of 1 μs at a RF field amplitude of $\sim$ 80 kHz and a MAS frequency of 30 kHz at 9.4 T, and a $\sim \pi/2$ pulse length of $\sim$1.7 μs at a RF field amplitude of $\sim$50 kHz and a MAS frequency of 20 kHz at 16.4 T. The 3QMAS experiment was performed at 9.4 T with 128 t_1 increments of 1320 scans each. Hard and soft pulses are performed at RF fields of 150 and $\sim$10 kHz, respectively. All ^{17}O NMR data were collected on freshly ^{17}O enriched sample and packed in ZrO_2 rotor. A recycle delay of 10 s was used for all experiments averaging $\sim$6500-30000 scans.

^1H MAS NMR experiments were performed on a 16.4 T Bruker Avance III 700 MHz spectrometer equipped with a Bruker 4 mm HXY probe (used in double resonance mode). One dimensional (1D) spectra were recorded under MAS using a rotor-synchronised spin echo sequence so as to suppress the proton background of the probe. All ^1H spectra were recorded at an RF field amplitude of 100 kHz and a MAS frequency of 12.5 kHz with recycle delays ranging from 4 to 60 s depending on the T_1 relaxation times. Temperature calibration was performed using the ^{207}Pb resonance of $Pb(NO_3)_2$ as a chemical shift thermometer.(Bielecki and Burum [156], Beckmann and Dybowski [157]) The sample temperatures quoted subsequently have all been corrected and have an accuracy of $\pm$ 10°C. Additional fast MAS ^1H NMR experiments were recorded on the same spectrometer with a Bruker 1.3mm HX probe spinning the sample at 60 kHz, using a rotor-synchronised spin echo sequence, an RF field amplitude of 115 kHz and recycle delay of 8 s; and a Bruker 3.2mm HXY probe spinning the sample at 20 kHz, using two dimensional ^1H to ^{17}O hetero-nuclear correlation (2D ^1H-^{17}O HETCOR MAS) (Huo et al. [21], Peng et al. [22], Hartmann and Hahn [23], Schaefer and Stejskal [24]) with a contact time of 40 μs for the cross-polarization (CP) transfer.

^{17}O and ^1H chemical shifts were externally referenced to water at 0.0 and 4.8 ppm respectively at 20°C. NMR data were processed using the Bruker TopSpin 3.0 package (BRUKER [124]), and the MatNMR package (van Beek [125]), the latter running on MatLab. Simulations and deconvolutions were also performed

using the TopSpin 3.0 and the MatNMR packages.

4.2.2 Computational Methods

Energetics and configurations: The first principles solid-state electronic structure calculations used here are similar to those in chapter 2 on the dry material and related studies by Johnston et al. [118], Blanc et al. [119], Buannic et al. [121], Middlemiss et al. [126], Barrow et al. [127], Reader et al. [128] and Mitchell et al. [129], and were all performed within the CASTEP code by Clark et al. [130]. Full structural optimisations (both cell and atomic positions) $Ba_2In_2O_4(OH)_2$ were performed in the absence of any symmetry constraints (i.e. space group $P1$), a plane wave kinetic energy cut-off of 40 Ry (∼53MJ/mol) and a linear spacing of 0.04 $Å^{-1}$ or smaller for the reciprocal space sampling mesh, yielding Monkhorst-Pack meshes of dimension 6x6x4 for the $Ba_4In_4O_8(OH)_4$ supercell. Full representation of all these structures is detailed in the Appendix A.1. The Perdew-Burke-Ernzerhof GGA-type exchange-correlation functional has been used throughout. (Perdew et al. [158]) Convergence of total energy with respect to numerical parameters was estimated at 0.2kJ/mol per atom or better. The optimisation was pursued until energy difference, maximum atomic force, maximum atomic displacement and maximum stress tensor component fell below tolerances of 1×10^{-6}eV, 1×10^{-3}eV$Å^{-1}$, 1×10^{-3}Å and 5×10^{-3}GPa, respectively. The effect of decreasing the tolerances listed above by a further order of magnitude was investigated, yielding only minimal changes in geometry and computed NMR parameters.

NMR Calculations: Fully periodic calculations of NMR parameters within the gauge-including projector augmented wave (GIPAW) method by Pickard and Mauri [62], Yates et al. [91] have been performed using the CASTEP code, including determinants of electric field gradient tensors and associated quadrupolar interaction parameters for ^{17}O sites. (Profeta et al. [94]) The NMR parameters were obtained from a single point calculation within the optimised geometry, differing only from the earlier optimizations in that a larger basis set cut-off of 60 Ry (∼79MJ/mol) was applied. The isotropic shielding was obtained as

$\sigma_{iso} = \frac{1}{3}(\sigma_{xx} + \sigma_{yy} + \sigma_{zz})$, where σ_{xx}, σ_{yy} and σ_{zz} are the principal components of the shielding tensor, ordered such that $|\sigma_{zz} - \sigma_{iso}| \geq |\sigma_{xx} - \sigma_{iso}| \geq |\sigma_{yy} - \sigma_{iso}|$. The chemical shift δ_{iso} is then derived from the computed site shielding σ_{iso} by applying a shielding reference σ_{ref} with the expression $\delta_{iso} = \sigma_{ref} + m\sigma_{iso}$. Both σ_{ref} and m for ^{17}O are obtained from a previous work by Middlemiss et al. [126] which yielded $\sigma_{ref} = 223.70 \pm 3.03$ppm, $m = -0.888 \pm 0.014$ with a mean absolute error (MAE) of 12.1 ppm. Meanwile σ_{ref} and m for ^{1}H are determined from a fit of the results of NMR CASTEP calculations on $Mg(OH)_2$ ($\sigma_{iso} = 30.89ppm$, $\delta_{iso} = 0.5ppm$, Sears et al. [19]) in combination with 55 different proton sites in four separate organic molecules as computed recently by Yates et al. [16], Webber et al. [17] and Sardo et al. [18] yielding $\sigma_{ref} = 28.45 \pm 0.51$ppm, $m = -0.930 \pm 0.020$ with a MAE of 0.29 ppm (Figure 4.4). It is noted that all but one of the proton sites considered in deriving the reference belong to organic molecules, and thus expected some discrepancy between experimental and calculated ^{1}H chemical shifts in $Ba_2In_2O_4(OH)_2$ as discussed below. The chemical shift anisotropy and asymmetry are also computed, defined as $\sigma_{aniso} = \sigma_{zz} - \frac{1}{2}(\sigma_{xx} - \sigma_{yy})$ and $\eta_{CS} = \frac{(\sigma_{yy} - \sigma_{xx})}{(\sigma_{zz} - \sigma_{iso})}$, respectively. The quadrupole coupling constant for ^{17}O sites is obtained as $C_Q = eQV_{zz}/h$; and the asymmetry, as $\eta_Q = \frac{(V_{xx} - V_{yy})}{V_{zz}}$; where an ordering $|V_{zz}| \geq |V_{yy}| \geq |V_{xx}|$ of the principal components of the traceless electric field gradient tensor is assumed. The experimental value Q = -0.02558 barns has been used for the ^{17}O nuclear electric quadrupole moment.(Pyykkö [95]) Unless otherwise specified, all the corresponding simulated ^{17}O NMR spectra were obtained by simulation of each individual O site with SIMPSON code by Bak et al. [131], which were then summed together to result in the final spectra, as expected from this method dipolar interactions are not present in the final spectra. No attempts were made to include ^{17}O - ^{1}H dipolar couplings because the spectra were acquired under MAS. NMR parameters of $Ba_2In_2O_4(OH)_2$ were calculated from structures derived from the experimental neutron diffraction model by Jayaraman et al. [3] that were also studied for their energetics and disorder of protons by Martinez et al. [20] as described below.

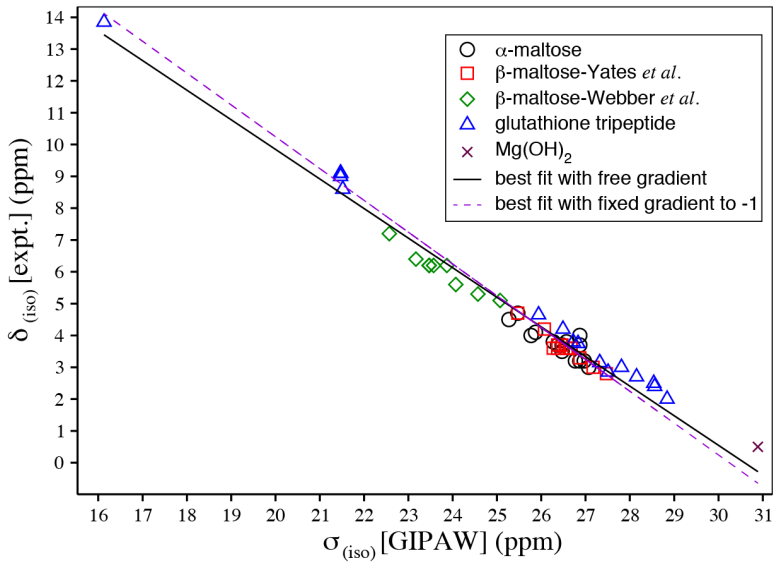

Figure 4.4: Plot of experimental isotropic shift, δ_{iso}, against computed isotropic shielding, σ_{iso}, for ^{1}H sites. Black circles denote α-maltose data;(Yates et al. [16]) red squares β-maltose data;(Yates et al. [16]) green diamond β-maltose data;(Webber et al. [17]) blue triangles glutathione tripeptide;(Sardo et al. [18]) and purple cross $Mg(OH)_2$ using the present calculation for σ_{iso} and the literature for δ_{iso} by Sears et al. [19]. Black line denotes the best fit with free gradient (corresponding to $\delta_{iso} = \sigma_{ref} + m\sigma_{iso}$ with $\sigma_{ref} = 28.45 \pm 0.51$ppm, $m = -0.930 \pm 0.020$ with a MAE of 0.29 ppm) and the dashed purple line, a fit with gradient fixed to -1 (fitted to $\delta_{iso} = \sigma_{ref} - \sigma_{iso}$ with $\sigma_{ref} = 30.24 \pm 0.32$ppm).

4.3 Results and Discussion

4.3.1 Energetics and configurations

The structural optimization of $Ba_2In_2O_4(OH)_2$ was performed with the same approach as for $Ba_2In_2O_5$ as used in the chapter 2 taking the $P4/mbm$ structure of Jayaraman et al. [3] as a starting point. (Figure 4.5a, O1 and O2 labels of Jayaraman et al. [3] are switched in order to match the notation used for pure $Ba_2In_2O_5$ previously) and cell lengths given by $\sqrt{2}a_p \times \sqrt{2}a_p \times 2a_p$ (where a_p is the notional perovskite unit cell length).(Fischer et al. [48], Jayaraman et al. [159]) Fourteen arrangements of protons are considered, with full occupancy of the O3 layers ($2c$ site), various proton configurations in the O2 layers ($16l$ site with fractional occupancy of $\frac{1}{8}$) and the O1 layer (which was not observed by Jayaraman et al. [3]), resulting in configurations similar to those appearing in the study by Martinez et al. [20] (Figure 4.5b and Table 4.1), and ranked in terms of calculated total energies (Figure 4.5b). As shown also by Martinez et al. [20], all configurations undergo strong relaxation from average positions suggested by Jayaraman et al. [3]. The O2 layer protons move off the $16l$ positions suggested from neutron diffraction[3] into the $'32y'$ positions, maintaining the nomenclature used previously used by Martinez et al. [20]. The computationally relaxed ground state forms alternating semi-occupied; fully-occupied; non-occupied; non-occupied layers of $\cdots O2 - O3 - O2 - O1 \cdots$ oxygens, respectively (Figure 4.5b). Simply, we can imagine that O3 layer O vacancies of the $Ba_2In_2O_5$ are fully occupied by an O and one of the protons of H_2O (Figure 4.1b and c), while the second proton of the water is placed into one of the two nearby O2 layers. However, only one of the O2 layers is protonated, while the other stays empty. (Figure 4.5b) The optimized In-O3-In bond angles are significantly different from In-O1-In and In-O2-In, placing O3 oxygen atoms in a significantly different electronic environment. (Table 4.1) Moreover, the bond length asymmetry of In-O2-In is substantial and may complicate the assignment of ^{17}O NMR spectra for the $Ba_2In_2O_4(OH)_2$. (Table 4.1) It is also clear from the optimized structures that hydrogen bonding constitutes the main interaction driving the formation of a number of distinct chemical environments for both protons and oxygens.

Table 4.1: Cell constants (Å, °), In-O and O-H bond distances (Å) and In-O-In and $O-H\cdots H$ bond angles (°) for O1, O2 and O3 environments obtained from optimizations of the initial perturbed P1 symmetry $Ba_4In_4O_8(HO)_4$ cells, in the lowest energy I, J, K, L configurations [Figure 4.6], as compared with corresponding experimental and calculated literature values. Means and standard deviations in the values are shown. * Note that the O1 and O2 labels of Jayaraman et al. [3] structure are switched in order to match the earlier notation used for the $Ba_2In_2O_5$.

		Optimized-I structure (present calculation, P1)	Optimized-J structure (present calculation, P1)	Optimized-K structure (present calculation, P1)	Optimized-L structure (present calculation, P1)	Average of I, J, K and L structures	Computational by Martinez et al. [20]	Experimental by Jayaraman et al. [3] ($P4/mbm$)
Cell	(Å, °)	a =5.975, b = 5.992, c = 9.308 α = 93.3, β =93.1, γ = 90.3	a = 5.951, b = 6.029, c = 9.226 α = 87.9, β = 90.2, γ = 91.0	a = 5.929, b = 5.984, c = 9.324 α = 93.7, β = 90.0, γ = 90.0	a = 5.966, b = 5.979, c = 9.247 α = 89.7, β = 90.0, γ = 92.1	a = 5.955 (sd 0.017), b = 5.996 (sd 0.02), c = 9.276 (sd 0.041) α = 91.2 (sd 2.4), β = 90.8 (sd 1.3), γ = 90.8 (sd 0.8)	-	a = 5.915, b = 5.915, c = 8.999, $\alpha = \beta = \gamma = 90$
In-O1-In	distances (Å)	2.120 (sd 0.006) 2.132 (sd 0.008)	2.138 (sd 0.014) 2.162 (sd 0.008)	2.112 (sd 0.006) 2.121 (sd 0.001)	2.160 (sd 0.023) 2.162 (sd 0.024)	2.133 (sd 0.028) 2.144 (sd 0.026)	- -	* 2.092 * 2.092
	angle (°)	169.1 (sd 2.5)	164.0 (sd 11.0)	168.5 (sd 1.3)	160.4 (sd 14.8)	165.5 (sd 18.7)	-	178.4
In-O2-In	distances (Å)	2.274 (sd 0.162) 2.411 (sd 0.231)	2.251 (sd 0.138) 2.391 (sd 0.235)	2.299 (sd 0.183) 2.378 (sd 0.172)	2.213 (sd 0.076) 2.428 (sd 0.250)	2.259 (sd 0.290) 2.402 (sd 0.448)	- -	* 2.192 * 2.307
	angle (°)	173.9 (sd 4.1)	169.6 (sd 5.9)	175.6 (sd 3.1)	170.9 (sd 1.7)	172.5 (sd 8.0)	-	180.0
In-O3-In	distances (Å)	2.231 (sd 0.067) 2.293 (sd 0.108)	2.245 (sd 0.085) 2.297 (sd 0.128)	2.250 (sd 0.053) 2.274 (sd 0.064)	2.253 (sd 0.080) 2.262 (sd 0.087)	2.244 (sd 0.145) 2.282 (sd 0.199)	- -	2.201 2.201
	angle (°)	139.0 (sd 4.4)	138.1 (sd 1.2)	137.5 (sd 3.7)	139.2 (sd 6.0)	138.4 (sd 8.4)	-	143.6
O3-H$\cdots$O	distances (Å)	1.011 (sd 0.005) 1.750 (sd 0.035)	1.013 (sd 0.001) 1.720 (sd 0.020)	1.022 (sd 0.000) 1.676 (sd 0.000)	1.018 (sd 0.002) 1.680 (sd 0.037)	1.016 (sd 0.006) 1.707 (sd 0.055)	- 1.7	1.404 1.404
	angle (°)	173.3 (sd 5.3)	175.3 (sd 0.2)	177.8 (sd 0.0)	176.7 (sd 0.5)	175.8 (sd 5.3)	-	180.0
O2-H$\cdots$O	distances (Å)	0.993 (sd 0.003) 1.819 (sd 0.005)	0.983 (sd 0.001) 1.969 (sd 0.005)	0.995 (sd 0.000) 1.844 (sd 0.000)	0.982 (sd 0.001) 1.957 (sd 0.014)	0.988 (sd 0.003) 1.897 (sd 0.016)	* 1.00 1.90	* 0.991 (sd 0.000) 2.542 (sd 0.051)
	angle (°)	153.5 (sd 1.8)	151.0 (sd 1.7)	154.5 (sd 0.0)	150.0 (sd 1.7)	152.2 (sd 3.0)	-	116.4 (sd 4.2)

Three different types of configurations were considered within the $Ba_4In_4O_8(OH)_4$ supercell with two out of four protons always placed in the O3 layer and the other two, each in a different O2 layer [two-layer hydroxide (TLH), configuration A-H], or in the same O2 layer [one-layer hydroxide (OLH), configuration I-L] or having one water molecule (two protons attached to one oxygen) per layer [one-layer water (OLW), configuration M-N]. Arrangements where the protons are located within one O2 layer (OLH, ground state structure $E_{ref} = 0 - 8.8$kJ/mol) are systematically lower in energy than the OLW ($E_{ref} = 17.8$ & 35.8kJ/mol) and TLH (Eref $= 10.2 - 48.8$kJ/mol) arrangements. Note however, that all OLW configurations are highly unstable, relaxing to OLH configurations. The thermal energy k_BT at a typical hydration synthesis temperature, assuming non-equilibrium cooling, allows for configurations with up to ∼10kJ/mol to be present at room temperature. This assumption is used to select I, J, K and L structures (all OLH) from the rest of configurations. The ground state structure is structure I where the protons in the O2 layer point towards two different O3 acceptors, a structure similar to the first excited structure of Martinez et al. [20]. Note that this previous study suggested our configuration L as the ground state structure where the O2 layer protons pointing towards O1 oxygen site. (Figure 4.5b and 4.6) The fact that our study and the Martinez et al. [20]s study disagree on the energy ordering of structures at the ∼6 kJ/mol level suggests that DFT cannot be regarded as yielding energies any more accurately that to within ∼ 10 kJ/mol.

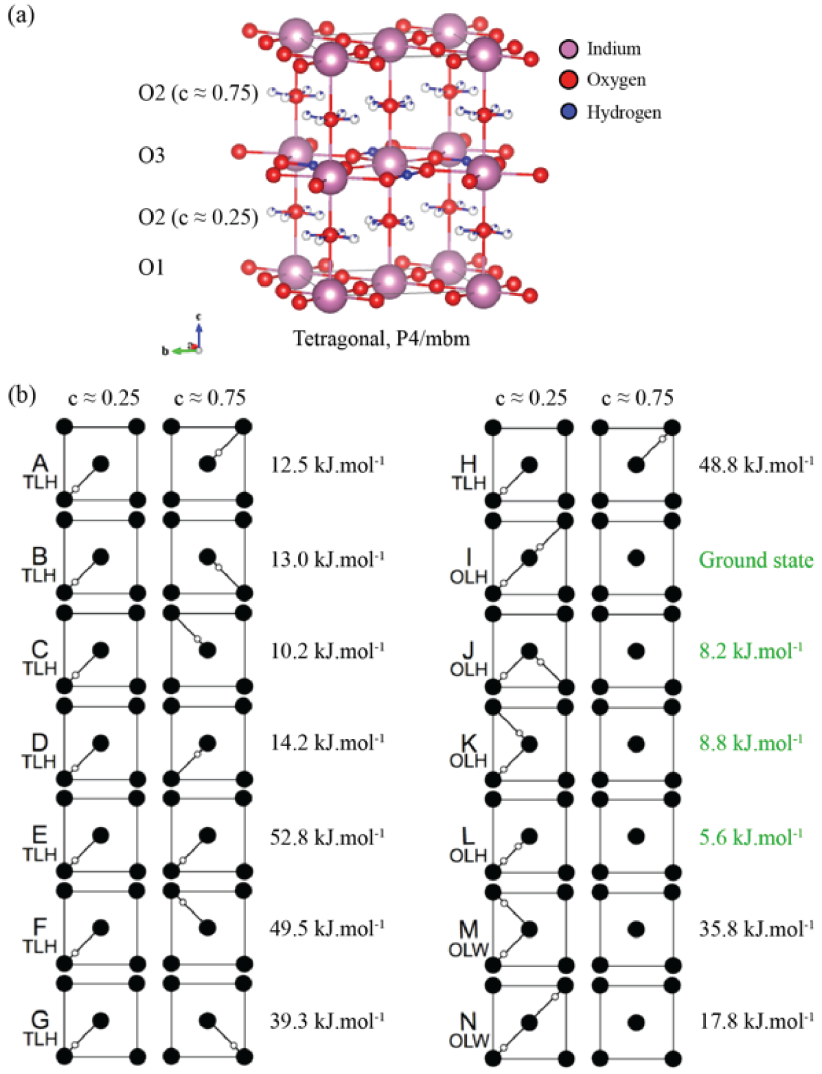

Figure 4.5: (a) Room temperature crystal structure of tetragonal $Ba_2In_2O_4(OH)_2$ in space group $P4/mbm$[3] showing full occupancy of the protons in the O3 layer ($2c$ site) and partial occupancy in the O2 layer ($16l$ site). The interlayer Ba cations have been omitted for clarity. (b) Schematic representation of the 14 calculated proton configurations differing in terms of the arrangement of protons in the O2 layers ($16l$ site). Full and empty circles represent the O atoms and protons, respectively. Eight configurations (A-H) correspond to two-layer hydroxyl (TLH) forms; Four configurations (I-L) to one-layer hydroxyl (OLH) forms; and two configurations (M-N), to one-layer water (OLW) forms. Protons were placed initially in the $16l$ positions with fractional occupancy of $\frac{1}{8}$ determined by neutron diffraction,[3] and optimized into the $32y$ positions suggested by the previous first principles calculations by Martinez et al. [20]. The calculated energy per unit cell of each configuration relative to the ground state structure I is also shown.

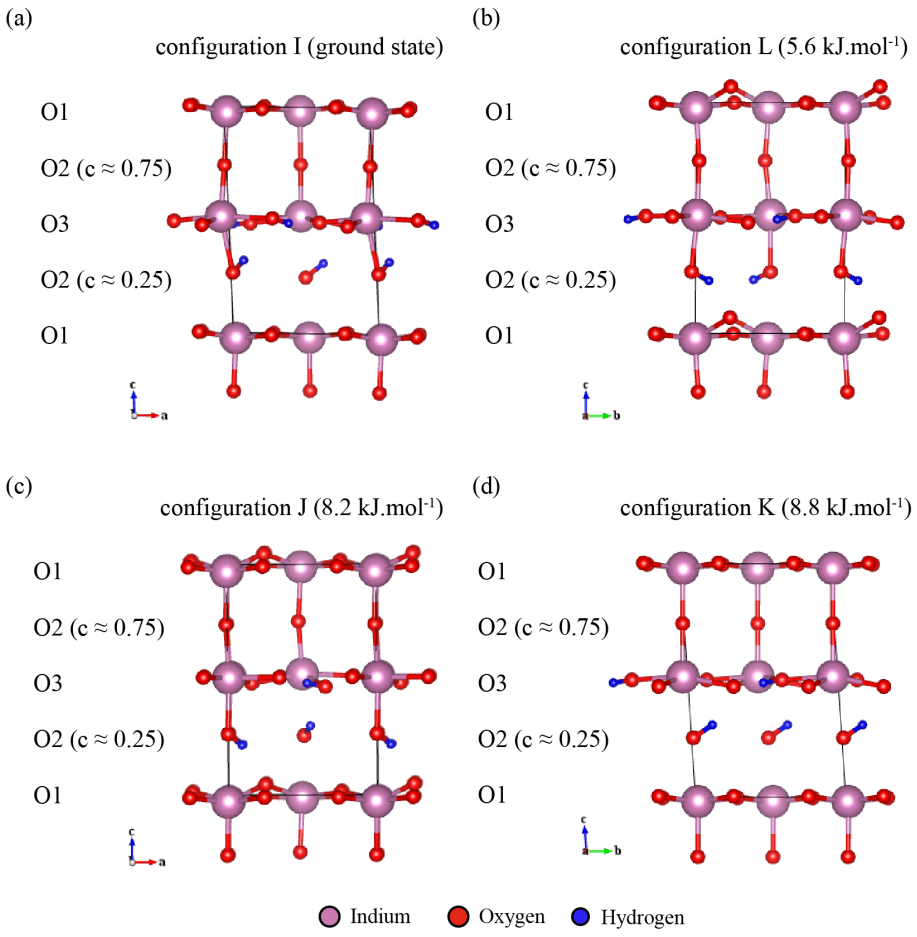

Figure 4.6: DFT Optimized geometries of (a) configuration I (ground state), (b) configuration L, (c) configuration J and (d) configuration K showing the O3 and O2 (c $\approx$ 0.25) layer protons. The interlayer Ba atoms have been omitted for clarity.

4.3.2 Experiments and DFT GIPAW results

X-ray powder diffraction pattern of $Ba_2In_2O_4(OH)_2$ samples and the ^{17}O enriched counterpart prepared in this study are consistent with previous reports.(Jayaraman et al. [3]) (Figure 4.2) and indicate that the structures are tetragonal in $P4/mbm$ (Jayaraman et al. [3]) symmetry.

The one-dimensional ^{17}O MAS NMR spectrum of ^{17}O enriched $Ba_2In_2O_4(OH)_2$ obtained at 9.4 T under conditions where lineshape distortion is minimal (i.e. with short pulse length) (Smith and van Eck [15]) shows a complicated pattern characteristic of multiple overlapping ^{17}O sites (Figure 4.7). Resolution of theses sites was performed with a ^{17}O 3QMAS experiment and clearly shows four different resonances (Figure 4.8) satisfactorily fitted to the NMR parameters given in Table 4.2. Fitting of the 1D ^{17}O MAS NMR spectra with these parameters reveals a 4:1:6:4 ratio of intensities (going from high to low shift) (Figure 4.7). The low shift O sites at 97 ppm are not totally resolved in the 3QMAS experiment due to smearing of the nearby site (fit of this site involves exclusion of high shift region in 3QMAS (Figure 4.8)), but the total fit of Figure 4.7 shows that the lineshape is well reproduced by the parameters given in Table 4.2. The ^{17}O signals in the 3QMAS show a broadening along the +1 direction (positive slope, diagonal) attributed to a distribution of chemical shifts and disorder in the position of high frequency oxygen atoms, such as O1 and proton acceptor O2 and O3 sites deduced from DFT calculations.

The calculations support the assignment of the experimental NMR spectrum discussed above with slight differences in chemical shifts. (Figure 4.9, Table 4.2) The deviation from experimental values can be accommodated under the error due to smearing of sites in 3QMAS experiments. Averaging over the chemical shifts for each chemically distinct O site within the four low energy structures leads to two types of O1 (O1 and acceptor O1), two types of O2 (O2 and donor O2) and three types of O3 (donor O3 and two distinct types of acceptor O3) sites (Table 4.2 & Figure 4.9). Peak intensity ratio of 14:2:19:13 (normalized to 7:1:10:7, going from high to low frequency) can be derived from calculations assuming equal contribution from all four low energy configurations, comparable to 4:1:6:4 ratio from experiments as described above. The high δ_{iso} resonance

at approximately 177ppm with a relative weight of 14 arises due to the fourteen combined non-acceptor O1 sites; the other high resonance at 186ppm with a relative weight of 2, from the two acceptor O1 sites; the next resonance with a relative weight of 19 at an average shift of 152ppm from the eight O2, eight O3 and three donor O3 sites; and finally the lowest resonance with relative weight of 13 at an average shift of 106ppm from the eight donor O2 and five donor O3 sites, all corresponding to the 48 O sites anticipated in the four $Ba_4In_4O_8(OH)_4$ configurations (Figure 4.9 and Table 4.2). The calculations provide relatively similar C_Q- and η_Q-values for the four sites with C_Q-values between 4.4MHz and 6.4MHz and two major ranges of η_Q-values: those for non-donor O sites falling at around 0.2, while those for donor O sites lie at approximately 0.7. In summary, the present first principles calculations support the assignment of the ^{17}O MAS-NMR spectrum of $Ba_2In_2O_4(OH)_2$ presented above, yielding chemical shifts and quadrupolar parameters in reasonable agreement with the experimental trends (Figure 4.9b).

The ^{17}O GIPAW calculated isotropic chemical shift δ_{iso} of $Ba_2In_2O_4(OH)_2$ are given in Table 4.2 and cover a wide range of values for a given O sublattice site (Figure 4.9). The corresponding simulated ^{17}O MAS NMR spectra is compared with the experimental data of ^{17}O enriched $Ba_2In_2O_4(OH)_2$ (Figure 4.9a and b) from which a very good agreement could be observed.

The room temperature ^1H MAS NMR spectrum of $Ba_2In_2O_4(OH)_2$ obtained at 16.4 T clearly shows three distinct proton sites at 7.3, 3.3 and 1.7 ppm in a 2:1:1 ratio of intensities (Figure 4.10), corresponding to ^1H in the O3 layers and to two types of protons in the O2 layers (vide supra, first principles calculations of $Ba_2In_2O_4(OH)_2$). Similar ^1H NMR spectra have been reported by Jayaraman et al. [3] although no straightforward assignment was given at the time as that data apparently contradicted the neutron diffraction finding of two distinct proton sublatices. The ^1H spectra is fairly broad, and we assign this to inhomogeneous broadening (i.e. a chemical shift distribution) rather than to strong homogeneous dipolar interactions between protons, as similar ^1H linewidths were obtained in spectra acquired under fast MAS conditions (Figure 4.11). (Lesage [160])

Proton dynamics are an important topic in materials presenting proton conductivity, as in the present hydrated phase. High temperature ^1H solid state

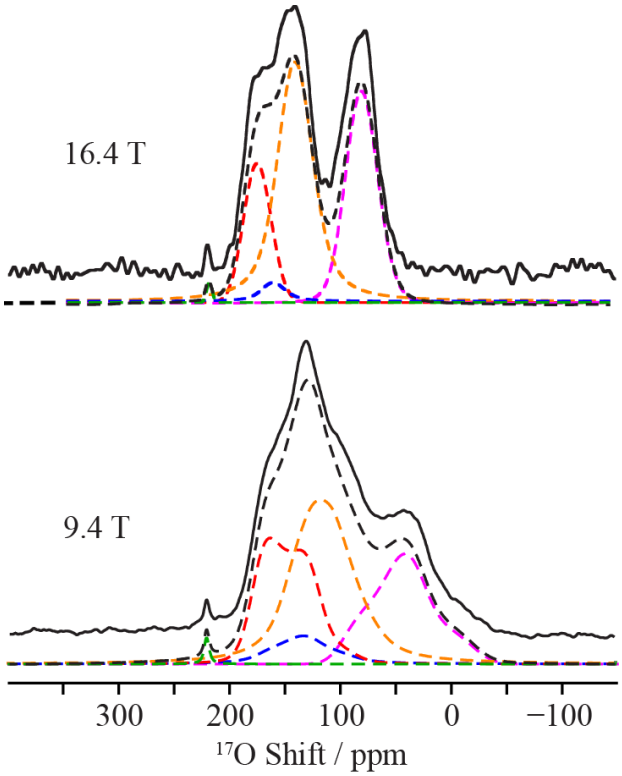

Figure 4.7: ^{17}O MAS NMR spectra of ^{17}O enriched $Ba_2In_2O_4(OH)_2$ obtained at 9.4 T and 16.4 T. Experimental spectra are shown with full lines and total best-fit simulations in black dashed lines. The individual site components are shown in dashed lines in red (site A: O1), blue (site B: acceptor O1), orange (site C: combination of acceptor O2 and acceptor O3) and purple (site D: donor O2 and donor O3) and green O site due to hydration (see Table 4.2). Assignments to O sites are achieved by DFT calculation (see Figure 4.9).

Table 4.2: Experimental and calculated ^{1}H & ^{17}O isotropic shift δ_1 (ppm); isotropic chemical shift, δ_{iso} (ppm); quadrupole coupling constant, C_Q (MHz); and quadrupole asymmetry η_Q for $Ba_2In_2O_4(OH)_2$. Standard deviations are also given for the calculated parameters, deviations of quadrupolar parameters are less than 0.01.

Structure	Nucleus	Environment	δ_1 (ppm)	δ_{iso} (ppm)	C_Q (MHz)	η_Q^b	N
		Experimental[a]					
$Ba_2In_2O_4(OH)_2$	^{17}O	O-Site A (O1) *	140	188(4)	4.5(2)	0.0(1)	0.25
	^{17}O	O-Site B (H-acc. O1) *	174	173(4)	4.1(2)	0.7(1)	0.0625
	^{17}O	O-Site C (H-acc. O2&O3) *	192	152(4)	4.2(2)	0.5(1)	0.375
	^{17}O	O-Site D (H-donor O2&O3) *	207	97(4)	4.8(2)	0.7(1)	0.25
	^{17}O	O-Site E (no match from models)	-	223(4)	1.0(2)	0.0(1)	0.0625
	^{1}H	H-Site A (H2, O3 plane) *	-	7.3(1)	-	-	0.5
	^{1}H	H-Site B (H1, O2 plane I,K) *	-	3.3(1)	-	-	0.25
	^{1}H	H-Site C (H1, O2 plane J,L) *	-	1.7(1)	-	-	0.25
		Calculated[b]					
I	^{17}O	O1	-	170.4 (sd 7.0)	-5.0	0.2	0.33
	^{17}O	donor O2	-	114.4 (sd 3.3)	-6.0	0.8	0.167
	^{17}O	O2	-	159.6 (sd 0.7)	-5.3	0.1	0.167
	^{17}O	donor O3	-	94.5 (sd 1.0)	5.3	0.8	0.167
	^{17}O	acceptor O3	-	156.4 (sd 12.4)	-4.3	0.5	0.167
	^{1}H	H2, O3 plane	-	8.5 (sd 0.7)	-	-	0.5
	^{1}H	H1, O2 plane	-	5.3 (sd 0.1)	-	-	0.5
J	^{17}O	O1	-	185.1 (sd 7.1)	-5.2	0.2	0.25
	^{17}O	acceptor O1	-	175.4 (sd 0.0)	-4.4	0.8	0.083
	^{17}O	donor O2	-	103.6 (sd 6.4)	-6.9	0.6	0.167
	^{17}O	O2	-	169.1 (sd 6.2)	-5.4	0.1	0.167
	^{17}O	donor O3	-	107.0 (sd 2.0)	5.1	0.9	0.167
	^{17}O	acceptor O3	-	158.5 (sd 0.3)	-4.4	0.7	0.167
	^{1}H	H2, O3 plane	-	8.8 (sd 0.3)	-	-	0.5
	^{1}H	H1, O2 plane	-	4.0 (sd 0.2)	-	-	0.5
K	^{17}O	O1	-	168.5 (sd 1.1)	-4.9	0.2	0.33
	^{17}O	donor O2	-	117.1 (sd 0.0)	-6.2	0.7	0.167
	^{17}O	O2	-	166.5 (sd 0.0)	-5.3	0.0	0.167
	^{17}O	donor O3	-	103.5 (sd 0.0)	5.7	0.6	0.167
	^{17}O	acceptor O3	-	151.9 (sd 0.0)	-3.8	0.45	0.167
	^{1}H	H2, O3 plane	-	9.7 (sd 0.0)	-	-	0.5
	^{1}H	H1, O2 plane	-	5.1 (sd 0.0)	-	-	0.5
L	^{17}O	O1	-	188.6 (sd 12.0)	-5.4	0.2	0.25
	^{17}O	aceptor O1	-	196.9 (sd 0.0)	4.5	0.7	0.083
	^{17}O	donor O2	-	105.1 (sd 0.8)	-6.8	0.6	0.167
	^{17}O	O2	-	170.8 (sd 3.5)	-5.5	0.1	0.167
	^{17}O	donor O3	-	98.8 (sd 7.5)	5.4	0.8	0.167
	^{17}O	acceptor O3	-	154.0 (sd 10.3)	-4.0	0.8	0.167
	^{1}H	H2, O3 plane	-	9.5 (sd 0.4)	-	-	0.5
	^{1}H	H1, O2 plane	-	3.8 (sd 0.1)	-	-	0.5

[a] Obtained from the 3QMAS and ^{1}H-^{17}O HETCOR experiments. δ_{iso} was determined from the center of gravity of each peak in F2 (δ_2) and F1 (δ_1) as $\delta_{iso} = (17 \times \delta_1 + 10 \times \delta_2)/27$, and C_Q from the fit of the δ_2 cross-sections through the ridge lineshapes. [b] Obtained from the averaged DFT calculated NMR parameters of the four low energy structures I, J, K and L. * denotes most plausible O and hydrogen environments from four hydrated models. [c] Molar fraction of the site in the structure specified.

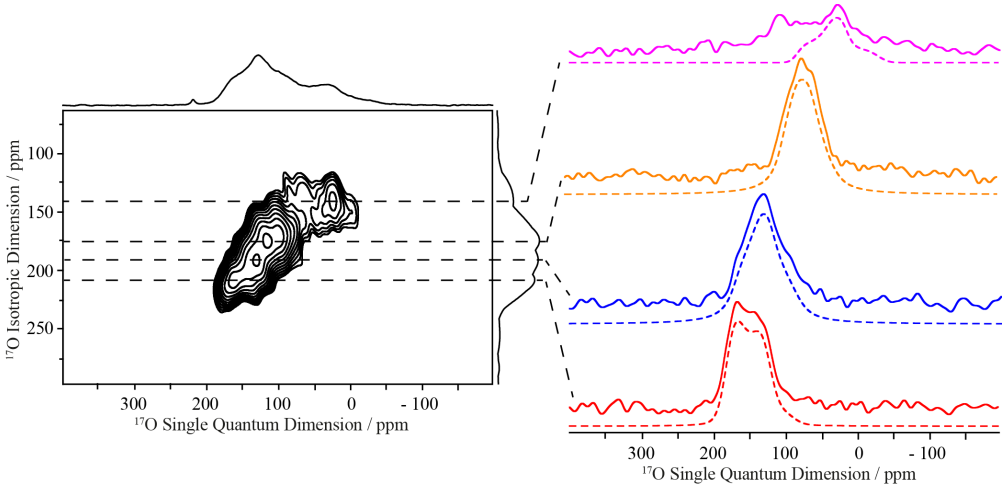

Figure 4.8: Two-dimensional ^{17}O 3QMAS spectrum of ^{17}O enriched $Ba_2In_2O_4(OH)_2$ obtained at 9.4 T. Right: experimental cross sections (full lines) obtained at $\delta_1 = 140$ (purple), 174 (orange), 192 (blue) and 207 (red) ppm along with best-fit simulations (dashed lines) using the parameters given in Table 4.2. Discrepancy at the $\delta_1 = 140$ (purple) is due to smearing of other environments and explained in the main text.

MAS NMR experiments up to 195 °C demonstrate the dynamics of all three proton sites in $Ba_2In_2O_4(OH)_2$, and show that the resonances completely coalesce at around 150°C, yielding a single site with an isotropic chemical shift of 4.4 ppm. Such coalescence process occurs when the proton jump frequency rate k equals $\frac{\pi}{\sqrt{2}}\Delta\nu$ (where $\Delta\nu$ is the frequency separation between the peaks) yielding, k $\sim$ 2.2 kHz for the H environments of 1.7ppm and 3.3ppm, and k $\sim$ 7kHz for the H environments of 7.3ppm and 2.5ppm (second being the coalescence of 1.7ppm and 3.3ppm). As the temperature is increased further, the peak height of the new resonance increases, and its line width narrows, both due to an increase in proton motion. This clearly indicates that all protons contribute to the conductivity, as would be anticipated for a good protonic conductor.

The two-dimensional NOESY NMR experiment correlates sites that are exchanging on the timescale of the mixing times. Such exchanges manifest itself in the presence of cross peaks, situated off positive slope diagonal of ^{1}H vs. ^{1}H chemical shifts. At 42°C, cross peaks between the two distinct protons in the O2

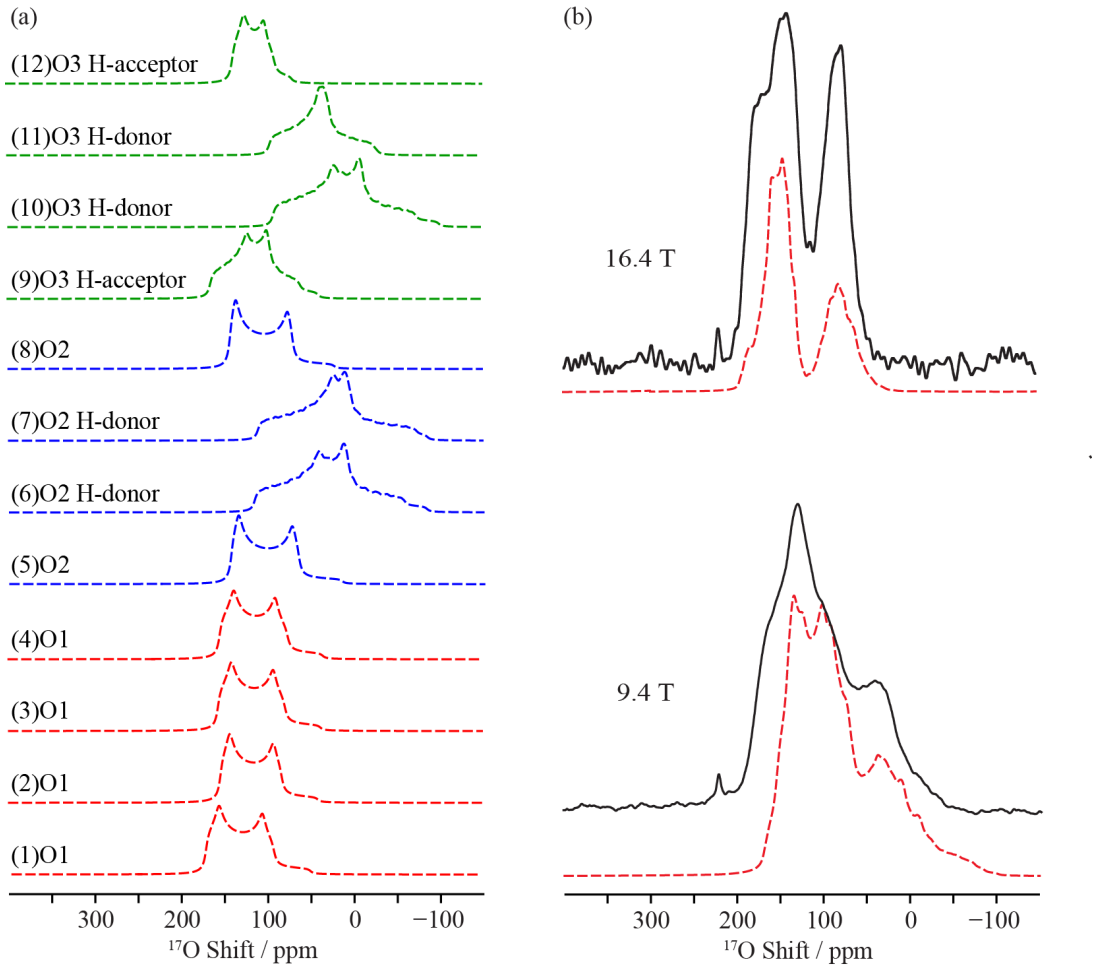

Figure 4.9: (a) Simulation of the GIPAW calculated ^{17}O NMR spectra of the 12 sublattice O sites of the lowest energy structure I of optimized $Ba_2In_2O_4(OH)_2$. All the spectra were simulated at 9.4 T. (b) Comparison of the experimental ^{17}O NMR spectra of ^{17}O enriched $Ba_2In_2O_4(OH)_2$ and the sum of the simulation of the GIPAW calculated ^{17}O NMR spectra (dashed red lines) of all O sites of the four lower energy structures (I, J, K and L) of optimized $Ba_2In_2O_4(OH)_2$ at two magnetic field strengths.

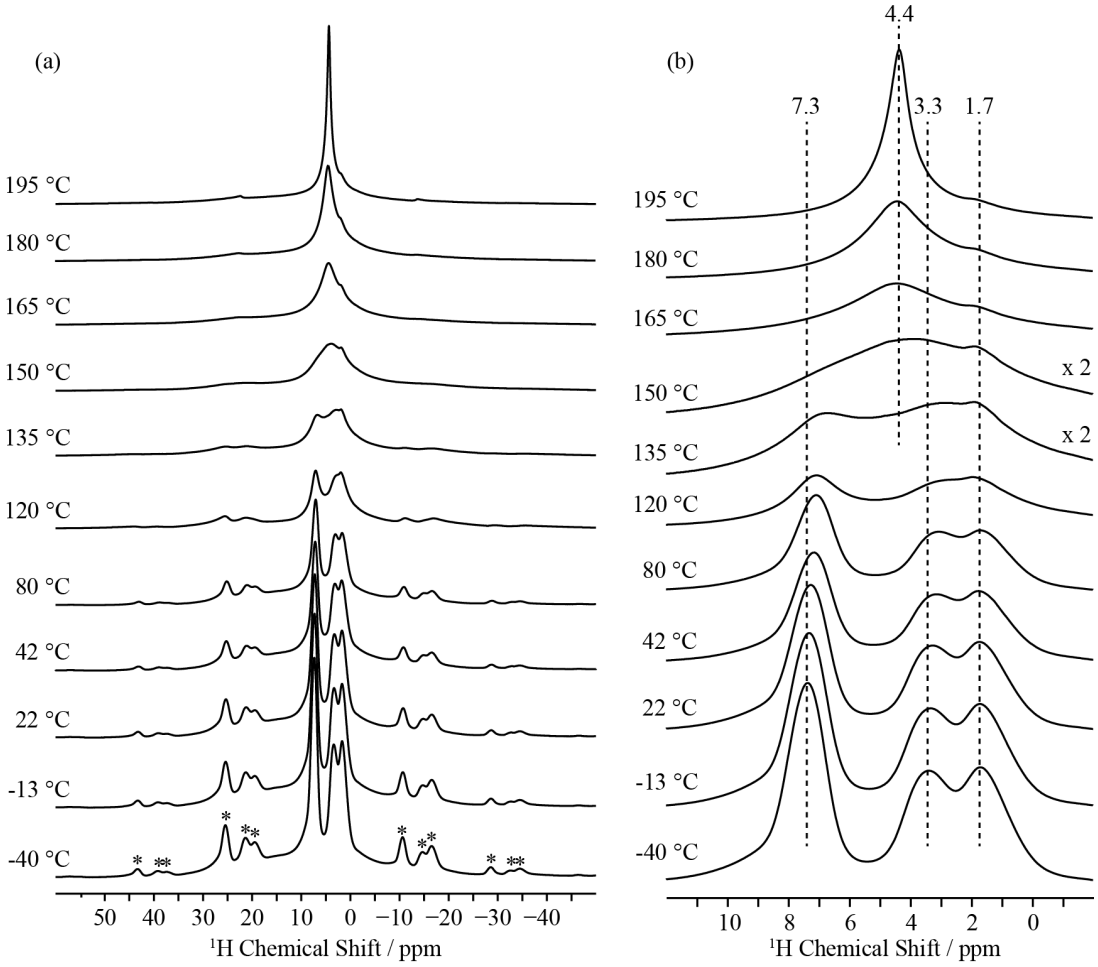

Figure 4.10: Variable temperature ^{1}H MAS NMR spectra of $Ba_2In_2O_4(OH)_2$ obtained at 16.4 T. (a) Full spectral width showing the isotropic region and the spinning side bands manifold marked with asterisks. (b) Magnified view highlighting the two sites 1.7 & 3.3ppm coalescence and complete coalescence of ^{1}H sites above 150°C.

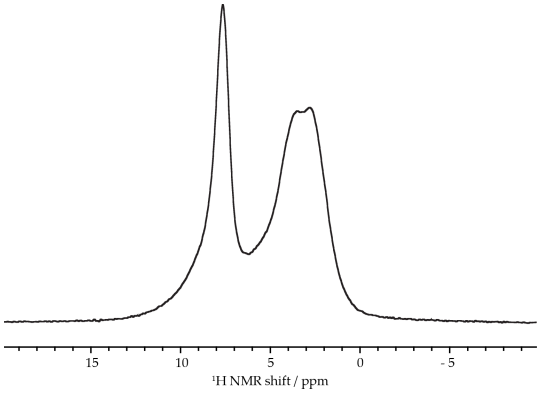

Figure 4.11: ^{1}H MAS NMR spectrum of ^{17}O enriched $Ba_2In_2O_4(OH)_2$ obtained at 16.4 T and under MAS frequency rate of 60 kHz. The sample temperature due to mechanical friction of the rotor was determined to be approximately 80°C, temperature at which the high field proton at $\sim$ 3ppm starts to coalesce (Figure 4.10).

layer (sites at 1.7 and 3.3 ppm) are observed at a mixing time of 1 ms, indicating that these sites belong to the same crystallographic phase and exchange at a rate of 1 kHz. Longer mixing times reveal that the proton in the O3 layer (at 7.3 ppm) also contributes to the exchange but at a much lower rate. Increase in temperature to 80°C leads, as expected, to faster exchange between protons in the O2 layer, as indicated by the presence of cross peaks at short mixing time of 0.1 ms. Meanwhile, at a temperature of 150°C, all protons exchange rapidly at a rate faster than 10 kHz, in agreement with the variable temperature ^{1}H spectra discussed above (Figure 4.10). (Figure 4.12)

The ^{1}H-^{17}O HETCOR NMR (Huo et al. [21], Peng et al. [22], Hartmann and Hahn [23], Schaefer and Stejskal [24]) experiments shown in Figure 4.13 indicate the strong correlation between protons and the lower frequency shift of ^{17}O. Putting this information onto the previous ^{17}O NMR experiments we can see that the lower frequency shift of ^{17}O NMR is due to the proton donating oxygens with short O-H bond distances.

To assign the experimental ^{1}H MAS NMR spectrum of $Ba_2In_2O_4(OH)_2$ presented in Figure 4.10, we computed the ^{1}H site shielding tensors in the proton arrangements discussed above (Table 4.2). Concentrating on parameters obtained

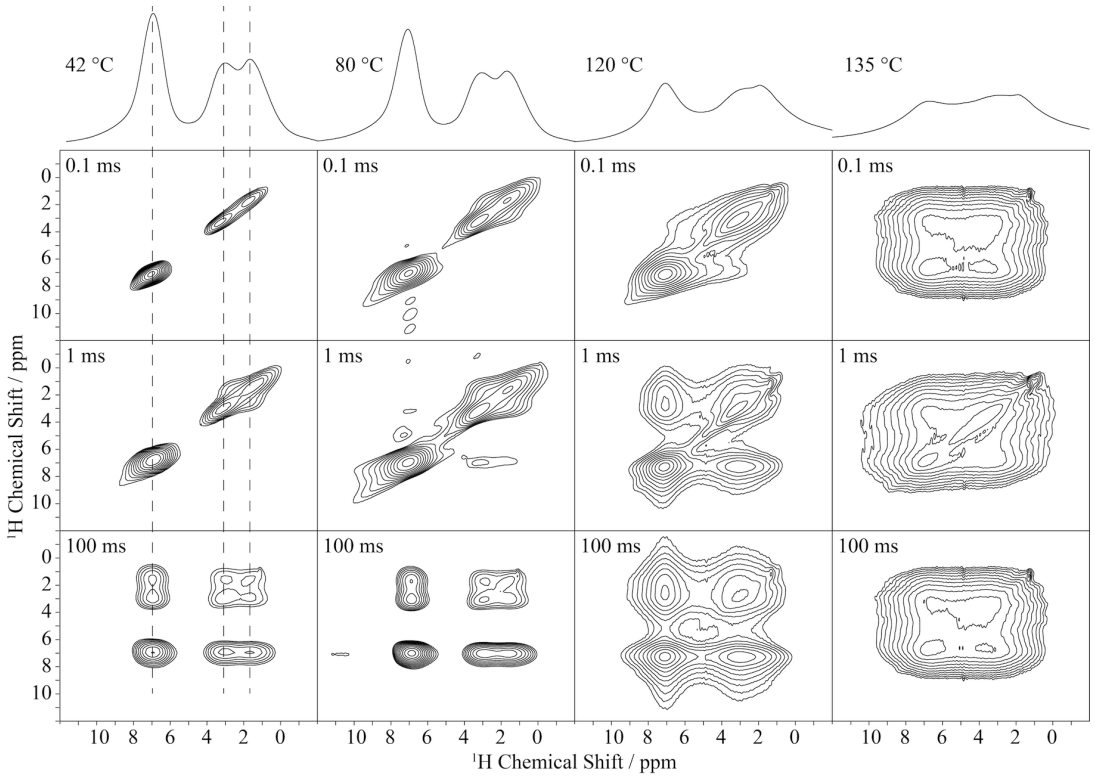

Figure 4.12: Variable temperature two-dimensional ^{1}H NOESY experiments as a function of mixing time. Only the isotropic region is shown. The 1D spectra shown above the 2D plots are the single pulse ^{1}H spectra shown in Figure 4.10.

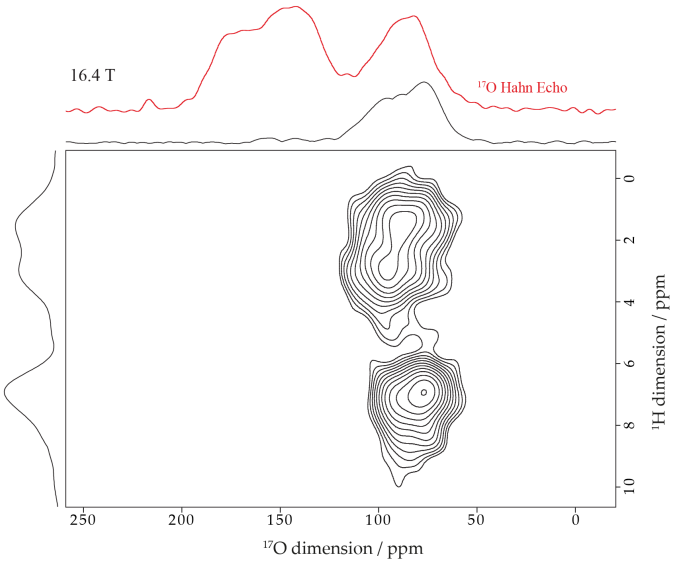

Figure 4.13: Two dimensional ^{1}H to ^{17}O hetero-nuclear correlation (2D ^{1}H-^{17}O HETCOR MAS)[21–24] with a contact time of 40 μs for the cross-polarization (CP) transfer of ^{17}O enriched $Ba_2In_2O_4(OH)_2$, obtained at 16.4T magnetic field.

for four most stable configurations discussed above (structures I, J, K and L), calculations place the O3 layer proton resonances at δ_{iso} of 7.8 - 9.3 ppm (configuration I), 8.6 - 9.1 (configuration J), 9.7 ppm (configuration K) and 9.1 - 9.9 ppm (configuration L) (Figure 4.14a). In some proportion, all ^{1}H signals are likely to be present as a single resonance in $Ba_2In_2O_4(OH)_2$ due to line widths typically in excess of 1kHz (∼2ppm on 16.4T magnet), attribute to the strong ^{1}H dipolar coupling observed under the experimental conditions used here.(Lesage [160]) A broad signal ($\Delta\nu_{1/2} = 800$ Hz) at approximately 7.3 ppm was observed for $Ba_2In_2O_4(OH)_2$ (Figure 4.10) and is therefore assigned to the protons in the O3 layer.

The two experimental resonances observed at 3.3 and 1.7 ppm are reasonably close to the δ_{iso} values calculated for the O2 layer protons at 5.2 - 5.5, 3.8 - 4.2, 5.1 and 3.7 - 3.9, ppm for configurations I, J, K and L, respectively (Figure 4.14a, Table 4.2). The ^{1}H GIPAW calculations therefore support the notion that the δ_{iso} values calculated from low energy configurations reasonably reproduce experimental results and provide a robust assignment. We note that all the ^{1}H

calculated δ_{iso} are offset by approximately 2 ppm, a value larger than the ^{1}H calculated standard deviation of 0.29 ppm (see Computational Methods above and Figure 4.4). This may be due to a ^{1}H shielding reference mismatch arising out of the use of primarily organic phases in deriving σ_{ref}, future work should be devoted to obtaining a reliable set of reference parameters for protons in inorganic materials, preferably inorganic oxides.

Calculations support the experimental assignment above. Hydrogen bonding ($-\mathrm{O}\cdots\mathrm{H}-$) has a strong effect on the chemical environment of both proton and oxygen ions due to change in electron density around them, compared to non-hydrogen bonded state. It is evident that short hydrogen-oxygen bonding (short O-H, with higher electron density on H and lower electron density on O) causes a shift to higher frequancy for the ^{1}H resonance and a shift to lower frequency of the ^{17}O resonance. The study by Yesinowski et al. [161] shows inverse correlation between donor O to acceptor O distance and ^{1}H shift with the following equation.

$$\delta_{iso}(ppm) = 79.05 - 25.5\mathrm{d}(\mathrm{O}-\mathrm{H}\cdots\mathrm{O})(\text{Å}) \tag{4.1}$$

However, this equation does not include the full geometry of the hydrogen bonding and may result in greater error for hydrogen bonds with very low strengths as noted by the authors.[161] Applying equation (4.1) onto O-O distances from I, J, K and L structures we calculate 7.4ppm and 9.7ppm ^{1}H shifts for O2 and O3 layer protons, respectively.

The ^{17}O NMR spectra in Figure 4.9a reveal that the resonance due to H-donating oxygens (O2 and O3) fall at lower shifts, while Figure 4.14a indicates that the O3 layer ^{1}H resonance fall at higher shifts than O2 layer ^{1}H due to shorter O-H bond lengths and/or more strained bond angles resulting in higher electron density around O3 layer protons (Table 4.1).

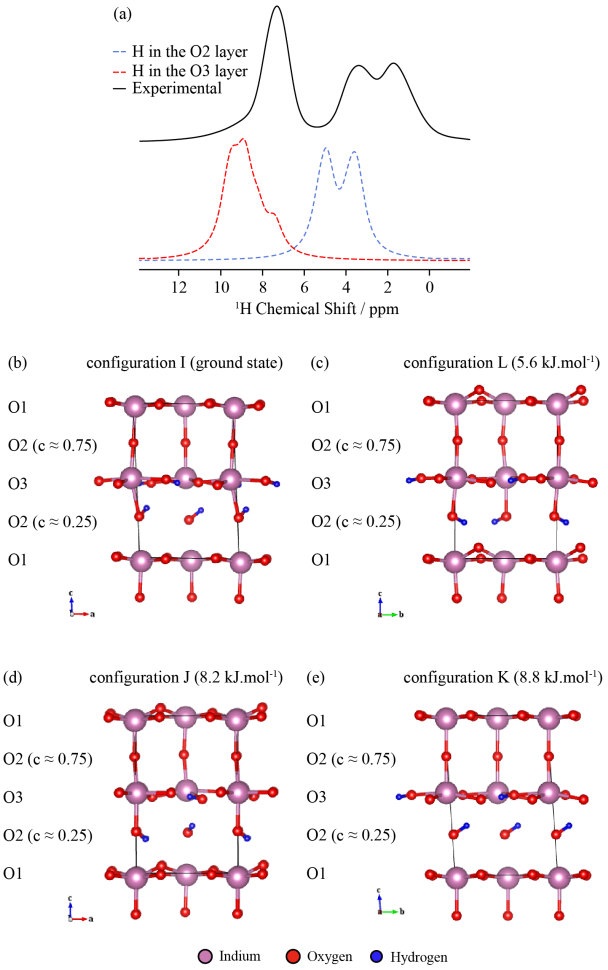

Figure 4.14: (a) Comparison of the experimental ^{1}H MAS NMR spectra of $Ba_2In_2O_4(OH)_2$ (full lines) at 22°C and the simulation of the GIPAW calculated ^{1}H NMR spectra (red dashed lines, O3 layer protons and blue dashed lines, O2 layer protons in the configuration I and K at 5.6 - 5.9 ppm and in the configuration L and J at 4.0 - 4.3 ppm). Optimized geometries of (b) configuration I (ground state), (c) configuration L, (d) configuration J and (e) configuration K showing the O3 and O2 ($c \approx 0.25$) layer protons. The interlayer Ba atoms have been omitted for clarity.

4.4 Conclusions

In summary, we have performed a comprehensive structural analysis of both the brownmillerite $Ba_2In_2O_5$ structure and its corresponding hydrated form, $Ba_2In_2O_4(OH)_2$, using multinuclear solid state NMR spectroscopy in combination with solid-state DFT calculations. Three different proton sites were observed by ^{1}H MAS NMR in $Ba_2In_2O_4(OH)_2$ as also reported by Jayaraman et al. [3] and were found to exchange at 150°C on the NMR timescale (kHz). Assignment of these resonances make use of extensive total energy DFT calculations of a wide range of proton configurations which obtained four low energy configurations, the simulated ^{1}H GIPAW NMR spectra of which are in relatively good agreement with the experimental data. Where three resonances can be assigned as high frequency shift being the O3 layer protons and the other two low frequency shifts being the two types of configurations of O2 layer protons which result in shorter and longer acceptor distances and 3°difference in $O-H\cdots O$ angles.

^{17}O NMR of $Ba_2In_2O_4(OH)_2$ yields five O sites where four of them can be very well explained by the DFT GIPAW calculations where H-donor oxygens appear at lower shift and the non-hydroxyl oxygens appear at higher shift ranges. In spite of that, the 220ppm resonance, exists due only to hydration of the system, but assignment to an environment requires further investigation.

Proton dynamics are an important topic in materials presenting proton conductivity, as in the present hydrated phase. We suggest that at least three proton sites should be considered in deriving a proton conduction mechanism in $Ba_2In_2O_4(OH)_2$ phase. High temperature ^{1}H solid state MAS NMR experiments up to 195 °C demonstrate the dynamics of all three proton sites in $Ba_2In_2O_4(OH)_2$, and show that the resonances completely coalesce at around 150°C, yielding a single site with an isotropic chemical shift of 4.4 ppm. Such coalescence process occurs at the proton jump frequency rate k of $\sim$ 2.2 kHz for the H environments of 1.7ppm and 3.3ppm, and k $\sim$ 7kHz for the H environments of 7.3ppm and 2.5ppm (second being the coalescence of 1.7ppm and 3.3ppm). As the temperature is increased further, the peak height of the new resonance increases, and its line width narrows, both due to an increase in proton motion. This clearly indicates that all protons contribute to the conductivity, as would

be anticipated for a good protonic conductor.

Chapter 5

Conclusions

In conclusion, we conducted a comprehensive structural analysis on a set of perovskite derived structures, i.e. $Ba_2In_2O_5$, $Ba_2In_2O_4(OH)_2$ and $Ba_2(In_{1-x}Ga_x)_2O_5$, using multinuclear solid state NMR spectroscopy in combination with solid-state DFT calculations.

The brownmillerite type $Ba_2In_2O_5$ with inherent oxygen lattice vacancies is a good parent material for hydration, and has structural flexibility for various types of cation doping. On the basis of the parent material study in chapter 2, we elucidated the stability of Ga doping onto the In lattice through DFT derived cluster expansion based Monte Carlo simulations, and a DFT based triple phase diagram study in chapter 3. These studies are further supported by x-ray diffraction experiments. In the last chapter (chapter 4) we studied the hydrated form of $Ba_2In_2O_5$, showing the explicit positions of H atoms in the system. We further analysed the proton dynamics with variable temperature ^{1}H NMR and oxygen atom environments with ^{17}O NMR experiments. To support our complicated solid state NMR experiments we conducted a detailed structural analysis of all possible proton sites of $Ba_2In_2O_4(OH)_2$ using DFT and GIPAW NMR calculations.

$Ba_2In_2O_5$ phase: In summary, we have performed a comprehensive structural analysis of the brownmillerite $Ba_2In_2O_5$ structure using multinuclear solid state NMR spectroscopy in combination with solid-state DFT calculations. Two distinct O environments in a 3:2 ratio were observed by ^{17}O MAS NMR in ^{17}O enriched $Ba_2In_2O_5$ and were assigned to the crystallographic O1+O3 and O2

sites. The more intense resonance seen at 179 ppm (at 21.1 T) is attributed to the combination of the O1 and O3 sublattices, while the weaker resonance at 138 ppm comprises the O2 sublattice alone. The assignment is based on GIPAW NMR calculations on both the ground state $\cdots OctTetOctTet' \cdots$ and the first high energy state $\cdots OctTetOctTet \cdots$ structures, which indicate that O1 and O3 sites have similar chemical shifts and quadrupolar couplings, preventing their separate resolution even at a very high magnetic field strength of 21.1 T. Notably the bridging O1 and O2 sites have similar calculated asymmetry parameters 0.05 and 0.15, the O1 value reflecting the more linear In-O-In bonding arrangement. In contrast, the asymmetry parameter for the bent (127.6°) In-O-In, O3 site is very different (0.9). The MQMAS data reveals a small distribution of environments consistent with some disorder in this material and making the separation of the O3 and O1 sites more difficult. An analysis of the first excited $\cdots OctTetOctTet \cdots$ structure reveals an intensity ratio for the high and low frequency shifts that is not consistent with that observed experimentally, suggesting that it is not present in significant concentrations at room temperature. However at high temperatures (∼450°C) it is highly likely that the first high energy state structure is forming and coexists with the ground state structure.

This new assignment is in contrast with the previous proposal that the two dominant but very different ^{17}O resonances arose due to the presence of InO_4 tetrahedra and InO_6 octahedra.(Adler et al. [1]) The sharp resonance at 220 ppm previously attributed to the O3 site by Adler et al. [1] is here shown to appear only upon exposure of the sample to moisture and is therefore tentatively re-assigned as originating from hydrated surface water; structural models investigated here do not reproduce the 220 ppm shift and further study is required to address this point.

$Ba_2(In_{1-x}Ga_x)_2O_5$ phase: First-principles-derived CE and MC simulations provide the local environment and long-range structures of pristine ($Ba_2In_2O_5$) and Ga-substituted $Ba_2In_2O_5$ ($Ba_2(In_{1-x}Ga_x)_2O_5$) at varying temperatures. CE and MC are shown here to work well for the comparatively simpler $Ba_2In_2O_5$ phase. For the $Ba_2In_2O_5$ phase, increasing temperature reveals a first order orthorhombic-tetragonal phase transition, and a subsequent second-order tetragonal-

cubic transformation, in accord with the experimental literature (Fischer et al. [48]). The characters of the two phase transformations are therefore well reproduced, albeit with significant errors in onset temperature, the latter likely due to the fact that the differences in vibrational enthalpy and entropy between different states of O ordering are not explicitly considered here. Separate approaches to the interpretation of the MC data are adopted, namely either averaging site occupancies over many structural snapshots at temperatures of interest or using temperature dependent site correlations obtained directly from the MC simulations. Both reveal the state of O order as a function of temperature, thereby relating directly to the experimental powder x-ray diffraction measurements.

The MC simulation of $Ba_2(In_{1-x}Ga_x)_2O_5$ yielded a brownmillerite-type structure for unsubstituted $Ba_2In_2O_5$ ($x = 0$), a similar result with higher oxygen site disorder emerging for all levels of Ga-doping under a homogeneous Ga distribution (modelled with a mean-field MC). An increase in Ga concentration, again with homogeneous Ga distribution yields a decrease in both phase transformation temperatures, and, beyond $x = 0.25$, the complete elimination of the first-order phase transformation from orthorhombic to tetragonal symmetry. This loss of the first-order transition is in agreement with experimental measurements. However, the average configurations from the model at 0K display a brownmillerite type orthorhombic or tetragonal ordering, while the experimental quenched samples (comparable with the mean field MC results) yield a cubic phase. In contrast, the triple phase diagram prepared by DFT calculations, allowing for the equilibrium distribution of Ga in $Ba_2(In_{1-x}Ga_x)_2O_5$, reveals the instability of the system at ambient temperatures with increasing Ga content. Phase transformations to cubic symmetry occur at higher temperatures in the presence of increasing amounts of mobile Ga (opposite the trend seen for a frozen in mean-field Ga distribution) and involve both cation and anion redistributions.

The theoretical results are generally supported by x-ray diffraction and pair distribution function (PDF) analyses, the former applied to both quenched and slow cooled samples, the latter only to the slow cooled samples. Samples with $0.35 \geq x \geq 0.15$ were cubic when quenched from high temperature, while slow cooling yielded orthorhombic phases at $x < 0.25$. The $x = 0.25$ phase was cubic following moderately slow cooling, but following annealing at an intermediate

temperature and quenching, phase segregation into Ga rich and Ga poor phases was observed, consistent with the theoretical results.

It is clear that an agreement between the theoretical MC simulations and the experimental thermodynamic studies using typical quenching conditions comes only by enforcing a homogeneous Ga distribution. However, both the experiments and the modelling suggest a significant tendency for Ga to form ordered phases. This structural instability of $Ba_2(In_{1-x}Ga_x)_2O_5$ and its tendency to phase separate into different ordered compounds has implications for the long-term stability of $Ba_2(In_{1-x}Ga_x)_2O_5$ as an SOFC electrolyte material. SOFCs operate in the general region (typically 973-1373 K) of the annealing temperature used in this study (1073 K). Thus the metastable cubic phase, with its desirable higher anionic conductivity [4], will likely phase segregate to form ordered phases with lower conductivities under such conditions. Furthermore, phase segregation is associated with significant changes in cell volume, which may result in the risk of mechanical breakdown of the electrolyte with thermal cycling.

The PDF analyses of $Ba_2(In_{1-x}Ga_x)_2O_5$ shown in Figure 3.17 reveal that the short-range structure of $Ba_2In_2O_5$ (1-8Å) is reasonably well preserved on increase of Ga content. Given that the majority of the doping-induced structural changes occur at longer inter-atomic distances, the use of the longer ranged CE for Ga containing phases presented in section 3.3.2 is therefore justified, despite the fact that this CE yielded a higher CV score than the shorter ranged alternative.

To conclude, we demonstrated the structural instability of $Ba_2(In_{1-x}Ga_x)_2O_5$ with high Ga content, which in turn suggests that the material with high Ga content may not be a suitable SOFC electrolyte. Beyond Ga, many other B-site substituted elements such as V, Mo and W may be doped into $Ba_2In_2O_5$ (Rolle et al. [49], Shimura and Yogo [152]) together with A-site substituents such as La and Sr (Liu et al. [153], Kakinuma et al. [154]). The long-term phase stability of these candidate SOFC electrolyte materials remain uninvestigated, suggesting an open and potentially important field for further theoretical and experimental investigations. Ab initio and MC simulations together with annealing/quenching experiments and long- and short-range structural probes such as x-ray powder diffraction, PDF analyses and solid state NMR could all play a key role in such studies.

$Ba_2In_2O_4(OH)_2$ phase: To conclude, we have performed a comprehensive structural analysis of $Ba_2In_2O_4(OH)_2$, using multinuclear solid state NMR spectroscopy in combination with solid-state DFT calculations. Three different proton sites were observed by ^{1}H MAS NMR in $Ba_2In_2O_4(OH)_2$ as also reported by Jayaraman et al. [3] and were found to exchange at 150°C on the NMR timescale (kHz). Assignment of these resonances make use of extensive total energy DFT calculations of a wide range of proton configurations which obtained four low energy configurations, the simulated ^{1}H GIPAW NMR spectra of which are in relatively good agreement with the experimental data. These three resonances can be assigned as, high frequency shift being the O3 layer protons and the other two low frequency shifts being the two types of configurations of O2 layer protons. These two types of O2 layer protons appear to have shorter and longer acceptor distances and a 3° difference in $O - H \cdots O$ angles.

^{17}O NMR of $Ba_2In_2O_4(OH)_2$ yields five O sites where four of them can be very well explained by the DFT GIPAW calculations where H-donor oxygens appear at lower shifts and the non-hydroxyl oxygens appear at higher shift ranges. In spite of that, the 220ppm resonance, which exists due only to the hydration of the system. An assignment of 220 ppm peak to an environment requires further investigation.

Proton dynamics are an important topic in materials presenting proton conductivity, as in the present hydrated phase. We suggest that at least three proton sites should be considered in deriving a proton conduction mechanism in $Ba_2In_2O_4(OH)_2$ phase. High temperature ^{1}H solid state MAS NMR experiments up to 195 °C demonstrate the dynamics of all three proton sites in $Ba_2In_2O_4(OH)_2$, and show that the resonances completely coalesce at around 150°C, yielding a single site with an isotropic chemical shift of 4.4 ppm. Such coalescence process occurs at the proton jump frequency rate k of $\sim$ 2.2 kHz for the H environments of 1.7ppm and 3.3ppm, and k $\sim$ 7kHz for the H environments of 7.3ppm and 2.5ppm (second being the coalescence of 1.7ppm and 3.3ppm). As the temperature is increased further, the peak height of the new resonance increases, and its line width narrows, both due to an increase in proton motion. This clearly indicates that all protons contribute to the conductivity, as would be anticipated for a good protonic conductor.

Appendix A

Appendix A: Computational, output data

A.1 DFT geometry optimized structures, as crystallographic information files (CIF)

In this study we used DFT calcualtions to structurally optimize 9 $Ba_2In_2O_5$ structures in the chapter 2; 81 $Ba_2In_2O_5$, 24 $Ba_2(In_{1-x}Ga_x)_2O_5$ and 9 end-member (from ICSD) structures in the chapter 3; 14 $Ba_2In_2O_4(OH)_2$ and one $Mg(OH)_2$ structures in the chapter 4. Structural information is supplied on the on-line database "DSpace@Cambridge" as crystallographic information files (CIF). (Hall et al. [162]) The exact web address is

"https://www.repository.cam.ac.uk/handle/1810/244979".

A.2 GIPAW calculated NMR parameters, as .MAGRES files

In this study we used DFT GIPAW calcualtions for NMR parameters calculatons on 9 $Ba_2In_2O_5$ structures in the chapter 2; 14 $Ba_2In_2O_4(OH)_2$ and one $Mg(OH)_2$ structures in the chapter 4. Magnetic information is supplied on the on-line database "DSpace@Cambridge" as CASTEP .MAGRES files. (Harris et al. [92], Clark et al. [130]) The exact web address is

"https://www.repository.cam.ac.uk/handle/1810/244979".

A.3 Cluster expansion (CE), ECIs and clusters

Table A.1: The effective cluster interactions (ECIs) of $Ba_2In_2O_5$. (van de Walle et al. [102])

ECI type	**ECI / eV**
Reference	-1.751446
Point O	0.000000
Pair O-O	0.262657
Pair O-O	0.031210
Pair O-O	0.326918
Pair O-O	0.023425
Pair O-O	0.041428
Pair O-O	0.005076
Pair O-O	-0.017047
Pair O-O	0.012889
Pair O-O	0.010398
Triplet O-O-O	0.057550
Triplet O-O-O	0.007995
Triplet O-O-O	0.057205

Table A.2: The $Ba_2In_2O_5$ cluster expansion (CE), clusters. (van de Walle et al. [102])

Legend	**Clusters**		
multiplicity (m) distance (r) / Å number of sites (n) coordinates of sites (x y z)	1 0.000000 0 ——— 3 0.000000 1 1.000000 0.500000 0.500000 ——— 12 3.015810 2 0.500000 1.000000 0.500000 0.500000 1.500000 0.000000 ——— 6 4.265000 2 0.500000 0.500000 1.000000 1.500000 0.500000 1.000000 ——— 3 4.265000 2 0.500000 0.500000 1.000000 0.500000 0.500000 0.000000	6 6.031621 2 0.500000 0.500000 1.000000 1.500000 1.500000 1.000000 ——— 12 6.031621 2 0.500000 0.500000 1.000000 1.500000 0.500000 0.000000 ——— 24 6.743557 2 0.500000 1.000000 0.500000 0.000000 2.500000 0.500000 ——— 12 7.387197 2 0.500000 0.500000 1.000000 1.500000 -0.500000 0.000000	48 7.979084 2 0.500000 1.000000 0.500000 1.500000 1.500000 -1.000000 ——— 8 3.015810 3 1.000000 0.500000 0.500000 1.500000 -0.000000 0.500000 1.500000 0.500000 0.000000 ——— 12 4.265000 3 0.500000 0.500000 1.000000 1.000000 0.500000 1.500000 1.500000 0.500000 1.000000 ——— 12 4.265000 3 0.500000 0.500000 1.000000 0.500000 -0.000000 0.500000 0.500000 0.500000 0.000000

Table A.3: The multi component (MC) effective cluster interactions (ECIs) and the mean field (MF) ECIs as a function of x in $Ba_2(In_{1-x}Ga_x)_2O_5$ as calculated from the MC ECIs. Where m is the multiplicity of a cluster, n is the number of In sites in a cluster and N denotes the oxygen-only clusters.(van de Walle et al. [102])

MC ECIs (type : ECI / eV)	**Excess part from In containing clusters only**	**MF ECIs**	
Ref: -8.218766 Point In: -1.275512 Point O: 0.000000 Pair In-O: 0.119839 Pair O-O: 0.380167 Pair O-O: 0.031363 Pair O-O: 0.348793 Pair In-In: 0.003420 Pair In-O: 0.021210 Pair O-O: 0.021293 Pair O-O: 0.039128 Pair O-O: 0.003948 Pair In-In: 0.005549 Pair In-O: -0.009495 Pair In-O: -0.024123 Pair O-O: -0.017358 Pair O-O: 0.012525 Pair In-In: 0.017541 Pair In-O: -0.036603 Pair O-O: 0.010197 Triplet O-In-O: 0.095607 Triplet O-O-O: 0.067861 Triplet O-O-O: 0.008593 Triplet O-In-O: 0.011304 Triplet O-O-O: 0.060790 Triplet In-O-In: 0.023497	$A_{ref} = \sum_i (\frac{m_i}{m_{ref}})(ECI)(2x-1)^n$ $A_{point} = \sum_i (\frac{m_i}{m_{point}})(ECI)(2x-1)^n$ $A_{pair} = \sum_i (\frac{m_i}{m_{pair}})(ECI)(2x-1)^n$	MF Ref: Ref + A_{ref} MF Point In: Point In MF Point O: Point O + A_{point} MF Pair N: Pair N + A_{pair} MF Triplet N: Triplet N	
		Example, x=0.125 (merged ECIs indicated by "-") -8.154800 -1.275512 -0.299534 - 0.308462 0.031363 0.340315 - - 0.021293 0.039128 0.003948 - - - -0.017358 0.012525 - - 0.010197 - 0.067861 0.008593 - 0.060790 -	**Example, x=0.25** -8.190337 -1.275512 -0.166024 0.332364 0.031363 0.343141 0.021293 0.039128 0.003948 -0.017358 0.012525 0.010197 0.067861 0.008593 0.060790

Table A.4: The $Ba_2(In_{1-x}Ga_x)_2O_5$ multi component (MC) cluster expansion (CE), clusters. (van de Walle et al. [102])

Legend	Clusters		
multiplicity (m) distance (r) / Å number of sites (n) coordinates of sites (x y z)	1 0.000000 0 — 1 0.000000 1 0.500000 0.500000 0.500000 — 3 0.000000 1 1.000000 0.500000 0.500000 — 6 2.132500 2 0.500000 0.500000 0.500000 0.500000 0.500000 0.000000 — 12 3.015810 2 1.000000 0.500000 0.500000 1.500000 0.500000 0.000000 — 6 4.265000 2 0.500000 0.500000 1.000000 1.500000 0.500000 1.000000 — 3 4.265000 2 0.500000 0.500000 1.000000 0.500000 0.500000 0.000000 — 3 4.265000 2 0.500000 0.500000 0.500000 0.500000 0.500000 -0.500000 — 24 4.768415 2 0.500000 0.500000 0.500000 0.500000 -0.500000 0.000000 — 24 5.223537 2 1.000000 0.500000 0.500000 1.500000 -0.500000 0.000000	6 6.031621 2 0.500000 0.500000 1.000000 1.500000 1.500000 1.000000 — 12 6.031621 2 0.500000 0.500000 1.000000 1.500000 0.500000 0.000000 — 6 6.031621 2 0.500000 0.500000 0.500000 0.500000 -0.500000 -0.500000 — 6 6.397500 2 1.000000 0.500000 0.500000 2.500000 0.500000 0.500000 — 24 6.397500 2 0.500000 0.500000 0.500000 -0.500000 -0.500000 0.000000 — 24 6.743557 2 0.500000 1.000000 0.500000 0.000000 2.500000 0.500000 — 12 7.387197 2 0.500000 0.500000 1.000000 1.500000 -0.500000 0.000000 — 4 7.387197 2 0.500000 0.500000 0.500000 -0.500000 -0.500000 -0.500000 — 24 7.688838 2 0.500000 1.000000 0.500000 1.500000 2.500000 0.500000	48 7.979084 2 0.500000 1.000000 0.500000 1.500000 1.500000 -1.000000 — 12 3.015810 3 1.000000 0.500000 0.500000 1.500000 0.500000 0.500000 1.500000 0.500000 0.000000 — 8 3.015810 3 1.000000 0.500000 0.500000 1.500000 -0.000000 0.500000 1.500000 0.500000 0.000000 — 12 4.265000 3 0.500000 0.500000 1.000000 1.000000 0.500000 1.500000 1.500000 0.500000 1.000000 — 3 4.265000 3 0.500000 0.500000 1.000000 0.500000 0.500000 0.500000 0.500000 0.500000 0.000000 — 12 4.265000 3 0.500000 0.500000 1.000000 0.500000 -0.000000 0.500000 0.500000 0.500000 0.000000 — 3 4.265000 3 0.500000 0.500000 0.500000 0.500000 0.500000 0.000000 0.500000 0.500000 -0.500000

References

[1] Stuart B. Adler, Jeffrey A. Reimer, Jay Baltisberger, and Ulrike Werner. Chemical structure and oxygen dynamics in $Ba_2In_2O_5$. *J. Am. Chem. Soc.*, 116:675–681, 1994. iv, 39, 41, 42, 51, 61, 122

[2] T Yao, Y Uchimoto, M Kinuhata, T Inagaki, and H Yoshida. Crystal structure of Ga-doped $Ba_2In_2O_5$ and its oxide ion conductivity. *Solid State Ionics*, 132:189–198, 2000. iv, 9, 63, 74, 78, 80, 82, 85, 91, 92

[3] V. Jayaraman, A. Magrez, M. Caldes, O. Joubert, F. Taulelle, J. Rodriguezcarvajal, Y. Piffard, and L. Brohan. Characterization of perovskite systems derived from $Ba_2In_2O_5\square$ part ii: The proton compounds $Ba_2In_{2(1-x)}Ti_{2x}O_{4+2x}(OH)_y$ $[0 \leq x \leq 1; y \leq 2(1-x)]$. *Solid State Ionics*, 170:25–32, 2004. iv, viii, ix, xiii, xiv, 7, 8, 39, 44, 50, 94, 97, 100, 102, 103, 105, 107, 108, 119, 125

[4] K.D. Kreuer. Proton-conducting oxides. *Annual Review of Materials Research*, 33:333–359, 2003. viii, 2, 4, 95

[5] John B. Goodenough. Oxide-ion electrolytes. *Annual Review of Materials Research*, 33(1):91–128, 2003. doi: 10.1146/annurev.matsci.33.022802.091651. URL http://www.annualreviews.org/doi/abs/10.1146/annurev.matsci.33.022802.091651. viii, 4

[6] Brian C. H. Steele and Angelika Heinzel. Materials for fuel-cell technologies. *Nature*, 414(6861):345–352, November 2001. ISSN 0028-0836. URL http://dx.doi.org/10.1038/35104620. viii, 4

[7] JB Goodenough, JE Ruiz-Diaz, and YS Zhen. Oxide-ion conduction in $Ba_2In_2O_5$ and $Ba_3In_2MO_8$ (M= Ce, Hf, or Zr). *Solid State Ionics*, 44: 21–31, 1990. viii, 4, 5, 7, 8, 9, 39, 41, 62, 63

[8] G. B. Zhang and D. M. Smyth. Protonic conduction in $Ba_2In_2O_5$. *Solid State Ionics*, 82(3-4):153–160, 1995. viii, 4, 8, 94

[9] Ray Dupree. *NMR of Quadrupolar Nuclei in Solid Materials (EMR Handbooks)*, chapter Double Rotation (DOR) NMR, page 134. A John Wiley and Sons Ltd., 2012. ix, 21

[10] A. A. Colville and S. Geller. The crystal structure of brownmillerite, Ca_2FeAlO_5. *Acta Crystallographica Section B Structural Crystallography and Crystal Chemistry*, 27:2311–2315, 1971. ix, 6, 7, 39, 40, 94

[11] D H Gregory and M T Weller. Phases in the system $Ba_2M_{2-x}Cu_xO_{4+\delta}$, M = In, Sc: Structure and oxygen stoichiometry. *Journal of Solid State Chemistry*, 107:134–148, 1993. ix, 6, 39, 40, 42, 47, 50

[12] S A Speakman, J W Richardson, B J Mitchell, and S T Misture. In-situ diffraction study of $Ba_2In_2O_5$. *Solid State Ionics*, 149:247–259, 2002. ix, 6, 7, 8, 9, 40, 41, 47, 48, 49, 50, 63, 70, 71, 74, 75

[13] P Berastegui, S Hull, F J Garcia-Garcia, and S G Eriksson. The crystal structures, microstructure and ionic conductivity of $Ba_2In_2O_5$ and $Ba(In_xZr_{1-x})O_{3-\frac{x}{2}}$. *Journal of Solid State Chemistry*, 164:119–130, 2002. ix, 6, 40, 41, 47, 48, 50, 75

[14] L Turner, Sonu E Chung, and Eric Oldfield. Solid-State Oxygen-17 Nuclear Magnetic Resonance Spectroscopic Study of the Group II Oxides. *Journal of Magnetic Resonance*, 64:316–324, 1985. ix, x, 52, 54, 57

[15] M. E. Smith and E.R.H. van Eck. Recent advances in experimental solid state NMR methodology for half-integer spin quadrupolar nuclei. *Progress in Nuclear Magnetic Resonance Spectroscopy*, 34(2):159–201, 1999. 184TJ Times Cited:208 Cited References Count:113. x, 51, 54, 107

[16] Jonathan R. Yates, Tran N. Pham, Chris J. Pickard, Francesco Mauri, Ana M. Amado, Ana M. Gil, and Steven P. Brown. An investigation of weak CH $\cdots$ O hydrogen bonds in maltose anomers by a combination of calculation and experimental solid-state NMR spectroscopy. *Journal of the American Chemical Society*, 127(29):10216–10220, 2005. xiv, 100, 101

[17] Amy L Webber, Bndicte Elena, John M Griffin, Jonathan R Yates, Tran N Pham, Francesco Mauri, Chris J Pickard, Ana M Gil, Robin Stein, Anne Lesage, Lyndon Emsley, and Steven P Brown. Complete ^{1}H resonance assignment of beta-maltose from ^{1}H-^{1}H DQ-SQ CRAMPS and ^{1}H (DQ-DUMBO)-^{13}C SQ refocused INEPT 2D solid-state NMR spectra and first principles GIPAW calculations. *Physical chemistry chemical physics : PCCP*, 12:6970–83, 2010. xiv, 100, 101

[18] Mariana Sardo, Rene Siegel, Srgio M Santos, Joo Rocha, Jos R B Gomes, and Luis Mafra. Combining multinuclear high-resolution solid-state mas nmr and computational methods for resonance assignment of glutathione tripeptide. *The journal of physical chemistry. A*, 116:6711–9, 2012. xiv, 100, 101

[19] R. E. J. Sears, R. Kaliaperumal, and S. Manogaran. ^{1}H shielding anisotropy in $Mg(OH)_2$: The isolated OH^- group. *The Journal of Chemical Physics*, 88(4):2284–2288, 1988. xiv, 100, 101

[20] Jean-Raphal Martinez, Chris E. Mohn, Svein Stlen, and Neil L. Allan. $Ba_2In_2O_4(OH)_2$: Proton sites, disorder and vibrational properties. *Journal of Solid State Chemistry*, 180(12):3388–3392, 2007. xiv, 42, 95, 100, 102, 103, 104, 105

[21] Hua Huo, Luming Peng, Zhehong Gan, and Clare P. Grey. Solid-state mas nmr studies of brnsted acid sites in zeolite h-mordenite. *Journal of the American Chemical Society*, 134(23):9708–9720, 2012. xvi, 98, 114, 116

[22] L. Peng, H. Huo, Y. Liu, and C. P. Grey. ^{17}O magic angle spinning NMR studies of Bronsted acid sites in zeolites HY and HZSM-5. *Journal of the American Chemical Society*, 129(2):335–46, 2007. 98, 114

[23] S. R. Hartmann and E. L. Hahn. Nuclear double resonance in the rotating frame. *Physical Review*, 128(5):2042–2053, 1962. PR. 98, 114

[24] Jacob Schaefer and E. O. Stejskal. Carbon-13 nuclear magnetic resonance of polymers spinning at the magic angle. *Journal of the American Chemical Society*, 98(4):1031–1032, 1976. xvi, 98, 114, 116

[25] 1960 Phillips, Rob. *Crystals, defects and microstructures : modeling across scales*. Cambridge University Press, Cambridge, 2001. ISBN 0521790050. 1, 24

[26] Peter G. Bruce, editor. *Solid State Electrochemistry*. Cambridge University Press, Cambridge, 1997. 1

[27] Paul Hagenmuller and W. van Gool, editors. *Solid Electrolytes: General Principles, Characterization, Materials, Applications*. Academic Press, New York, 1978. 1

[28] Tetsuichi Kudo and Kazuo Fueki. *Solid state ionics*. Kodansha ; VCH, Tokyo, 1990. ISBN 0895739852. 1

[29] Paul G Shewmon. *Diffusion in solids*. Minerals, Metals & Materials Society, Warrendale, Pa, 2nd ed edition, 1989. ISBN 9780873391054 (hbk.). 1

[30] C. Julien and G. A. Nazri. *Solid State Batteries Materials Design and Optimization*. Kluwer Academic Publishers, Boston/Dordrecht/London, 1994. 1

[31] V.V Kharton, a.a Yaremchenko, a.L Shaula, M.V Patrakeev, E.N Naumovich, D.I Logvinovich, J.R Frade, and F.M.B Marques. Transport properties and stability of ni-containing mixed conductors with perovskite- and k2nif4-type structure. *Journal of Solid State Chemistry*, 177:26–37, 2004. 1, 5

[32] Olivier Tillement. Solid state ionics electrochemical devices. *Solid State Ionics*, 68(12):9 – 33, 1994. ISSN 0167-2738. doi: 10.1016/0167-2738(94)90231-3. URL http://www.sciencedirect.com/science/article/pii/0167273894902313. 1

[33] D M Smyth. Defects and order in perovskite-related oxides. *Annual Review of Materials Science*, 15(1):329–357, 1985. doi: 10.1146/annurev.ms.15.080185.001553. URL http://www.annualreviews.org/doi/abs/10.1146/annurev.ms.15.080185.001553. 5

[34] Stuart Adler, Steven Russek, J. Reimer, Mark Fendorf, Angelica Stacy, Qingzhen Huang, Antonio Santoro, Jeffrey Lynn, Jay Baltisberger, and Ulrike Werner. Local structure and oxide-ion motion in defective perovskites. *Solid State Ionics*, 68:193–211, 1994. 5, 38

[35] P. M. Woodward. Octahedral tilting in perovskites. ii. structure stabilizing forces. *Acta Crystallographica Section B Structural Science*, 53:44–66, 1997. 5, 39

[36] P. M. Woodward. Octahedral tilting in perovskites. i. geometrical considerations. *Acta Crystallographica Section B Structural Science*, 53:32–43, 1997. 5

[37] a. M. Glazer. The classification of tilted octahedra in perovskites. *Acta Crystallographica Section B Structural Crystallography and Crystal Chemistry*, 28:3384–3392, 1972. 5

[38] Kurt R Kendall, Carlos Navas, Julie K Thomas, and Hans-Conrad zur Loye. Recent developments in perovskite-based oxide ion conductors. *Solid State Ionics*, 82:215–223, 1995. 5, 39

[39] S B Adler. Mechanism and kinetics of oxygen reduction on porous $La_{1-x}Sr_xCoO_{3-\delta}$ electrodes. *Solid State Ionics*, 111:125–134, 1998. 5

[40] M S Islam, R A Davies, C A J Fisher, and A V Chadwick. Defects and protons in the $CaZrO_3$ perovskite and $Ba_2In_2O_5$ brownmillerite: computer modelling and EXAFS studies. *Solid State Ionics*, 145:333–338, 2001. 5, 39, 42, 95

[41] A. Navrotsky Prasanna, T.R.S. Energetics of the oxygen vacancy order-disorder transition in ba2in2o5. *Journal of Materials Research*, 8(7):4, 1993. 6, 39

[42] Chris E Mohn, Neil L Allan, Colin L Freeman, P Ravindran, and Svein Stolen. Order in the disordered state: local structural entities in the fast ion conductor $Ba_2In_2O_5$. *Journal of Solid State Chemistry*, 178(1):346–355, 2005. 6, 39, 40, 42, 47, 48, 49, 63

[43] M. Yoshinaga, T. Fumoto, and T. Hashimoto. Electrical conductivity and crystal structure of $Ba_2In_2O_5$ at high temperatures under various oxygen partial pressures. *Journal of The Electrochemical Society*, 152:A1221, 2005. 6, 39

[44] Takuya Hashimoto. Observation of two kinds of structural phase transitions in the $Ba_2In_2O_5$ system. *Journal of The Electrochemical Society*, 149: A1381–A1384, 2002. 6, 39

[45] A Rolle, R N Vannier, N V Giridharan, and F Abraham. Structural and electrochemical characterisation of new oxide ion conductors for oxygen generating systems and fuel cells. *Solid State Ionics*, 176:2095–2103, 2005. 6, 39

[46] B. C. H. Steele. *Oxygen Ion Conductors*, page 690. World Scientific Publishing Co. Inc., Teaneck, NJ, 1989. 7, 8, 39, 41

[47] C A J Fisher, M S Islam, and R J Brook. A computer simulation investigation of brownmillerite-structured $Ba_2In_2O_5$. *Journal of Solid State Chemistry*, 128:137–141, 1997. 8, 42

[48] W Fischer, G Reck, and T Schober. Structural transformation of the oxygen and proton conductor $Ba_2In_2O_5$ in humid air: an in-situ X-ray powder diffraction study. *Solid State Ionics*, 116:211–215, 1999. 9, 39, 47, 49, 63, 67, 90, 102, 123

[49] A Rolle, G Fafilek, and R N Vannier. Redox stability of $Ba_2In_2O_5$-doped compounds. *Solid State Ionics*, 179:113–119, 2008. 9, 63, 92, 124

[50] E. M. Purcell, H. C. Torrey, and R. V. Pound. Resonance absorption by nuclear magnetic moments in a solid. *Phys. Rev.*, 69:37–38, Jan 1946.

doi: 10.1103/PhysRev.69.37. URL http://link.aps.org/doi/10.1103/PhysRev.69.37. 10

[51] F. Bloch, W. W. Hansen, and Martin Packard. Nuclear induction. *Physical Review*, 69:127–127, Feb 1946. doi: 10.1103/PhysRev.69.127. URL http://link.aps.org/doi/10.1103/PhysRev.69.127. 10

[52] Jean-Paul Amoureux, Christian Fernandez, and Stefan Steuernagel. Z filtering in MQMAS NMR. *Journal of Magnetic Resonance, Series A*, Series A 1:116–118, 1996. 10, 43, 51

[53] Kazuyuki Takeda. Microcoils and microsamples in solid-state nmr. *Solid State Nuclear Magnetic Resonance*, 47-48(0):1–9, 2012. 10

[54] Jonathan F. Stebbins. Nuclear magnetic resonance at high temperature. *Chemical Reviews*, 91(7):1353–1373, 1991. doi: 10.1021/cr00007a004. URL http://pubs.acs.org/doi/abs/10.1021/cr00007a004. 10

[55] F. Taulelle, J. P. Coutures, D. Massiot, and J. P. Rifflet. High and very high temperature NMR. *Buletin of Magnetic Resonance*, 11(3/4):318–320, 1989. 10

[56] Michel Letellier, Frederic Chevallier, Christian Clinard, Elzbieta Frackowiak, Jean-Noel Rouzaud, Francois Beguin, Mathieu Morcrette, and Jean-Marie Tarascon. The first in situ ^{7}Li nuclear magnetic resonance study of lithium insertion in hard-carbon anode materials for li-ion batteries. *The Journal of Chemical Physics*, 118(13):6038–6045, 2003. doi: 10.1063/1.1556092. URL http://link.aip.org/link/?JCP/118/6038/1. 10

[57] F. Chevallier, M. Letellier, M. Morcrette, J.-M. Tarascon, E. Frackowiak, J.-N. Rouzaud, and F. Bguin. In situ ^{7}Li-nuclear magnetic resonance observation of reversible lithium insertion into disordered carbons. *Electrochemical and Solid-State Letters*, 6(11):A225–A228, 2003. doi: 10.1149/1.1612011. URL http://esl.ecsdl.org/content/6/11/A225.abstract. 10

[58] Michel Letellier, Frdric Chevallier, Franois Bguin, Elzbieta Frackowiak, and Jean-Nol Rouzaud. The first in situ ^{7}Li NMR study of the reversible lithium insertion mechanism in disorganised carbons. *Journal of Physics and Chemistry of Solids*, 65(23):245 – 251, 2004. ISSN 0022-3697. doi: 10.1016/j.jpcs.2003.10.022. URL http://www.sciencedirect.com/science/article/pii/S0022369703003834. 10

[59] Baris Key, Rangeet Bhattacharyya, Mathieu Morcrette, Vincent Seznec, Jean-Marie Tarascon, and Clare P. Grey. Real-time nmr investigations of structural changes in silicon electrodes for lithium-ion batteries. *Journal of the American Chemical Society*, 131(26):9239–9249, 2009. doi: 10.1021/ja8086278. URL http://pubs.acs.org/doi/abs/10.1021/ja8086278. PMID: 19298062. 10

[60] Thibault Charpentier. The PAW/GIPAW approach for computing NMR parameters: a new dimension added to NMR study of solids. *Solid state nuclear magnetic resonance*, 40:1–20, 2011. 10, 32, 42

[61] Christian Bonhomme, Christel Gervais, Florence Babonneau, Cristina Coelho, Frédérique Pourpoint, Thierry Azaïs, Sharon E. Ashbrook, John M. Griffin, Jonathan R. Yates, Francesco Mauri, and Chris J. Pickard. First-principles calculation of NMR parameters using the gauge including projector augmented wave method: A chemist's point of view. *Chemical Reviews*, 112(11):5733–5779, 2012. 10, 24

[62] Chris Pickard and Francesco Mauri. All-electron magnetic response with pseudopotentials: Nmr chemical shifts. *Physical Review B*, 63:1–13, 2001. 10, 32, 42, 46, 95, 99

[63] A. van de Walle and G. Ceder. Automating first-principles phase diagram calculations. *Journal of Phase Equilibria and Diffusion*, 23(4):348–359, 2002. 10.1361/105497102770331596. 10, 37, 65, 67

[64] Artem R. Oganov and Colin W. Glass. Crystal structure prediction using ab initio evolutionary techniques: Principles and applications. *The Journal*

of Chemical Physics, 124(24):244704, 2006. doi: 10.1063/1.2210932. URL http://link.aip.org/link/?JCP/124/244704/1. 11

[65] Chris J Pickard and R J Needs. Ab initio random structure searching. *Journal of Physics: Condensed Matter*, 23(5):053201, 2011. URL http://stacks.iop.org/0953-8984/23/i=5/a=053201. 11

[66] James Keeler. *Understanding NMR spectroscopy*. John Wiley & Sons, Chichester, 2007. ISBN 9780470017869 (hardback). 11

[67] Malcolm H Levitt. *Spin dynamics : basics of nuclear magnetic resonance*. Wiley, Chichester, 2nd ed edition, 2008. ISBN 9780470511176 (pbk.). 11

[68] P. J Hore. *Nuclear magnetic resonance*. Oxford University Press, Oxford, 1995. ISBN 0198556829. 11

[69] Melinda J Duer. *Introduction to solid-state NMR spectroscopy*. Blackwell Science, Malden, MA, 2004. ISBN 1405109149. 11

[70] K. J. D. MacKenzie and M. E. Smith. *Multinuclear Solid State NMR of Inorganic Materials*. 2002. 11

[71] David C. Apperley, Robin Kingsley Harris, and Paul Hodgkinson. *Solid-state NMR : basic principles & practice*. Momentum,, New York, 2012. URL http://search.lib.cam.ac.uk/?itemid=|cambrdgedb|5485881. 11

[72] Emine Kucukbenli. *Nuclear Magnetic Resonance Study of Complex Molecular Crystals From First Principles: Case of Cholesterol*. Ph.d., International School for Advanced Studies - Condensed Matter Theory Sector, SISSA - Via Bonomea 265, 34136 Trieste - ITALY, 2011. URL http://hdl.handle.net/1963/5356. 11

[73] A. Llor and J. Virlet. Towards high-resolution {NMR} of more nuclei in solids: Sample spinning with time-dependent spinner axis angle. *Chemical Physics Letters*, 152(23):248 – 253, 1988. ISSN 0009-2614. doi: http://dx.doi.org/10.1016/0009-2614(88)87362-7. URL http://www.sciencedirect.com/science/article/pii/0009261488873627. 22, 24

[74] A. Samoson, E. Lippmaa, and A. Pines. High resolution solid-state n.m.r. *Molecular Physics*, 65(4):1013–1018, 1988. doi: 10.1080/00268978800101571. URL http://www.tandfonline.com/doi/abs/10.1080/00268978800101571. 22, 24

[75] Lucio Frydman and John S Harwood. Isotropic spectra of half-integer quadrupolar spins from bidimensional magic-angle spinning nmr. *Journal of the American Chemical* , 117:5367–5368, 1995. 22, 23, 42, 43, 51

[76] Ales Medek, John S. Harwood, and Lucio Frydman. Multiple-quantum magic-angle spinning nmr: A new method for the study of quadrupolar nuclei in solids. *Journal of the American Chemical Society*, 117:12779–12787, 1995. 22, 23, 42, 43, 51

[77] S. E. Ashbrook and S. Wimperis. Multiple-quantum cross-polarization and two-dimensional MQMAS NMR of quadrupolar nuclei. *J Magn Reson*, 147 (2):238–49, 2000. 22

[78] David S. Sholl and Janice A. Steckel. *Density Functional Theory, A Practical Introduction*. John Wiley & Sons, 2009. ISBN ISBN 978-0-470-37317-0. 24

[79] P. Hohenberg and W. Kohn. Inhomogeneous electron gas. *Phys. Rev.*, 136:B864–B871, Nov 1964. doi: 10.1103/PhysRev.136.B864. URL http://link.aps.org/doi/10.1103/PhysRev.136.B864. 25

[80] W. Kohn and L. J. Sham. Self-consistent equations including exchange and correlation effects. *Phys. Rev.*, 140:A1133–A1138, Nov 1965. doi: 10.1103/PhysRev.140.A1133. URL http://link.aps.org/doi/10.1103/PhysRev.140.A1133. 26

[81] I. Stich, R. Car, M. Parrinello, and S. Baroni. Conjugate gradient minimization of the energy functional: A new method for electronic structure calculation. *Phys. Rev. B*, 39:4997–5004, Mar 1989. doi: 10.1103/PhysRevB.39.4997. URL http://link.aps.org/doi/10.1103/PhysRevB.39.4997. 28

[82] D. M. Ceperley and B. J. Alder. Ground state of the electron gas by a stochastic method. *Physical Review Letters*, 45:566–569, Aug 1980. doi: 10.1103/PhysRevLett.45.566. URL http://link.aps.org/doi/10.1103/PhysRevLett.45.566. 29

[83] J. P. Perdew and Alex Zunger. Self-interaction correction to density-functional approximations for many-electron systems. *Phys. Rev. B*, 23: 5048–5079, May 1981. doi: 10.1103/PhysRevB.23.5048. URL http://link.aps.org/doi/10.1103/PhysRevB.23.5048. 29

[84] John P. Perdew and Yue Wang. Accurate and simple analytic representation of the electron-gas correlation energy. *Phys. Rev. B*, 45:13244–13249, Jun 1992. doi: 10.1103/PhysRevB.45.13244. URL http://link.aps.org/doi/10.1103/PhysRevB.45.13244. 29

[85] John P. Perdew, Kieron Burke, and Matthias Ernzerhof. Generalized gradient approximation made simple. *Physical Review Letters*, 77(18):3865–3868, 1996. PRL. 29, 45, 65

[86] Yingkai Zhang and Weitao Yang. Comment on "generalized gradient approximation made simple". *Phys. Rev. Lett.*, 80:890–890, Jan 1998. doi: 10.1103/PhysRevLett.80.890. URL http://link.aps.org/doi/10.1103/PhysRevLett.80.890. 29

[87] Felix Bloch. Über die quantenmechanik der elektronen in kristallgittern. *Zeitschrift für Physik*, 52:555–600, 1929. ISSN 0044-3328. doi: 10.1007/BF01339455. URL http://dx.doi.org/10.1007/BF01339455. 29

[88] Hendrik J. Monkhorst and James D. Pack. Special points for brillouin-zone integrations. *Phys. Rev. B*, 13:5188–5192, Jun 1976. doi: 10.1103/PhysRevB.13.5188. URL http://link.aps.org/doi/10.1103/PhysRevB.13.5188. 30, 65

[89] N. Troullier and José Luriaas Martins. Efficient pseudopotentials for plane-wave calculations. *Phys. Rev. B*, 43:1993–2006, Jan 1991. doi: 10.1103/PhysRevB.43.1993. URL http://link.aps.org/doi/10.1103/PhysRevB.43.1993. 31

[90] David Vanderbilt. Soft self-consistent pseudopotentials in a generalized eigenvalue formalism. *Phys. Rev. B*, 41:7892–7895, Apr 1990. doi: 10.1103/PhysRevB.41.7892. URL http://link.aps.org/doi/10.1103/PhysRevB.41.7892. 31

[91] Jonathan R. Yates, Chris J. Pickard, and Francesco Mauri. Calculation of nmr chemical shifts for extended systems using ultrasoft pseudopotentials. *Phys. Rev. B*, 76:024401, Jul 2007. doi: 10.1103/PhysRevB.76.024401. URL http://link.aps.org/doi/10.1103/PhysRevB.76.024401. 32, 34, 35, 46, 99

[92] Robin K. Harris, Paul Hodgkinson, Chris J. Pickard, Jonathan R. Yates, and Vadim Zorin. Chemical shift computations on a crystallographic basis: some reflections and comments. *Magnetic Resonance in Chemistry*, 45(S1): S174–S186, 2007. ISSN 1097-458X. doi: 10.1002/mrc.2132. URL http://dx.doi.org/10.1002/mrc.2132. 32, 127

[93] Thomas Gregor, Francesco Mauri, and Roberto Car. A comparison of methods for the calculation of nmr chemical shifts. *The Journal of Chemical Physics*, 111(5):1815–1822, 1999. doi: 10.1063/1.479451. URL http://link.aip.org/link/?JCP/111/1815/1. 34

[94] M Profeta, F. Mauri, and C.J. Pickard. Accurate first principles prediction of ^{17}O NMR parameters in SiO_2: Assignment of the zeolite ferrierite spectrum. *J. Am. Chem. Soc.*, 125:2541–548, 2003. 35, 46, 99

[95] Pekka Pyykkö. Year-2008 nuclear quadrupole moments. *Molecular Physics*, 106(16-18):1965–1974, 2008. doi: 10.1080/00268970802018367. URL http://www.tandfonline.com/doi/abs/10.1080/00268970802018367. 35, 46, 100

[96] Nicholas Metropolis, Arianna W. Rosenbluth, Marshall N. Rosenbluth, Augusta H. Teller, and Edward Teller. Equation of state calculations by fast computing machines. *The Journal of Chemical Physics*, 21(6):1087–1092, 1953. doi: 10.1063/1.1699114. URL http://link.aip.org/link/?JCP/21/1087/1. 35

[97] R. A. Farrell, T. Morita, and P. H. E. Meijer. Cluster expansion for the ising model. *The Journal of Chemical Physics*, 45:349, 1966. 36

[98] J. M. Sanchez, F. Ducastelle, and D. Gratias. Generalized cluster description of multicomponent systems. *Physica A: Statistical and Theoretical Physics*, 128(1-2):334–350, 1984. 36, 64, 67

[99] D. de Fontaine. Cluster approach to order-disorder transformation in alloys. *Solid State Physics*, 47:33–176, 1994. 36, 64

[100] A. Zunger. *Nato Advanced Study Institute on Statics Dynamics of Alloy Phase, Transformations*, volume v. 319 of *NATO ASI series Series B, Physics ;*, pages 361–419. Plenum, New York, London, 1994. (1992 : Rhodes, Greece) "Published in cooperation with NATO Scientific Affairs Division.". "Proceedings of a NATO Advanced Study Institute on Statics and Dynamics of Alloy Phase Transformations, held June 21-July 3, 1992, in Rhodes, Greece"–T.p. verso. 36, 64

[101] M H Kutner, C J Nachtschiem, W Wasserman, and J Neter. Applied linear statistical models. 1996. 37, 64

[102] A van de Walle, M Asta, and G Ceder. The alloy theoretic automated toolkit: A user guide. *Calphad*, 26:539–553, 2002. doi: DOI: 10.1016/S0364-5916(02)80006-2. 37, 68, 128, 129, 130, 131

[103] A van de Walle and M Asta. Self-driven lattice-model monte carlo simulations of alloy thermodynamic properties and phase diagrams. *Modelling and Simulation in Materials Science and Engineering*, (5):521, 2002. 37, 64, 65, 67

[104] A. van de Walle and G. Ceder. The effect of lattice vibrations on substitutional alloy thermodynamics. *Reviews of Modern Physics*, 74(1):11, 2002. Copyright (C) 2008 The American Physical Society Please report any problems to prola@aps.org RMP. 37

[105] Andrew R Leach. *Molecular modelling : principles and applications*. Longman, Harlow, 1996. ISBN 0582239338. 37

[106] Lorenzo Malavasi, Craig A. J. Fisher, and M. Saiful Islam. Oxide-ion and proton conducting electrolyte materials for clean energy applications: structural and mechanistic features. *Chemical Society Reviews*, 39(11):4370–4387, 2010. 38, 93

[107] V V Kharton, F M B Marques, and A Atkinson. Transport properties of solid oxide electrolyte ceramics: a brief review. *Solid State Ionics*, 174: 135–149, 2004. 39

[108] E. F. Bertaut, P. Blum, and a. Sagnires. Structure du ferrite bicalcique et de la brownmillerite. *Acta Crystallographica*, 12:149–159, 1959. 41

[109] C A J Fisher and M S Islam. Defect, protons and conductivity in brownmillerite-structured $Ba_2In_2O_5$. *Solid State Ionics*, 118:355–363, 1999. 42

[110] Masami Kanzaki and Akihiko Yamaji. Molecular dynamics simulation of oxygen ion diffusion in $Ba_2In_2O_5$. *Materials Science and Engineering B*, 41: 46–49, 1996. 42

[111] Chris E. Mohn, Neil L. Allan, Colin L. Freeman, Ponniah Ravindran, and Svein Stolen. Collective ionic motion in oxide fast-ion-conductors. *Physical Chemistry Chemical Physics*, 6(12):3052, 2004. 42

[112] Christel Gervais, Mickael Profeta, Florence Babonneau, Chris J Pickard, and Francesco Mauri. Ab initio calculations of nmr parameters of highly coordinated oxygen sites in aluminosilicates. *J. Phys. Chem. B*, 108:13249–13253, 2004. 42

[113] Alan Wong, Gary Thurgood, Ray Dupree, and Mark E Smith. A first-principles computational ^{17}O NMR investigation of metal ion oxygen interactions in carboxylate oxygens of alkali oxalates. *Chemical Physics*, 337: 144–150, 2007. 42

[114] Elodie Salager, Graeme M Day, Robin S Stein, Chris J Pickard, Bénédicte Elena, and Lyndon Emsley. Powder crystallography by combined crystal

structure prediction and high-resolution ^{1}H solid-state NMR spectroscopy. *Journal of the American Chemical Society*, 132:2564–6, 2010. 42

[115] Sharon E Ashbrook, Andrew J Berry, Daniel J Frost, Alan Gregorovic, Chris J Pickard, Jennifer E Readman, and Stephen Wimperis. ^{17}O and ^{29}Si NMR parameters of $MgSiO_3$ phases from high-resolution solid-state NMR spectroscopy and first-principles calculations. *J. Am. Chem. Soc.*, 129:13213–13224, 2007. 42

[116] Sharon E Ashbrook, Laurent Le Polles, Gautier Regis, Chris J. Pickard, and Richard I. Walton. ^{23}Na multiple-quantum MAS NMR of the perovskites $NaNbO_3$ and $NaTaO_3$. *Phys. Chem. Chem. Phys.*, 8:3423–3431, 2006. 42

[117] Karen E Johnston, John M Griffin, Richard I Walton, Daniel M Dawson, Philip Lightfoot, and Sharon E Ashbrook. ^{93}Nb NMR and DFT investigation of the polymorphs of NaNbO3. *Physical chemistry chemical physics : PCCP*, 13:7565–7576, 2011. 42

[118] Karen E Johnston, Chiu C Tang, Julia E Parker, Kevin S Knight, Philip Lightfoot, and Sharon E Ashbrook. The polar phase of $NaNbO_3$: a combined study by powder diffraction, solid-state NMR, and first-principles calculations. *Journal of the American Chemical Society*, 132:8732–46, 2010. 42, 45, 99

[119] Frédéric Blanc, Derek S Middlemiss, Zhehong Gan, and Clare P Grey. Defects in doped $LaGaO_3$ anionic conductors: linking NMR spectral features, local environments, and defect thermodynamics. *Journal of the American Chemical Society*, 133:17662–72, 2011. 42, 45, 54, 99

[120] Frédéric Blanc, Derek S Middlemiss, Lucienne Buannic, John L Palumbo, Ian Farnan, and Clare P Grey. Thermal phase transformations in $LaGaO_3$ and $LaAlO_3$ perovskites: an experimental and computational solid-state NMR study. *Solid state nuclear magnetic resonance*, 42:87–97, 2012. 42

[121] Lucienne Buannic, Frédéric Blanc, Derek S. Middlemiss, and Clare P. Grey. Probing cation and vacancy ordering in the dry and hydrated yttrium-substituted $BaSnO_3$ perovskite by NMR spectroscopy and first principles

calculations: Implications for proton mobility. *Journal of the American Chemical Society*, 134(35):14483–14498, 2012. 42, 45, 99

[122] Anthony R. West. *Solid state chemistry and its applications*. Wiley, 1984. ISBN 0471908746. 43, 96

[123] Sharon E Ashbrook and Mark E Smith. Solid state ^{17}O NMR-an introduction to the background principles and applications to inorganic materials. *Chemical Society reviews*, 35:718–735, 2006. 43, 54, 96

[124] BRUKER. *Topspin 3.1, software for NMR spectral analysis*. Bruker Biospin, Rheinstetten , Germany. Bruker Biospin, Rheinstetten , Germany, 2011. 45, 98

[125] Jacco D van Beek. matNMR: a flexible toolbox for processing, analyzing and visualizing magnetic resonance data in Matlab. *Journal of Magnetic Resonance*, 187:19–26, 2007. 45, 98

[126] D. S. Middlemiss, F. Blanc, C. J. Pickard, and C. P. Grey. Solid-state nmr calculations for metal oxides and gallates: shielding and quadrupolar parameters for perovskites and related phases. *J Magn Reson*, 204(1):1–10, 2010. 45, 46, 54, 56, 99, 100

[127] N. S. Barrow, J. R. Yates, S. A. Feller, D. Holland, S. E. Ashbrook, P. Hodgkinson, and S. P. Brown. Towards homonuclear J solid-state NMR correlation experiments for half-integer quadrupolar nuclei: Experimental and simulated ^{11}B MAS spin-echo dephasing and calculated 2J BB coupling constants for lithium diborate. *Physical Chemistry Chemical Physics*, 13(13):5778–5789, 2011. URL http://www.scopus.com/inward/record.url?eid=2-s2.0-79952730412&partnerID=40&md5=2bdd4b94da8159694fc0501ca09a5873. cited By (since 1996)8. 45, 99

[128] Simon W. Reader, Martin R. Mitchell, Karen E. Johnston, Chris J. Pickard, Karl R. Whittle, and Sharon E. Ashbrook. Cation disorder in pyrochlore ceramics: ^{89}Y MAS NMR and first-principles calculations. *The Journal of Physical Chemistry C*, 113(43):18874–18883, 2009. 45, 54, 99

[129] Martin R. Mitchell, Simon W. Reader, Karen E. Johnston, Chris J. Pickard, Karl R. Whittle, and Sharon E. Ashbrook. ^{119}Sn MAS NMR and first-principles calculations for the investigation of disorder in stannate pyrochlores. *Physical Chemistry Chemical Physics*, 13(2):488–497, 2011. 45, 99

[130] S. J. Clark, M. D. Segall, C. J. Pickard, P. J. Hasnip, M. J. Probert, K. Refson, and M.C. Payne. First principles methods using CASTEP. *Z. Kristall.*, 220:567–570, 2005. 45, 99, 127

[131] M. Bak, J. T. Rasmussen, and N. Chr Nielsen. Simpson: A general simulation program for solid-state nmr spectroscopy. *Journal of Magnetic Resonance*, 147(2):296–330, 2000. Cited By (since 1996): 783 Export Date: 16 October 2012 Source: Scopus. 46, 100

[132] Timothy J. Bastow, Peter J. Dirken, Mark E. Smith, and Harold J. Whitfield. Factors controlling the ^{17}O NMR chemical shift in ionic mixed metal oxides. *The Journal of Physical Chemistry*, 100:18539–18545, 1996. 51, 54, 56

[133] John L. Palumbo, Tobias a. Schaedler, Luming Peng, Carlos G. Levi, and Clare P. Grey. ^{17}O NMR studies of local structure and phase evolution for materials in the $Y_2Ti_2O_7$ - $ZrTiO_4$ binary system. *Journal of Solid State Chemistry*, 180:2175–2185, 2007. 54

[134] Svein Stølen, Egil Bakken, and Chris E Mohn. Oxygen-deficient perovskites: linking structure, energetics and ion transport. *Physical chemistry chemical physics : PCCP*, 8:429–447, 2006. 63

[135] Chris E Mohn, Neil L Allan, and Svein Stølen. Sr and Ga substituted $Ba_2In_2O_5$: Linking ionic conductivity and the potential energy surface. *Solid State Ionics*, 177:223–228, 2006. 63

[136] Yueh-Lin Lee and Dane Morgan. Ab initio study of oxygen-vacancy ordering in oxygen conducting $Ba_2In_2O_5$. *MRS Proceedings*, 972, 2006. doi: 10.1557/PROC-0972-AA04-06. URL http://journals.cambridge.org/article_S1946427400056542. 63, 78

[137] P E Blöchl. Projector augmented-wave method. *Phys. Rev. B*, 50:17953–17979, 1994. 65

[138] G Kresse and D Joubert. From ultrasoft pseudopotentials to the projector augmented-wave method. *Phys. Rev. B*, 59:1758–1775, 1999. 65

[139] G Kresse and J Furthmüller. Efficiency of ab-initio total energy calculations for metals and semiconductors using a plane-wave basis set. *Computational Materials Science*, 6:15–50, 1996. 65

[140] G. Bergerhoff and I.D. Brown. *Crystallographic Databases*, page 221. Chester, International Union of Crystallography, 1987. ICSD ref. 65

[141] M E J Newman and G T Barkema. Monte Carlo methods in statistical physics. 1999. 65, 67

[142] Koichi Momma and Fujio Izumi. Vesta: a three-dimensional visualization system for electronic and structural analysis. *Journal of Applied Crystallography*, 41:653–658, 2008. 67

[143] Harold T. Stokes and Dorian M. Hatch. *FINDSYM*: program for identifying the space-group symmetry of a crystal. *Journal of Applied Crystallography*, 38(1):237–238, Feb 2005. doi: 10.1107/S0021889804031528. URL http://dx.doi.org/10.1107/S0021889804031528. 67, 80

[144] A.C. Larson and RB Von Dreele. General structure analysis system (GSAS). In *Structure*, volume 748, 2000. 68

[145] AP Hammersley. FIT2D: an introduction and overview. In *European Synchrotron Radiation Facility Internal Report ESRF97HA02T*, 1997. 68

[146] Xiangyun Qiu, Jeroen W Thompson, and Simon J L Billinge. PDFgetX2: a GUI-driven program to obtain the pair distribution function from X-ray powder diffraction data. *Journal of Applied Crystallography*, 37:678, 2004. 68

[147] C. L. Farrow, P. Juhas, J. W. Liu, D. Bryndin, E. S. Bozin, J. Bloch, Proffen Th, and S. J. L. Billinge. PDFfit2 and PDFgui: computer programs for

studying nanostructure in crystals. *Journal of Physics: Condensed Matter*, (33):335219, 2007. 68

[148] L. Bellaiche and David Vanderbilt. Virtual crystal approximation revisited: Application to dielectric and piezoelectric properties of perovskites. *Physical Review B*, 61:7877–7882, 2000. 80

[149] John P. Perdew. Density functional theory and the band gap problem. *International Journal of Quantum Chemistry*, 28(S19):497–523, 1985. ISSN 1097-461X. doi: 10.1002/qua.560280846. URL http://dx.doi.org/10.1002/qua.560280846. 82

[150] John P. Perdew, Adrienn Ruzsinszky, Lucian A. Constantin, Jianwei Sun, and Gabor I. Csonka. Some fundamental issues in ground-state density functional theory: A guide for the perplexed. *Journal of Chemical Theory and Computation*, 5(4):902–908, 2009. doi: 10.1021/ct800531s. URL http://pubs.acs.org/doi/abs/10.1021/ct800531s. 82

[151] Defa Wang, Zhigang Zou, and Jinhua Ye. Photocatalytic water splitting with the Cr-doped $Ba_2In_2O_5/In_2O_3$ composite oxide semiconductors. *Chem. Mater.*, 17(12):3255–3261, May 2005. ISSN 0897-4756. doi: 10.1021/cm0477117. URL http://dx.doi.org/10.1021/cm0477117. 82

[152] Tetsuo Shimura and Toshinobu Yogo. Electrical properties of the tungsten-doped $Ba_2In_2O_5$. *Solid State Ionics*, 175:345–348, 2004. 92, 124

[153] Yun Liu, Ray L Withers, and John Fitz Gerald. A TEM, XRD, and crystal chemical investigation of oxygenvacancy ordering in $(Ba_{1-x}La_x)_2In_2O_{5+x}$, $0 \leq x \leq 0.6$. *Journal of Solid State Chemistry*, 170:247–254, 2003. 92, 124

[154] Katsuyoshi Kakinuma, Hiroshi Yamamura, Hajime Haneda, and Tooru Atake. Oxide-ion conductivity of the perovskite-type solid-solution system, $(Ba_{1-x-y}Sr_xLa_y)_2In_2O_{5+y}$. *Solid State Ionics*, 154-155:571–576, 2002. 92, 124

[155] T. Schober, J. Friedrich, and F. Krug. Phase transition in the oxygen and proton conductor $Ba_2In_2O_5$ in humid atmospheres below 300°C. *Solid State Ionics*, 99:9–13, 1997. 96

[156] Anthony Bielecki and Douglas P. Burum. Temperature dependence of ^{207}Pb MAS spectra of solid lead nitrate. an accurate, sensitive thermometer for variable-temperature MAS. *Journal of Magnetic Resonance, Series A*, 116: 215–220, 1995. 98

[157] P. A. Beckmann and C Dybowski. A thermometer for nonspinning solid-state NMR spectroscopy. *Journal of magnetic resonance (San Diego, Calif. : 1997)*, 146:379–80, 2000. 98

[158] John P. Perdew, Kieron Burke, and Matthias Ernzerhof. *Local and Gradient-Corrected Density Functionals*, chapter 31, pages 453–462. American Chemical Society, 1996. doi: 10.1021/bk-1996-0629.ch030. URL http://pubs.acs.org/doi/abs/10.1021/bk-1996-0629.ch030. 99

[159] V. Jayaraman, A. Magrez, M. Caldes, O. Joubert, M. Ganne, Y. Piffard, and L. Brohan. Characterization of perovskite systems derived from $Ba_2In_2O_5\square$ part i: the oxygen-deficient $Ba_2In_{2(1-x)}Ti_{2x}O_{5+x}\square_{1-x}$ ($0 \leq x \leq 1$) compounds. *Solid State Ionics*, 170:17–24, 2004. 102

[160] Anne Lesage. Recent advances in solid-state NMR spectroscopy of spin I = 1/2 nuclei. *Physical Chemistry Chemical Physics*, 11(32):6876–6891, 2009. 108, 116

[161] James P. Yesinowski, Hellmut. Eckert, and George R. Rossman. Characterization of hydrous species in minerals by high-speed proton MAS-NMR. *Journal of the American Chemical Society*, 110(5):1367–1375, 1988. doi: 10.1021/ja00213a007. URL http://pubs.acs.org/doi/abs/10.1021/ja00213a007. 117

[162] S. R. Hall, F. H. Allen, and I. D. Brown. The crystallographic information file (CIF): a new standard archive file for crystallography. *Acta Crystallographica Section A*, 47(6):655–685, Nov 1991.

doi: 10.1107/S010876739101067X. URL http://dx.doi.org/10.1107/S010876739101067X. 126